CRUSTAL STRESS DISTRIBUTION:
A STUDY OF ITS CHARACTERISTICS AND MECHANISM
BASED ON HYDRAULIC FRACTURING STRESS MEASUREMENTS

A DISSERTATION

SUBMITTED TO THE DEPARTMENT OF GEOPHYSICS,

FACULTY OF SCIENCE, HOKKAIDO UNIVERSITY

FOR THE DEGREE OF

DOCTOR OF SCIENCE

By

Ryuji Ikeda

December, 1991

ABSTRACT

Stress measurements by the hydraulic fracturing method have been conducted at 20 sites in the Kanto-Tokai area in the central part of Japan. Hydraulic fracturing, which is the best method to obtain in situ stress data in deep boreholes at present, was adopted for the first time in 1978 in Japan. Stress data, stress orientations and magnitudes, have been obtained successfully from boreholes drilled to depths from 100 m to 900 m. To conduct more sensitive measurements, new techniques including a high pressure pump system, multiple impression packers, as well as others have been developed and are being improved. A "curve fitting method" is also proposed to take the pore pressure effect into consideration for the interpretation of the shut-in pressure on pressure-time curves.

The characteristics of the stress spatial distributions have been revealed by synthesizing the stress magnitude distributions for each site. The reverse fault type of a stress state is prevalent in the Kanto-Tokai area. The vertical distribution of the average horizontal stress of all the sites is expressed as $S_{Hav}=0.035h+0.1$, where the unit of stress is MPa and the depth (h) is in meters. With regards to each site, the stress magnitude distribution often shows a heterogeneous state, which is influenced by the inhomogeneity of the rocks or formations which are on a small geological scale unit. In general, the data obtained in hard rocks show that the stresses tend to fluctuate largely.

Stress distributions in two cases, that is, both soft and hard rocks have been investigated. It has been revealed that the main physical mechanism controlling the state of stress in the shallower part of the crust is the yielding of the basement dominated by the frictional sliding of the

micro-cracks. The value of μ=0.57 is the average frictional coefficient which includes both hard and soft rocks. Each measurement site, however, has its own characteristic μ value.

The physical mechanism has to be investigated more precisely in relation to variations of the material properties. The crack densities, which are obtained from the core materials and logging data have been compared with the shear stress distributions. The following phenomena are recognized by this comparison: The number of cracks remains few in a high shear state before the occurrence of frictional sliding. Then the cracks increase in a process where the stress yields to the frictional sliding. In the state "after" this yielding, the mixing of both open and closed cracks occurs. One of the factors which causes an abnormal stress state such as a stress concentration area is suggested by this investigation. To cause this abnormal stress state, a relatively hard area with few or no fractures is needed to continue for an interval with a scale of 30 m or more, as determined from the estimation of the Ashigawa well.

A stress magnitude map reflecting the physical mechanism of controlling the stress distribution has been proposed, that is a shear stress depth-gradient map which reflects the frictional coefficients characteristic for each site. The stress magnitude map has been drawn in order to combine its data with that of the stress orientation map to better understand the fundamental forces which cause earthquakes and crustal deformations.

ACKNOWLEDGEMENTS

The study that follows was based largely on the in situ crustal stress measurement project of the National Research Institute for Earth Science and Disaster Prevention (NIED), which was conducted and developed with Dr. H. Tsukahara, head of the Crustal Dynamics Laboratory. Since the beginning of this project, Dr. Tsukahara's ideas and insights have helped to facilitate very productive research in the development of stress measurement techniques at various depths in the earth's crust.

The NIED, whose former name was the National Research Center for Disaster Prevention, and the director-general Dr. Y. Hagiwara have and do support the ongoing efforts of this research. Dr. Hamada, director, and the members of the Solid Earth Science Division in the NIED, have supported for 13 years this stress measurement research. Their interest in and useful discussions have been fundamental to the experiment efforts described in this study. I want to also thank Dr. H. Takahashi, former director-general of the NIED, for his understanding and support of our project. I would like to extend my appreciation to Professors M. Ohtake and H. Sato of Tohoku University for their cooperative research and stimulating discussions throughout the stress measurement project.

I am deeply grateful to Professor H. Okada of Hokkaido University for his valuable suggestions throughout my work and critical reading of this manuscript. I would specifically like to thank Dr. I. Maeda of the Research Center for Earthquake Prediction, Hokkaido University, for the extensive and beneficial discussions on the topic of borehole experiments and rock properties. Many other fruitful discussions and recommendations about this work have come from the faculty members of Hokkaido University,

specifically Professors M. Kasahara, T. Sasatani, I. Nakanishi and Y. Nishida. Special acknowledgement also goes to Professors K. Nakao and K. Urakami for their continuous advice and encouragement throughout this work.

I would like to extend my thanks to all the staff members of Geophysical Surveying and Consulting Co., Ltd., and Sumiko Consultants Co., Ltd. The interaction with these members has been important in the progress and success of this research. This not only includes helpful scientific discussions but also collaboration in field experiment.

Finally, I want to thank my friend, Ms. L. Bond for her proof reading of this manuscript. And I would most especially like to thank my wife, Nobuko, and three daughters for their love and support during all of the effort it has taken to pursue this goal.

TABLE OF CONTENTS

CHAPTER 1:

INTRODUCTION

Crustal stresses are the most fundamental forces that cause earthquakes and induce crustal deformations. Furthermore, crustal stresses are indispensable factors used in determining designs for underground space constructions, for example oil reservoirs, electrical power stations, nuclear disposal facilities, and hot dry rock geothermal energy plants, to name a few. Consequently, revealing the states of crustal stresses is crucial to the understanding of a number of important questions in earth science, in particular earthquake occurrence mechanisms.

Relationships between the state of stress and the strength of the crust control the occurrence of earthquakes. The state of crustal stress is described by the magnitude and the orientation of stresses induced by the interaction between the overburden stress and tectonic stress. Some stress states can be estimated by surveying various geological phenomena, such as fault movement, dike intrusion and volcanic alignment. However, the stress states obtained by these phenomena practically include stresses which have existed in geological time or over a given measurement interval. Stress variations can also be estimated by multiplying strains obtained from a geodetic survey and the elastic constants of rocks. However, the strain accumulation before the first geodetic survey can not be known, which means that absolute in situ stress values can not be evaluated. Further, the observed crustal strains include not only elastic strain but also inelastic strain, such as plastic deformations caused by fractures.

In situ stress measurements have been involved in determining the present absolute stress value. Remarkable progress has been made in the

measurement techniques in the past fifteen years. The data of stress distribution and stress variance measured by these techniques are of great value in interpreting the mechanisms of earthquake occurrence and/or crustal deformation. Likewise, the discovery of abnormal stress states in space and time do and will continue to contribute to earthquake prediction research. The in situ stress measurement experiment plays an important role as a mediator between the rock mechanical laboratory experiments and the seismic observational research from the view point of the scales of the rocks concerned in these investigations.

Stress measurements by the hydraulic fracturing method have been conducted at 20 sites in the Kanto-Tokai area in the central part of Japan. Stress data have been gathered from boreholes drilled to depths from 100 m to 900 m in various types of rock. The stress data obtained from deep positions and vertical continuous stress measurements in deep boreholes are quite important for earthquake research. Hydraulic fracturing is, at present, the best method to obtain the stress data from various depths and determine the in situ stress levels in deep boreholes.

In this study characteristics and a physical mechanism of in situ stress spatial distribution are revealed from a synthesis of the stress data accumulated thus far. In situ crack density distribution has also been investigated in relation to the stress magnitude distribution on the basis of the physical mechanisms. Taking the results of these investigations into consideration, a stress magnitude map which indicates the regional distribution of the in situ stress relative magnitude is presented.

The contents of each chapter in this study are as follows:

Chapter 2: A proposal of new techniques and interpretations on the hy-

draulic fracturing stress measurement. These techniques have been developed and improved with the hope of obtaining more sensitive measurements with applications for deeper positions.

Chapter 3: An outline of the geological and geophysical features of the stress measurement sites. The locations and the lithology of 21 boreholes at 20 sites are described herein.

Chapter 4: The characteristics of the stress spatial distributions. It has become possible to describe the state of shallow crustal stresses by accumulating in situ measurement data. Each datum, however, is complicatedly affected by regional geological conditions (topography, geological structure, rock type, etc.) and tectonic conditions. In situ stress data measured at each site have been rearranged, and abstracted differences or commonalities on the stress magnitude distributions are presented in hopes of obtaining and understanding the characteristics.

Chapter 5: A study of the main physical mechanism controlling the stress magnitude distributions. Revealing the main physical mechanism is absolutely necessary to consider relationships between the stresses and various geological phenomena. Taking the results of Chapter 4 into consideration, the stress distributions in two cases, that is, both soft and hard rocks have been investigated. Results of this study show that a frictional sliding of cracks in rocks is an important factor affecting the physical mechanism controlling the stress magnitude distributions.

Chapter 6: A study of the relationships between the stress distributions and crustal material properties. It is effective when estimating the stress state at deeper positions if the material properties or well-known physical constants are evaluated in close relation with the stress magnitudes. Investigating the crustal stress distributions conversely contributes to

the understanding of the crustal structures. For these reasons, the physical mechanism has to be investigated more precisely in relation to the variation of the material properties. From the viewpoint of crack density distributions in rocks, the relationships have been analyzed by using sonic velocity data measured on cores and logged in wells.

Chapter 7: A proposal for a map on stress magnitude distribution. A map of stress magnitude has been necessary and desired for conducting research on earthquake occurrence mechanisms and tectonics. The existence of stress provinces has been proposed by compiling the in situ measurement stress orientation data and earthquake focal mechanism data. The facts known suggest that in situ stress data are affected strongly by a relatively wide stress field. However, the magnitude of stresses has not been considered. In this chapter, a stress magnitude map reflecting the physical mechanism of controlling the stress distribution is proposed.

Chapter 8: A summary of the studies presented in this work are reviewed drawing conclusions for the merits of hydraulic fracturing stress measurement and the data obtained with applications for possible earthquake prediction.

CHAPTER 2:

METHOD OF HYDRAULIC FRACTURING STRESS MEASUREMENT

2.1 Position and role

In Japan in situ stress has been measured at various sites since 1977 by both the method of hydraulic fracturing and overcoring in order to obtain basic data for earthquake prediction research (TANAKA, 1985, 1986). The crustal stress data collected for spatial distribution and time variations are absolutely necessary to understand the earthquake occurrence mechanism and plate movement. The detection of abnormal stress states in space and time will consequently contribute to earthquake prediction research. For these purposes, the following subjects have been studied: (1) Improving the methods and developing new techniques for progressively sensitive stress measurements. (2) Measuring the regional and vertical distribution of crustal stresses, and investigating the relations between in situ stress and tectonics, crustal activity, and laboratory experimental data. (3) Observing the stress state variation in time and developing techniques for continuous measurement of it (TANAKA, 1987).

The in situ stress measurement was initiated to recognize rock mass stresses in the 1950's, and the stress relief method has been developed as the most prevalent technique used to date. Stresses acting on a borehole wall are relieved through overcoring, then the elastic strain recovery of a rock is measured. This method has proved to be true in principle and is advantageous because it is accurate. However, it is necessary to multiply the strain and the elastic constants of the overcored material for the

stress calculation. The measurement can be only achieved with delicate electrical transducers, such as strain gauges or linearly variable differential transducers. It is essential that the strain gauges be bonded to the borehole wall. Therefore, it is difficult to take a measurement in a deep borehole at a depth of more than several tens of meters from the surface or from the wall of an underground excavation site. Besides, it is necessary to measure at many points to recognize the stress state of the surrounding wide area because the tests are performed at limited points, and the strength of the rocks must be guaranteed to bear the pressure of the test for a long period of time. These factors are disadvantageous for the stress relief method; accordingly, it is not enough to obtain the stress distributions with depth. However, a lot of stress data were obtained by carrying out this method at various sites. The comparison between the stress data and the tectonic stress field in Japan has become possible by the accumulation of these data, and a close association between them was discovered (HIRAMATSU et al., 1973). These findings have rendered remarkable contributions toward progress in crustal stress research.

As compared with the stress relief method, the hydraulic fracturing method, which originated in the oil industry from oil well stimulation methods, can measure in situ stress at deeper positions. The deepest measurement at present has been taken from a depth of 5,000 m in the Michigan Basin in the U.S.A. (HAIMSON, 1978a). The hydraulic fracturing method has few technical problems because there is no need to have time for stress relief or complicated operations at the borehole bottom. The stress relief method can obtain all stress tensors; however, the hydraulic fracturing method contains assumptions that the vertical stress equals the overlying rock pressure and that two other principal stresses exist in the horizontal

plane perpendicular to the borehole axis (HUBBERT and WILLIS, 1957). From the measurement results, the stresses measured are recognized to be a reflection of the average stresses in rock masses assumed to be extending throughout the surrounding area in spite of this disadvantage. The triaxial rock stress measurement technique, which does not require the above assumptions, has also been proposed recently (OGINO et al., 1984; KURIYAGAWA et al., 1989). This technique is useful for the measurement of rock mass stresses in cavities, but the depth of the well measured was shallow, only several meters. Further, the fact that the stress-depth relation can be evaluated directly is the most important point for the estimation of the stress state around the measurement site. Recently, comparative measurements of crustal stresses by the stress relief method and the hydraulic fracturing method were conducted at the same site (THE RESEARCH GROUP FOR CRUSTAL STRESS IN WESTERN JAPAN, 1986; KOIDE et al., 1986). Some interesting points were noted, such as the fact that shear stress magnitudes obtained by hydraulic fracturing tended to be smaller than those obtained by the relief method (TANAKA, 1987). How to insure that the same measurement conditions exist for both methods is a subject for future study. Still the hydraulic fracturing method is, at present, the best method which allows for the determination and estimation of continuous stress logs with depth. With recent development of measurement techniques, the amount of in situ stress data has rapidly increased. International workshops on hydraulic fracturing stress measurements have been also undertaken in order to advance this method (ZOBACK and HAIMSON, 1983; HAIMSON et al., 1988). The method has been introduced in many countries around the world, such as the U.S.A., Germany, France and China, and the comparison of the measured data

taken from the various countries has been enabled by these international workshops. However, the data obtained are not sufficient to discover or state a general law for estimating the crustal stress state because measurement sites and depths are still limited.

In addition to the above two methods, a few other methods have been developed for measuring the in situ stress in boreholes. The holography method is one in which holographic interferometry is used on the principle of locally relieving the stresses acting on a rock mass by drilling a small hole into the borehole surface and recording the resultant displacement field (BASS et al., 1986). The borehole elongation, also called the breakout method, detects the changes in a borehole cross section that occur as fractures or spalls correlate with the stress azimuth by using instruments such as a dipmeter caliper or borehole televiewer (e.g. PLUB and COX, 1987; ZHENG et al., 1989; MOOS and ZOBACK, 1990). There have been few comparisons or corroborations of the stress magnitude data obtained by these methods because the data itself is quite limited. As indirect methods for estimation of the stress, cored rock samples are used as follows: The acoustic emission method is based on the Kaiser effect in acoustic emission activity depending on the stress level (KANAGAWA et al., 1977, 1981; YOSHIKAWA and MOGI, 1981). The deformation rate analysis method uses the effect of previously applied stresses on the inelastic deformation of rock specimens under cyclic uni-axial compression tests (YAMAMOTO et al., 1990). The time-dependent strain recovery method measures strain recovery immediately after coring with inductive displacement transducers (WOLTER and BERCKHEMER, 1989, 1990). The X-ray method detects residual stresses locked in as the difference of spacing of the crystal lattice planes by X-ray diffraction (FRIEDMAN, 1972; HOSHINO et al., 1978). These methods are useful when in

situ stress measurement in boreholes is difficult, in spite of the fact that they are still considered to be a part of fundamental research. It is necessary to obtain further knowledge about residual stresses and stress history in rocks by comparing the in situ measurement data.

Several geologic phenomena have been used as reliable observational methods to obtain horizontal stress directions other than the stress measurement methods: earthquake focal mechanism, fault-slip, dike intrusion and volcanic alignment (TSUKAHARA and IKEDA, 1987; ZOBACK et al., 1989). However, special attention should be paid to the fact that these geologic phenomena, except for earthquakes, are not always reflected in the contemporary stress field because they include stresses applied over long periods of geologic time.

2.2 Theory

The state of stress around a vertical cylindrical borehole which is drilled into an infinite basement is considered (Fig. 2.1). It is assumed that the crustal stresses represented by the following three principal stresses are acting at any point:

(1) S_V: vertical stress. It acts in a direction parallel to the axis of the borehole.

(2) S_{Hmax}: maximum horizontal compressive stress. It is the maximum stress in the horizontal plane perpendicular to the borehole axis.

(3) S_{Hmin}: minimum horizontal compressive stress. It is the minimum stress in the horizontal plane mentioned above.

Some assumptions are made regarding the materials around the borehole wall.

The borehole wall is impermeable without the existence of fractures. The rock is homogeneous, isotropic, and elastic. The stresses around the borehole can be calculated according to the theory of elasticity.

The stress components in the directions of the tangential (σ_c), radial (σ_r), and vertical (σ_z), which are expressed in the cylindrical coordinates, are given by

$$\sigma_c = S_{Hmax}(1-2\cos 2\theta) + S_{Hmin}[1-2\cos(\pi-2\theta)] \quad (1)$$

$$\sigma_r = 0 \quad (2)$$

$$\sigma_z = S_v \quad (3)$$

where θ is the angle measured counter-clockwise from the S_{Hmax} axis.

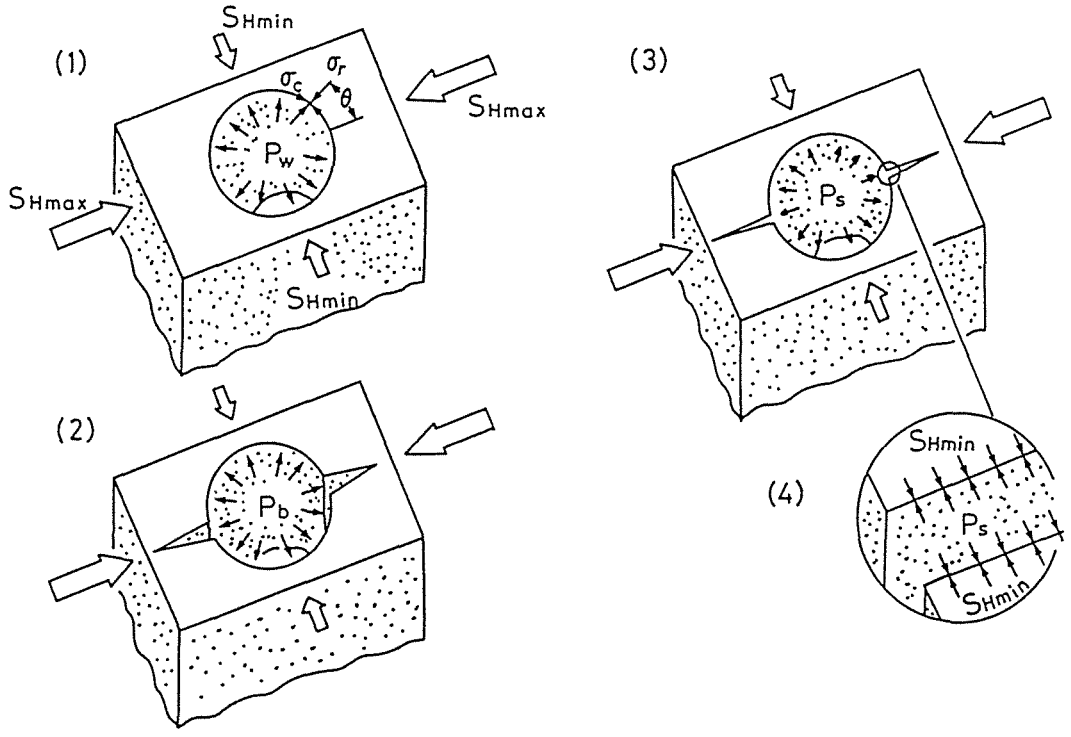

Fig.2.1: Principle of hydraulic fracturing in a borehole.

When fluid is pumped into the borehole, so as to increase the pressure to P_w, Eqs. (1) and (2) can be reduced to

$$\sigma_c = S_{Hmax}(1-2\cos 2\theta) + S_{Hmin}[1-2\cos(\pi-2\theta)] - P_w \quad (4)$$

and

$$\sigma_r = P_w \quad (5)$$

but σ_z does not change. With an increasing P_w, σ_c decreases gradually to become negative. This means that a tensile stress acts in the tangential direction. Fracturing will occur at a point on the boundary of the wellbore where the absolute value of the tensile stress is equal to or greater than the tensile strength of the rock. From Eq. (4) the points

$$\sigma_c = -S_{Hmax} + 3S_{Hmin} - P_w \quad (6)$$

are obtained. This stress can initiate vertical fractures simultaneously at $\theta=0$ and $\theta=\pi$, that is in a direction parallel to that of the maximum principal stress. These fractures extend in both directions symmetrically (Fig. 2.1, (2)). Hence, the S_{Hmax} direction can be obtained by detecting the fracture azimuths (HUBBERT and WILLIS, 1957).

In order to estimate the magnitudes of S_{Hmax} and S_{Hmin}, the relationship between the critical (breakdown) pressure (P_b) necessary to induce a vertical hydrofracture and the two horizontal principal stresses is introduced (SCHEIDEGGER, 1962; KEHLE, 1964; and HAIMSON and FAIRHURST, 1967):

$$P_b = -S_{Hmax} + 3S_{Hmin} + T \quad (7)$$

where T is the tensile strength of the rock in the borehole wall. If a pore pressure (P_p) exists in the rock, and $T=T_0$ when $P_p=0$, T is represented by

$$T=T_o-P_p \tag{8}$$

Hence, from Eq. (6)

$$P_b=-S_{Hmax}+3S_{Hmin}+T_o-P_p \tag{9}$$

When pumping is stopped after causing a hydrofracture, the instantaneous shut-in pressure needed to keep the hydrofracture open is equal to the magnitude of S_{Hmin} perpendicular to the fracture plane (Fig. 2.1, (3)(4)) as

$$P_s=S_{Hmin} \tag{10}$$

Eqs. (9) and (10) will determine the magnitudes of S_{Hmax} and S_{Hmin} by using the values of P_b, P_s, T_o, and P_p. Both values, P_b and P_s, are determined by sensitive measurements of the pressure variation in the borehole. On the contrary, T_o has to be determined by laboratory experiments of rock samples cored from the stress measurement points. Since the strength of the rock, T_o, is often scattered, errors in S_{Hmax} become noticeable. To solve this problem, a series of studies have been done such as those by BREDEHOEFT et al. (1976), ZOBACK et al. (1977), and HAIMSON (1978b) resulting in the proposal of equations without depending on T_o. The hydrofracturing on the condition of a zero tensile strength ($T_o=0$) of a rock can be considered through the process of reopening the fractures by pressurizing repeatedly at the same measurement point in a given borehole. If P_r is the reopening pressure, Eq. (9) is rewritten:

$$P_r=-S_{Hmax}+3S_{Hmin}-P_p \tag{11}$$

Consequently, S_{Hmax} and S_{Hmin} will be determined by Eqs. (10) and (11)

using the in situ measured values of the instantaneous shut-in pressure, P_s, and the reopening pressure, P_r. In the case of a stress state condition of $3S_{Hmin}<S_{Hmax}+P_p$, Eq. (9) has to be used because the experimental detection of P_b is not possible. However, such an extreme case has not been encountered at the measurement sites in Japan. How to detect the values of P_s and P_b sensitively is the most important problem concerning the reliability of the hydraulic fracturing method itself. For these reasons, many measurement instruments and interpretations have been developed and improved. In this study, S_{Hmax} and S_{Hmin} are obtained from Eqs. (10) and (11), and the vertical stress, S_v, is calculated from the weight of the overlying rock:

$$S_v=Dgh \tag{12}$$

where D is the rock density, g is the gravitational acceleration, and h is the depth.

2.3 Measurement procedure and system

The experimental procedure and arrangement of the apparatus for hydraulic fracturing in situ stress measurements are schematically illustrated in Fig. 2.2 and Fig. 2.3, respectively. The main procedure consists of four steps. When an experiment borehole is deeper than 500 m, a reaming and/or casing of the borehole are often necessary to maintain the borehole wall and conduct the experiments safely. Under such circumstances, the following four steps must be followed repeatedly:

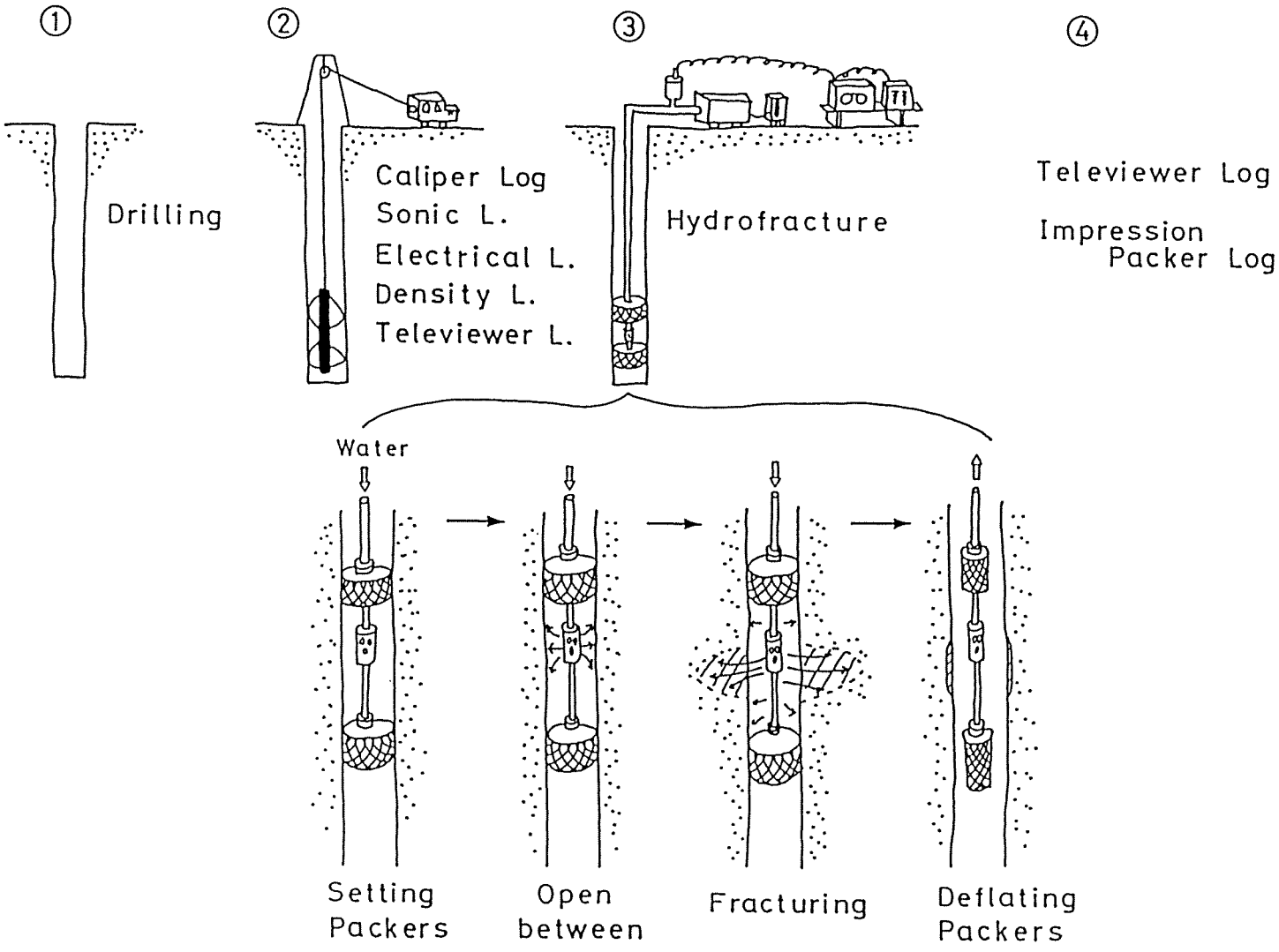

Fig.2.2: Schematic diagram of the procedure of the hydraulic fracturing stress measurement.

Step 1: Drilling of the measurement borehole. - A borehole with a diameter of 159 mm is drilled by a rotary drilling machine. This is true for all cases except the Enzan [EN] well, which was drilled by a wire-line drilling technique with a diameter of 98 mm. Since an extreme borehole deviation from the vertical is restricted by the length of the packers used, constant measurement is necessary and the drilling loads and rates must be controlled frequently to insure the exactness of the borehole inclination. Due to this deviation restriction, some boreholes have had to have corrections made of the deviation. In the case of a 1,000 m class borehole, the permissible limit of the maximum bending angle is within 3^{o} per 20 m, and the maximum angle of the inclination can only be 8^{o} at the bottom. Throughout the drilling process, rock samples are cored from various depths to examine their physical properties in the laboratory.

Step 2: Geophysical well logging and the selection of the measurement points. - Many fractures exist on the borehole wall, and some troublesome phenomena for measurements, such as too large a diameter for the inflatable packers, mud-cakes on the borehole wall, and the deviation, accompany the drilling. Good condition points (about 3 m in length is needed) in the borehole for the hydraulic fracturing are very important for the success of the stress measurement experiments and the survey to find these points is essential. To obtain information of the borehole wall condition, various kinds of well logs, $\gamma-\gamma$ density, sonic wave (form, velocity and intensity), electrical resistivity, ultra-sonic borehole televiewer (BHTV), self-potential and caliper logs, are run throughout the borehole. Since some properties in the borehole or in the formations surrounding the borehole are reflected in these log results, the results are very important for not only finding suitable points for measurements but for studying the control-

ling factors of the crustal stress distribution. Especially, the BHTV log, which gives a visual image of the borehole wall by detecting the reflection strength of ultra-sonic signals from the wall, is very useful to observe the distributions and figures of the fractures.

Step 3: The hydraulic fracturing. - To make the fractures on a borehole wall, a section of the borehole at the measuring depth is sealed off by two inflatable packers, and hydraulic fluid is injected into the sealed off section. The magnitude of the principal stresses may then be determined by the fluid pressure at the time of the fractures opening and shutting-in on the pressure-time records, and the direction of the fractures gives the stress orientation. The interpretations of the stress magnitude determination are described in Section 2.4 and that of the stress orientation is in Section 2.5.

The equipment used is comprised of borehole tools to set the packers, the high pressure injection pumps, and a pressure recording system. Two types of the inflatable packers are used. A conventional packer system which has to be pulled up and down for every experiment at one depth was used during the period of 1978-84. A new packer system (Tam International, Inc.) was adopted in 1985. This system can allow measurements to be carried out at several depths by only one insertion of the packer in the borehole.

An engine drive water pump (<70 MPa, 100 l/min) was used during the period of 1978-81. However, the pump was replaced by an electric motor drive pump because the electric motor has the advantage of constant water injection. Presently, two different capacity plunger pumps, 20 MPa, <53 l/min, and 50 MPa, <16 l/min, are used. Moreover, they are controlled by a frequency inverter with a frequency range of 6-50Hz. This flow rate

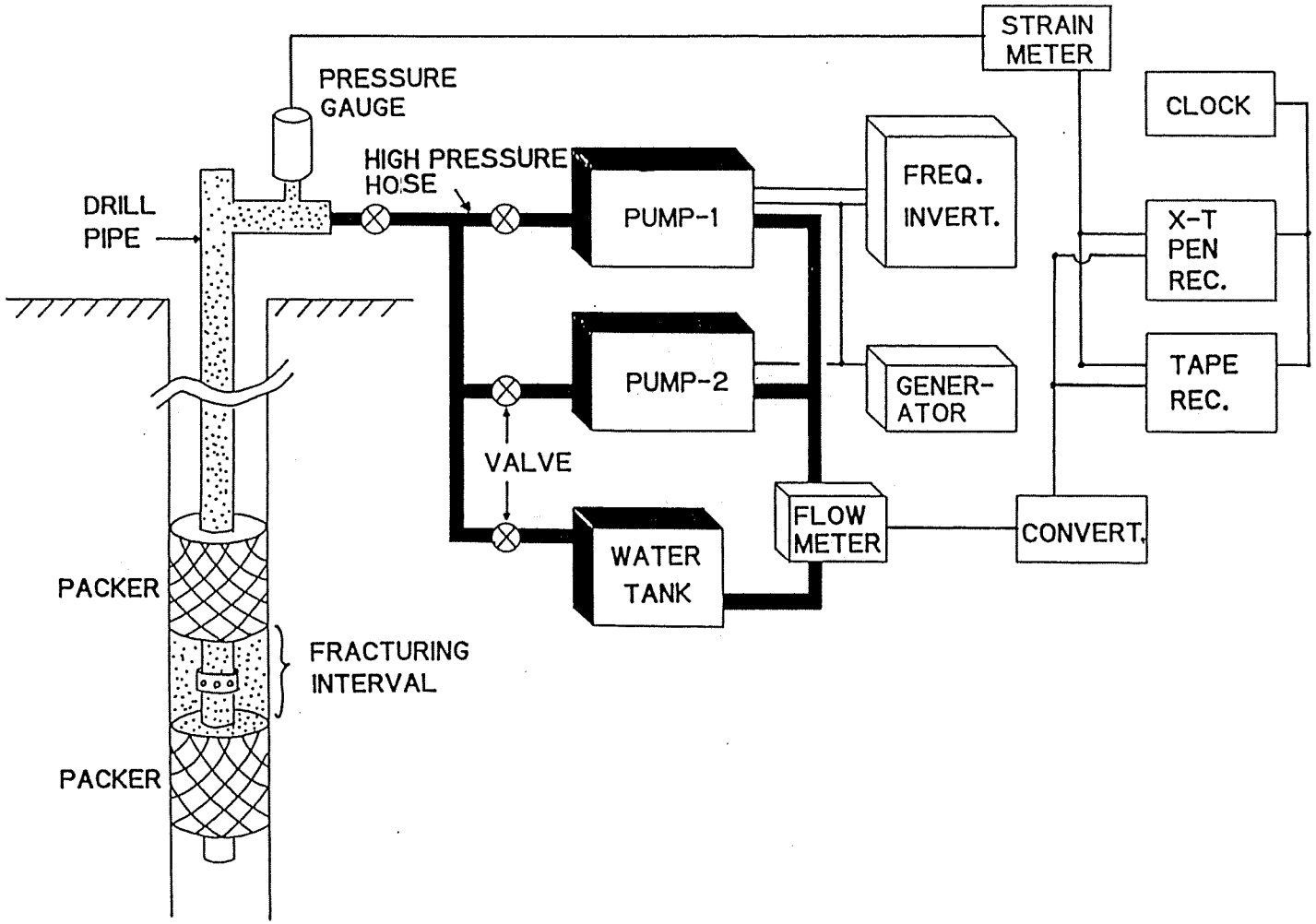

Fig.2.3: Schematic diagram of the hydraulic fracturing measurement system.

controlling system can produce a pressure which is 50 MPa for the entire pressurization system. In the case of very hard rocks, like chert, hydrofractures can not be created within this capacity of 50 MPa. For pressurization pipes between the pumps and the inflatable packers, drill pipes with a diameter of 89 mm are used. It is necessary to check carefully the pressure-resisting qualities for drops in pressure prior to each experiment.

The water pressure is measured at the top of the drill pipe on the surface by using a strain-gauge type pressure transducer, and the flow rate of the water is measured at the suction port of the pumps. For some experiments, a downhole pressure transducer with a logging cable was used and the pressure data were compared with the surface pressure. The difference between both pressure data is smaller than 0.2 MPa. This confirms that a 89 mm diameter drill pipe is large enough to transmit a small change in water pressure from the depth of the hydraulic fracturing to the surface within the experiment depth (TSUKAHARA and IKEDA, 1987). All data is recorded by a magnetic tape recorder with monitoring on a multi-pen chart recorder.

Step 4: Detection of the fractures. - Two types of equipment are used for detecting the hydraulic fracture azimuth, an ultrasonic borehole televiewer and impression packers. Since both kinds of equipment have advantages and disadvantages in and of themselves, it is desirable to use them together. The impression packer can print the fracture traces on the surface of plastic synthetic resin wound around an inflatable packer by impressing it to the borehole wall. Magnetic north is measured by the magnetic direction detector set just above the impression packer. In the case of the BHTV, magnetic north is obtained by the pulse signal generated by the built-in magnetometer. To increase the reliability of orientation detec-

tion, preexamination of the direction detector and repetition of measurements are necessary.

The equipment used for the experiment has been improved and developed for more sensitive and efficient measurements. It is so designed as to bear the experiments throughout the entire depth of a 2,000 m class borehole [TSUKAHARA and IKEDA, 1990]. Details of the inflatable packer, the BHTV, and the impression packer are explained in APPENDIX A.

2.4 Stress magnitude determination

Magnitudes of the in situ stress are obtained from the analysis of a pressure-time record (P-T curve). The P-T curve reflects not only the stress magnitude but the in situ permeability and pore pressure connected with fractures and pores in a given formation. S_{Hmax} and S_{Hmin} are obtained from Eqs. (10) and (11) by using the values of the reopening pressure, P_r, and the instantaneous shut-in pressure, P_s, which are detected on the P-T curve. Under certain circumstances, the very points of P_r and P_s do not appear clearly on the P-T curve. This ambiguity tends to appear in hard rocks at deeper positions. A typical P-T curve (hydrofracture at the depth of 538 m taken in the Hannou [HN] well) is shown in Fig. 2.4, together with its flow rate-time record (F-T curve). The fundamental procedure for the pressurization is explained along the P-T and F-T curves as follows:

(1) Pumping is started at point A and continued at a constant flow rate, so as to increase the pressure to result in hydraulic fracturing. This critical value is the breakdown pressure (P_b). At the same time of the breakdown, the pumping stopped at point B. Thus, water pressure drops down

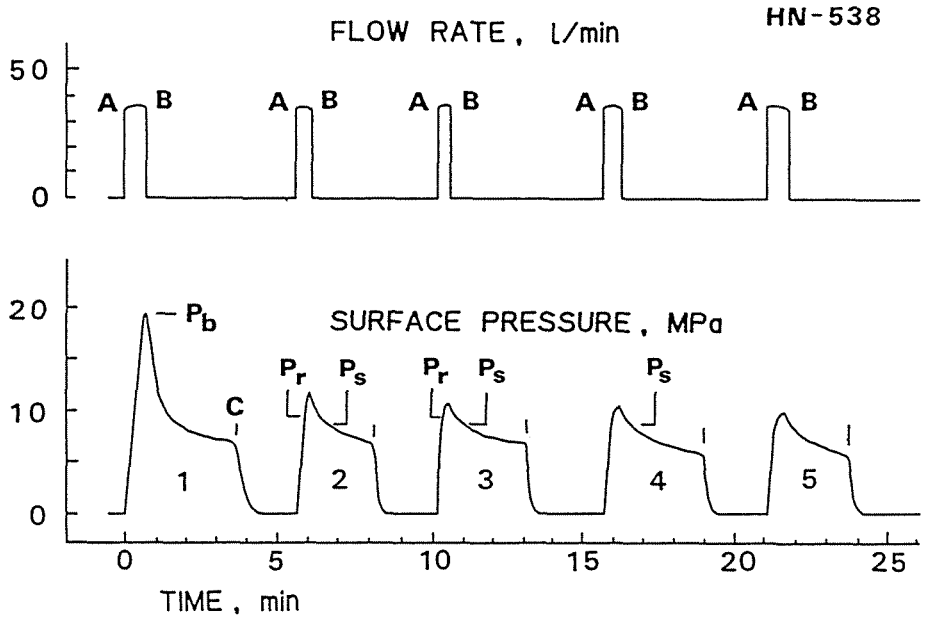

Fig.2.4: Pressure-time and flow rate-time curves. Hydraulic fracturing at the Hannou, [HN], site, depth of 538 m. Pumping was maintained in each injection cycle between points A and B, and water pressure was vented at point C. Pb, Pr, and Ps are the initial breakdown, reopening, and instantaneous shut-in pressures, respectively.

abruptly. Then the pressure decreasing rate changes when the fractures close at the instantaneous shut-in pressure, P_s.

(2) Water is vented at point C. During the process of repressurization, the pressure increasing rate changes when the fractures reopen at the reopening pressure, P_r. The pumping is stopped again at the time when the pressure rises to almost a constant level, then P_s is yielded repeatedly.

(3) Five pressurization cycles are seen in the figure, which yield repeated P_r as well as P_s. If the realization of the developing or closing of the fractures is necessary, it is effective to observe this by changing the flow rate.

All following P-T curves are recorded by using a pressure transducer at the top of the drill pipe on the surface. Therefore, the actual pressure at the experimental depth is obtained by adding the hydrostatic pressure to the recorded pressure.

Determination of the reopening pressure (P_r):

The method for determining the P_r is proposed by ZOBACK et al. (1980) and HICKMAN and ZOBACK (1981), and it is schematically explained in Fig. 2.5. By comparing the first pressurization cycle with the subsequent cycles, the deviation point of the pressure buildup curve between each cycle is detected as P_r. The flow rate is nearly constant during the pressurization of each cycle. In Fig. 2.5, although the clear breakdown P_b is not observed, the hydrofractures are considered to be created at the breakdown pressure and reopened at the deviation point. This idea is fundamentally true, because the pressure increasing rate changes at the time of the fracture's reopening.

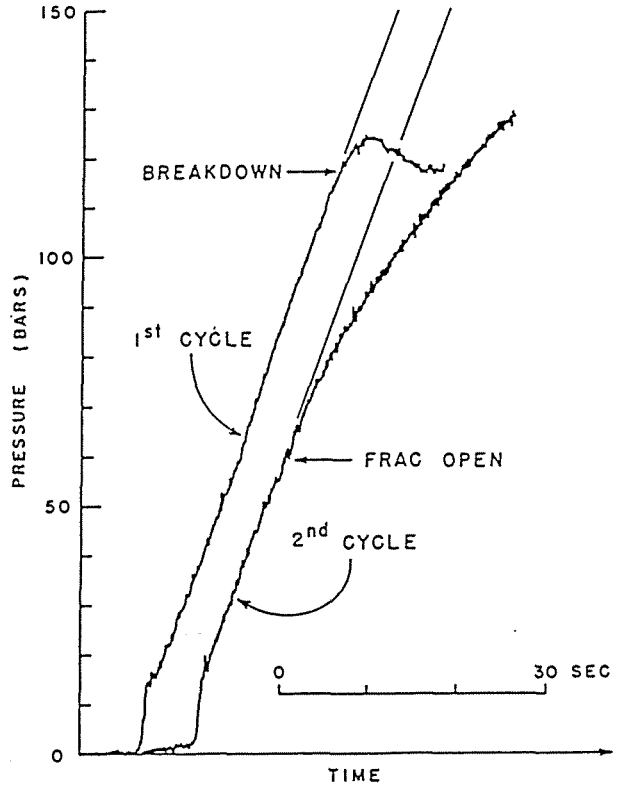

Fig.2.5: Detection of reopening pressure. The deviation of the pressure buildup curve from a constant rate of pressurization is diagnostic of fracture formation on the first cycle and fracture opening on subsequent cycles [after Zoback et al. (1980)].

Fig. 2.6 shows P-T curves taken from the experiment at the depth of 110 m in the Hannou [HN] well, and they are shifted along the abscissa axis, or the time axis. In this case, the value of P_r is determined by the same manner as ZOBACK et al. (1980) in the pressurization cycles from the 2nd to the 5th cycle. The average value of the cycles is adopted for the stress calculation. The influence of the injection flow rate to the P_r value is observed after the 6th cycle. As the flow rate increases at the 6th cycle, the deviation point on the pressure buildup curve becomes a little larger. From the 7th pressurization cycle to the 10th cycle, the P_r value at each cycle decreases by becoming a smaller gradient of the buildup curve. Usually in the experiments, the P_r value is obtained from the pressure curve of several earlier cycles.

The diffusion of water into the rock surrounding the borehole will reduce the reopening pressure due to the decrease of effective pressure in the formation. This is especially true in the vicinity of the fracture. It is difficult to know the absolute value of the pore pressure increase during pressurization. Therefore, a large water injection rate is desirable to minimize the effect of a pore pressure increase because a long injection time to obtain the reopening pressure increases the pore pressure.

Determination of the instantaneous shut-in pressure (P_s):

The identification of the shut-in pressure P_s on the P-T curve is not easier than that for P_r. It tends to be more difficult to detect the P_s points in experiments at deeper positions than shallower ones'. The influence, however, by the difference of rock types is not necessarily distinguished. Various methods for the determination of P_s have been proposed

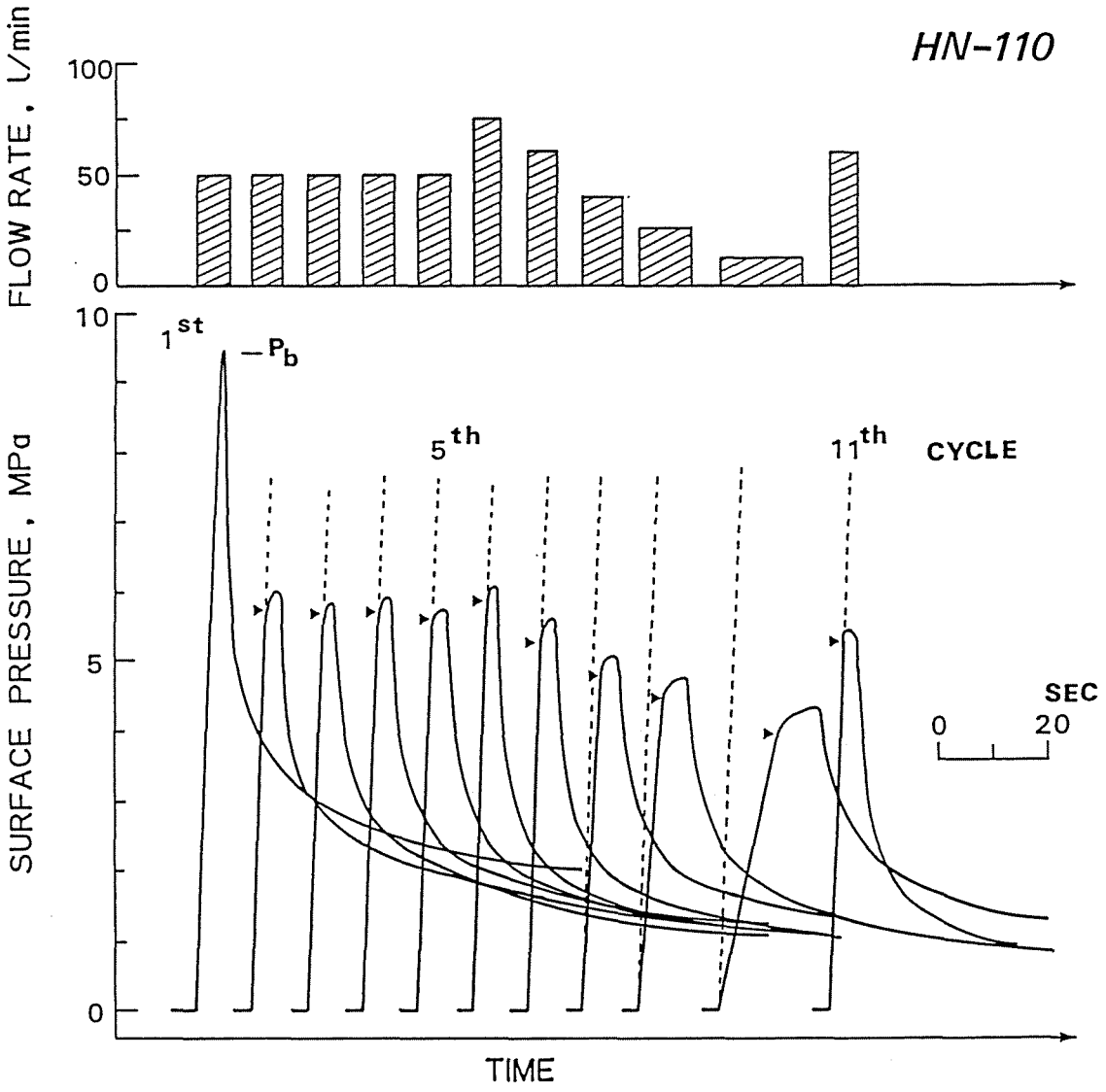

Fig.2.6: Variation of reopening pressures from hydraulic fracturing at the depth of 110 m in the Hannou, [HN], well. Black triangles indicate the reopening pressure. Pressure curves are shifted along the abscissa axis (the time axis). Gradient of the dotted lines is the same as that of the first cycle pressure build-up curve.

(HAIMSON et al., 1988). HAYASHI and SAKURAI (1989) analyzed the closure process after a shut-in of the cracks on the basis of the linear theory of elasticity and also on the basis of linear fracture mechanics. According to their study, the pressure decay characteristics of shut-in curves are primarily governed by the leak-off rate, the equipment compliance and the partial crack closure. The P-T curves obtained from actual field experiments are influenced by various combinations of these factors. So it is rare to realize an apparent P_S inflection point such as is shown on a simulation curve. Moreover, the influences of fracture and pore pressure, induced by repeated pressurization, cannot be neglected. A new "Curve Fitting Method" is proposed to take the pore pressure effect into consideration for the interpretation of the shut-in pressure point (IKEDA and TSUKAHARA, 1989).

The P-T curve after the shut-in is governed by steady-state diffusion into the formation through the borehole wall and fractures. Therefore, in the case of multiple pressurizing at the same depth as shown in Fig. 2.6, the P-T curves after shut-in should coincide with each other. However, the P-T curves do not usually coincide. This is mainly caused by the pore pressure change and by change in the fracture shape. If the difference between the P-T curves is due only to the pore pressure change, ΔP, the P-T curves will coincide with each other when the curve is shifted by ΔP.

These phenomena are examined by moving the P-T curve parallel to both the P and T axes to fit the last part of the curve. Fig. 2.7 shows the fitted curves, which are the same records as shown in Fig. 2.6. The P-T curves of the 3rd cycle follow the same trace as that of the 2nd cycle after the maximum pressure, and they lie upon the 1st cycle curve at point A. Point A of the 2nd cycle should be adopted as the P_S value. On the other

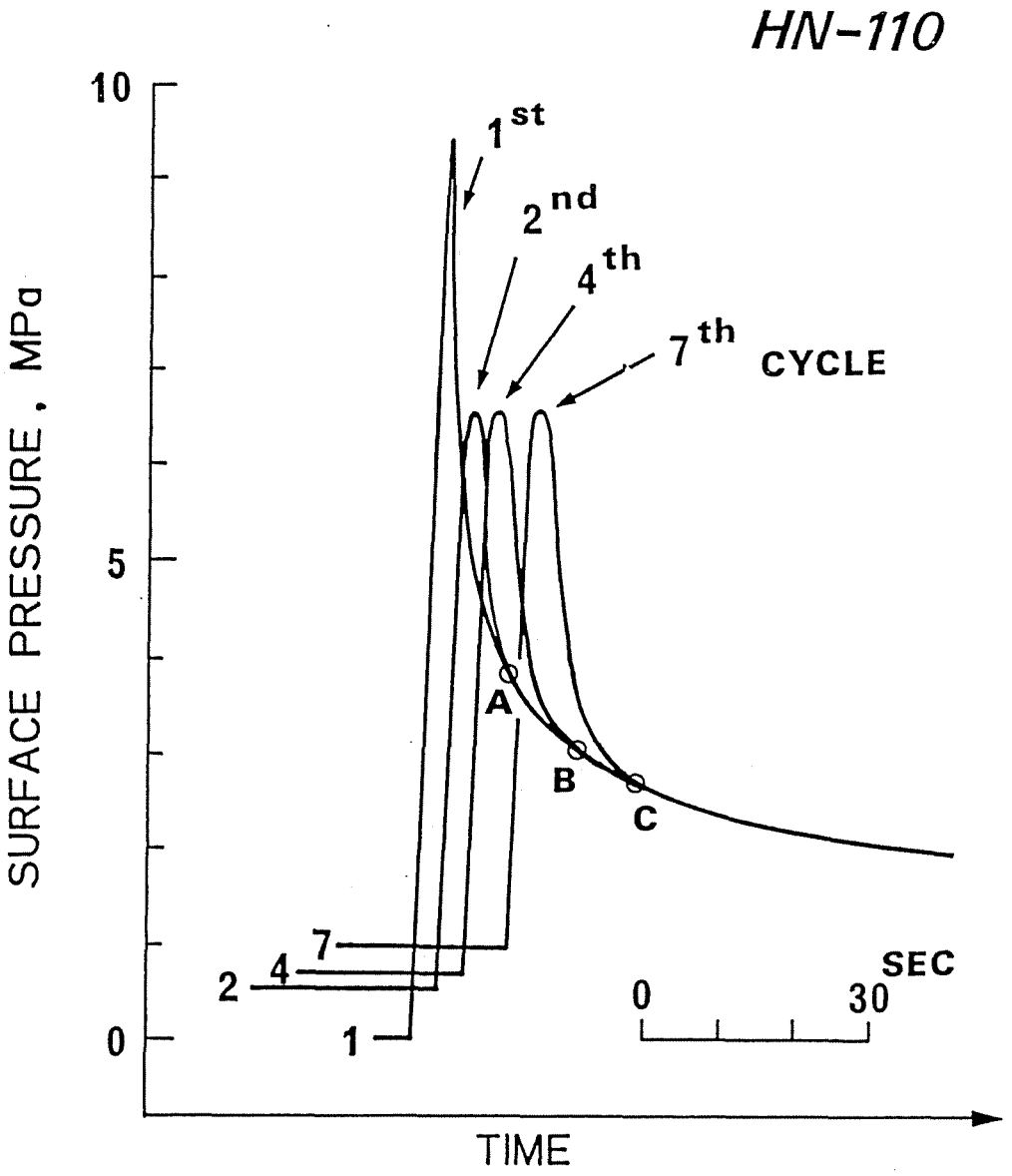

Fig.2.7: "Curve Fitting Method" for the interpretation of the shut-in pressure. The curves from the same records as shown in Fig.2.6 are shifted suitably in order to fit them to the 1st cycle. Note the agreement of the curves below point A among the 1st, 2nd and 3rd cycles. Below point B, the curves of the 1st to 6th cycles coincide with each other; and below point C, all of the curves coincide. A is the intrinsic shut-in point, and B and C are secondary ones, suggesting the occurrence of a new fracture system.

hand, from the 4th to 6th cycle the curves overlap and lie upon the 1st cycle at point B. Moreover, the curves from the 7th to 11th cycle lie upon the 1st cycle at point C. This feature suggests that new fractures occur between the 3rd and the 4th cycles and between that of the 6th and the 7th. The origins of the P-T records vary with the pressurization cycle. The difference of the origin value indicates the pore pressure variation surrounding the borehole, especially in and around the fracture. In this case, the pore pressure change is about 1 MPa from the 1st cycle to the 7th cycle.

2.5 Stress orientation determination

The hydraulic fractures are observed by both the ultrasonic borehole televiewer (BHTV) and impression packers for the determination of the stress orientation, as described in Section 2.3. Fig. 2.8 shows an example of borehole wall development images from a depth in the area around 263 m in the Nishi-Izu [NI] well. The left-hand and right-hand records were taken before and after the hydrofracturing, respectively. The ultrasonic reflection strength from the borehole wall is strong at the white parts, and weak at the black parts on the picture. Newly created fractures are seen on diametrically opposite sides of the borehole in the right-hand record. The N in the picture indicates magnetic north, with a declination of 6^{o} to the west. Fig. 2.9 is a photo of an impression taken from the area around 225 m in the Okabe [OK] well. A printed long fracture trace is seen between the directions of north (N) and west (W). The impression pressure and its holding time in this case is about 9 MPa and 30 minutes, respectively. The depth of the fractures cannot be measured by the BHTV and the impression

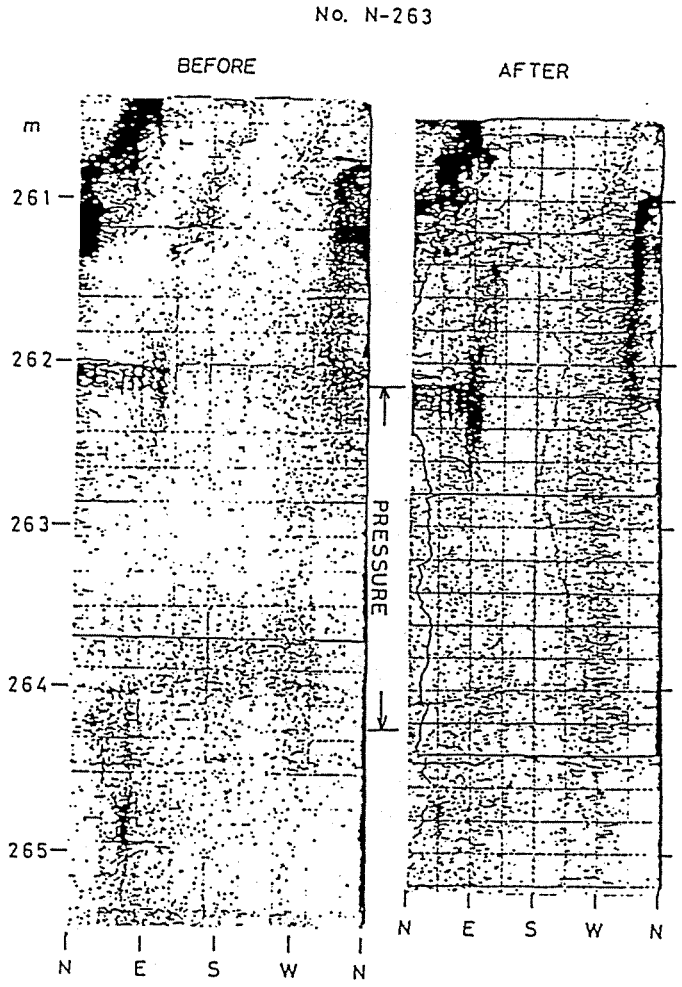

Fig.2.8: Borehole wall development images by ultrasonic borehole televiewer. Before and after hydraulic fracturing around the depth of 263 m in the Nishi-Izu, [NI], well. Newly created fractures are detected in the "after" hydraulic fracturing picture. N indicates magnetic north.

packers. The fracture length is sometimes over the length of the pressurization interval, about 2 m. The fracture width is observed from 1 mm to several mm by observing the thickness of the pinched rubbers on the impression packer surface, and from this a direct relationship can be drawn to the fracture's width. The fractures ordinarily extend in both directions symmetrically as expected by the theory explained in Section 2.2. However, as seen in Fig. 2.8 and 2.9, the fracture traces are not straight and not always parallel with the distance of 180°. A mean value of the fracture

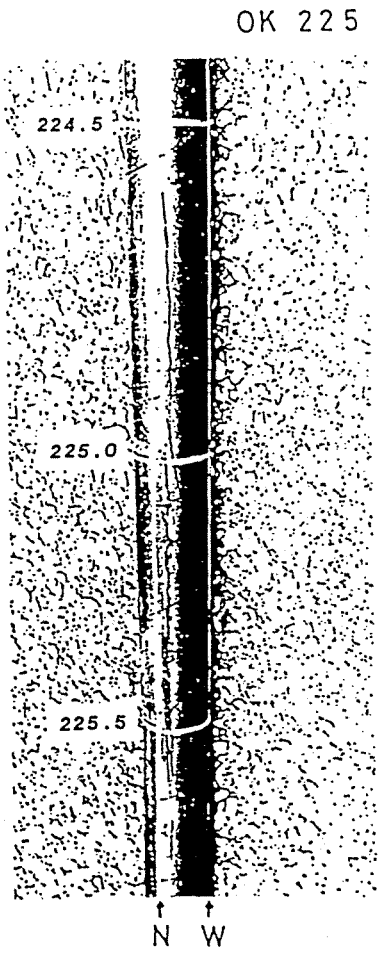

Fig.2.9: Fractures printed on the surface of an impression packer after hydraulic fracturing around the depth of 225 m in the Okabe, [OK], well. N indicates magnetic north.

azimuth is adopted as the orientation of the S_{Hmax}. It is assumed from the fracture traces that the uncertainty in the mean value of the azimuth is approximately 20^{o}. This is not a statistical measure but is merely an indication of the confidence in the accuracy of the mean value.

An observation of acoustic emissions (AE) is effective to monitor the hydrofracture's occurrence and development (IKEDA et al., 1978; IKEDA and TSUKAHARA, 1983). The frequency, epicenter, and characteristics of the AE, which are accompanied by the occurrence of micro-fractures in rocks, are important not only to study the fracture process but also to determine the stress magnitude and orientation. The observation condition, however, is so restricted that full observation of the AE is not usual.

CHAPTER 3:

MEASUREMENT SITES AND LITHOLOGY

The sites of hydraulic fracturing stress measurements are marked with black circles in Fig.3.1. Six sites are added to the sites previously measured by TSUKAHARA and IKEDA (1987). Table 3.1 shows the location of the sites, depth of the measurement wells, depth of the experiment points, and experiment year and month. The outline of the lithology and the results from density and P-wave velocity logs, which are closely related to the physical properties of the rocks constituting the boreholes, are also summarized in Table 3.1.

The Kanto-Tokai area stands at the junction of three plates: the Philippine Sea (PH), Pacific (PA), and Eurasian (EU) plates, as illustrated in the inserted figure in Fig.3.1. White arrows indicate the direction of the relative movement among the three plates. The PH plate is considered to be moving northwestward relative to the EU plate and subducting at the Nankai (NAN), Suruga (SU), and Sagami (SA) troughs under the EU plate, while the PA plate is moving westward and subducting at the Japan (JA) trench under the EU plate. The extremely complicated tectonic features of this area are also shown on land in the tectonic lines longer than 200 km: the Itoigawa-Shizuoka Line (IS) and the Median Tectonic Line (MT).

The lithology of the wells is extremely diverse, such as sandstone, mudstone, tuff and granitic rocks. Since the center part of the Kanto plain has both thick and soft sediments more than 3,000 m deep, there is little data available for this area. The measurement points in each well are also not equally distributed throughout the entire depth of the wells. The possibility of hydraulic fracturing is restricted by the hardness of rocks

and the existence of fractures in the parts of the well used for pressurization. For instance, in the case of the Tsukuba well, [TK], the measurement could not be taken in the interval shallower than the depth of 410 m because of the low hardness in the mudstone and sandstone of Quaternary age, but data were obtained in the basement granitic rocks of Cretaceous age at a level deeper than 410 m. The youngest sedimentary rocks in which stress data have been obtained are of Early Pliocene age of the Chikura well, [CK]. The detailed lithologies and log results of each well are explained in APPENDIX B.

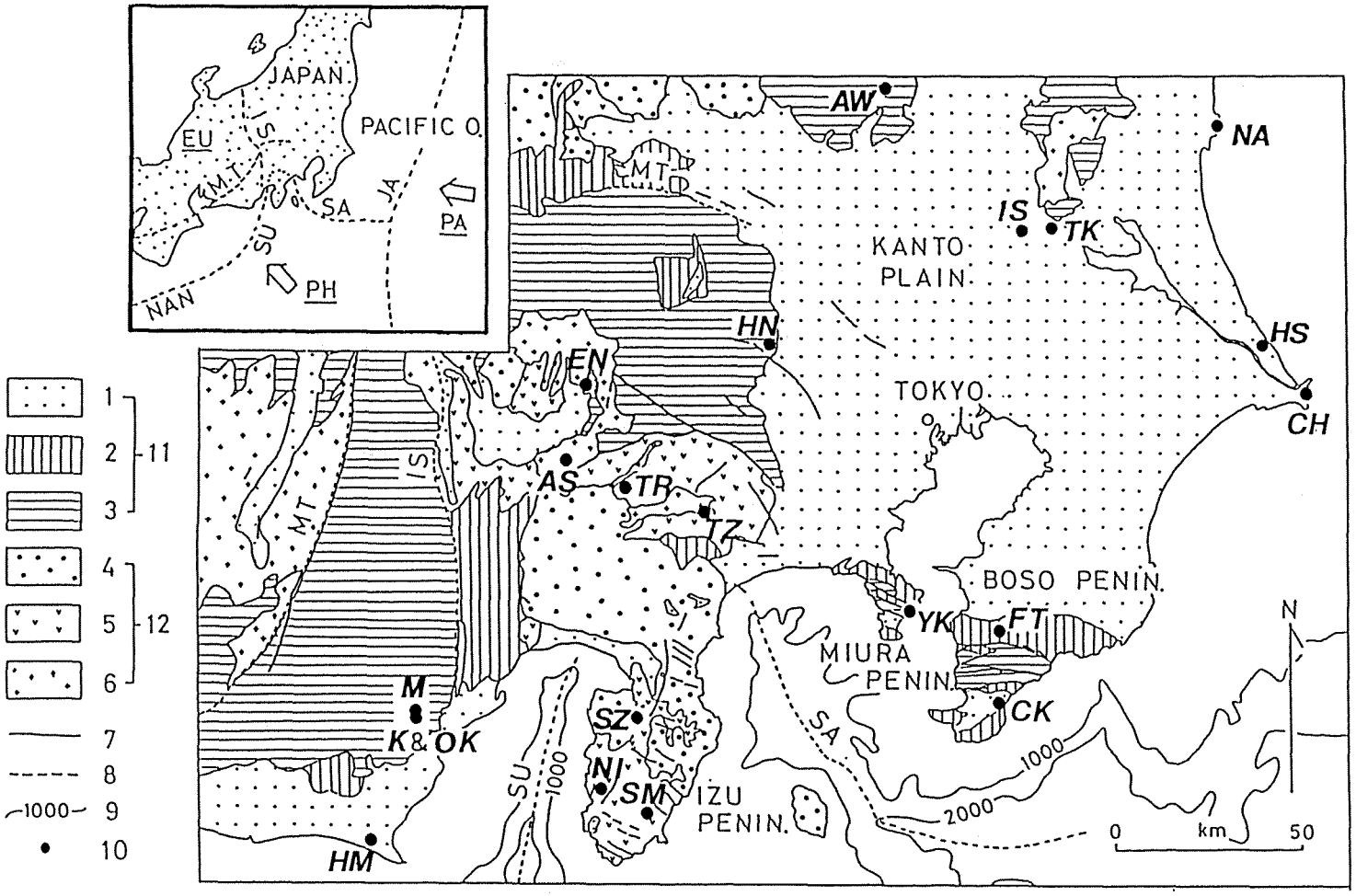

Fig.3.1: Stress measurement sites and their geological settings in the Kanto-Tokai area. 1:Post-Miocene; 2:Miocene; 3:Pre-Miocene; 4:Quaternary extrusives; 5:Tertiary extrusives; 6:Intrusive rocks; 7:Active faults; 8:Main tectonic lines; 9:Sea bottom contours; and 10:Stress measurement sites. See text for the explanation of the tectonic situation of the area mapped in the inserted figure.

Table 3.1 (a): HYDRAULIC FRACTURING EXPERIMENT SITES

Site	Location lat. (N) long. (E) height(m)	Well depth (m)	Exper. depth (m)	Exper. Mon/year	Rocks (Age)	Density (g/cc) (methods)	P-wave velocity (km/sec)
Hamaoka [HM]	34°37'31" 140°10'02" 20	250	119-247	3/1984	Ms. with sandy beds (Neogene)	2.0(L)	2.5-3.0
Okabe-M [M]	34°57'56" 138°15'22" 80	100	81-90	3/1978	Ms. with many claycy beds (Paleogene)	n.m.	n.m.
Okabe-K [K]	34°55'47" 138°16'08" 40	100	77-95	2/1978	Ss. with some claycy beds (Paleogene)	n.m.	n.m.
Okabe-OK [OK]	34°55'47" 138°16'08" 40	450	218-429	3/1981	Ss. with some clayey beds (Paleogene)	2.4(L)	4.3-5.3
Tsuru [TR]	35°30'47" 138°53'12" 598	450	75-389	2/1983	Tuff and tuff breccia with some altered clayey rocks (Miocene)	2.7(L)	3.5-5.5
Ashigawa [AS]	35°32'58" 138°42'35" 1050	200	128-193	3/1986	0-62m:diorite; 62-113m: basalt; 113-203m:porphyrite (Miocene)	2.6(L)	4.2-5.5 (120-200m)
Enzan [EN]	35°44'19" 138°43'26" 465	200	103-186	3/1990	0-50m:gravel; 50-200m:granodiorite (Neogene)	2.55(L:0-80m) 2.75(L:80m-)	2.5-6.0(0-80m) 5.2-6.0(80m-)
Tanzawa [TZ]	35°26'28" 139°07'08" 700	140	91-136	11/1988	quartzdiorite with many cracks(Neogene)	2.45(L)	2.5-6.0
Nishi-Izu [NI]	34°46'39" 138°47'48" 15	450	263-436	1/1979	Indurated tuffaceous Ss. with several clayey beds (Miocene)	2.6(S)	4.2-5.2
Shuzenji [SZ]	34°56'46" 138°55'08" 149	450	136-395	12/1981	Tuff and tuff breccia with many altered clayey rocks (Miocene)	2.2(L)	2.2-4.0
Shimoda [SM]	34°43'03" 138°56'55" 30	450	71-444	3/1982	Tuff and tuff breccia with some altered clayey rocks (Miocene)	2.2(L)	3.0-4.8

Table 3.1 (b):

Site	Location lat. (N) long. (E) height(m)	Well depth (m)	Exper. depth (m)	Exper. Mon/year	Rocks (Age)	Density (g/cc) (methods)	P-wave velocity (km/sec)
Yokosuka [YK]	35°12'28" 139°42'02" 10	450	107-200	12/1980	Ms. with many pre-existing fracs. (Miocene)	2.1(C)	2.5-3.0
Chikura [CK]	34°58'03" 139°56'57" 71	800	94-784	12/1984 - 1/1985	Ms. and Ss. (Early Pliocene)	2.0(L:0-400m) 2.1(L:400m-)	2.7-3.0
Futtsu [FT]	35°10'23" 139°57'43" 60	450	101-437	12/1979	Ms. and Ss. (Miocene)	2.0(L)	2.5-3.0
Tsukuba [TK]	36°07'21" 140°05'36" 26	600	435-599	3/1983	0-410m: Ms. and Ss. (Quaternary); 410-600m: granitic rocks with many cracks(Cretaceous)	2.0(L:0-410m) 2.5(L:410m-)	1.7-2.5(0-410m) 4.0-5.5(410m-)
Ishige [IS]	36°06'28" 139°59'33" 15	900	438-873	2/1986	0-518m: Ms. and Ss. (Quaternary); 518-900m: granitic rocks with many cracks(Cretaceous)	2.0(L:0-518m) 2.5(L:518m-)	1.9-2.4(0-518m) 3.0-4.5(518m-)
Nakaminato [NA]	36°21'36" 140°37'27" 20	450	217-434	3/1980	siltstone (Cretaceous)	2.3(L)	3.2-4.0
Hasaki [HS]	35°49'33" 140°44'08" 5	800	519-792	2/1984	Ms. and Ss. 0-50m(Quaternary) 50-450?m(Pliocene) 450?-800m(Miocene)	1.9(L:0-650m) 2.1(L:650m-)	2.4-2.5(0-500m) 2.5-3.0(500-600m) 3.0-3.5(600m-)
Choshi [CH]	35°42'20" 140°52'15" 5	450	60-391	3/1979	Shale with many pre-existing fracs and clayey beds(Cretaceous)	2.2(S)	2.5-3.5(0-330m) 3.5-5.0(330m-)
Hannou [HN]	35°50'33" 139°17'59" 178	800	58-761	11/1986 - 2/1987	Shale and Ss. with some chert(Pre-Neogene)	2.5(L)	3.0-4.0(0-400m) 2.0-3.0(410-460m) 2.5-4.5(460m-)
Awano [AW]	36°28'46" 139°37'16" 151	800	51-773	7/1987 - 9/1987	Ss. and Slate (Paleozoic)	2.45(L)	3.8-4.5(20-600m) 3.0-5.0(600m-)

Ss: sandsone; Ms: mudstone.
L: log data; C: core specimen; S: surface rock specimen; n.m.: not measured.

CHAPTER 4:

MEASUREMENT RESULTS

4.1 Measurement data and stress magnitudes

The P-T and F-T curves are obtained from each stress measurement depth in each borehole. In this section, measurement data and analyzed results are described from the measurement results taken from the Enzan [EN] well, where vertically dense measurements were conducted and continuous core samples were obtained.

The stress measurements were conducted at 16 measurement depths below 80 m in the [EN] well. The P-T and F-T curves from 13 measurement depths out of the 16 depths have good features for the stress magnitude analyses. However, it is important to note that the stress magnitude was obtained in only 9 depths for several reasons. For example, Fig. 4.1 shows the P-T and F-T curves from these 9 depths. The points which are interpreted as the breakdown pressure, P_b, the reopening pressure, P_r, and the instantaneous shut-in pressure, P_s, are indicated on these curves. To obtain the accurate stress magnitude, it is necessary to interpret P_r and P_s concerned with the exact vertical hydrofractures extending parallel to the borehole center axis. In the case of this [EN] well, the inflection points of P_r and P_s are not apparent. Therefore, it is difficult to recognize the moment when the vertical or horizontal fractures are initiated during the pressurization. It is rare that the P-T curve traces the theoretical curve under ideal conditions as shown through many experiments. This is because the P-T curve is influenced by various combinations of many factors: the pressurization system (pump, packer, and pressure lines), the pressurizing time, the flow

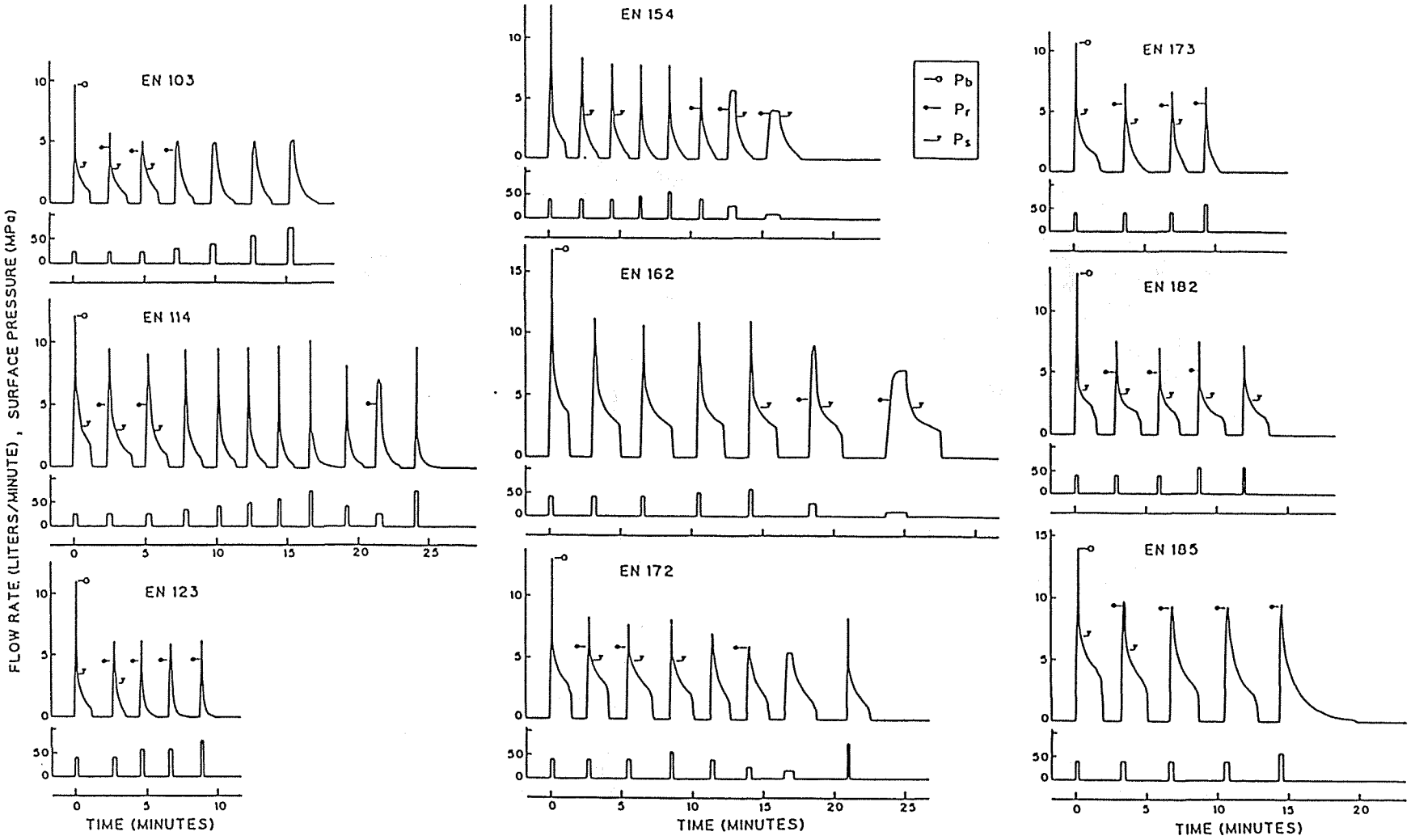

Fig.4.1: Pressure and flow rate against time curves obtained from the experiments in the Enzan, [EN], well. The number above each record indicates the test depth. Surface pressure is measured by transducers on the injection pipe line. Pb:initial breakdown pressure; Pr:reopening pressure; and Ps:instantaneous shut-in pressure.

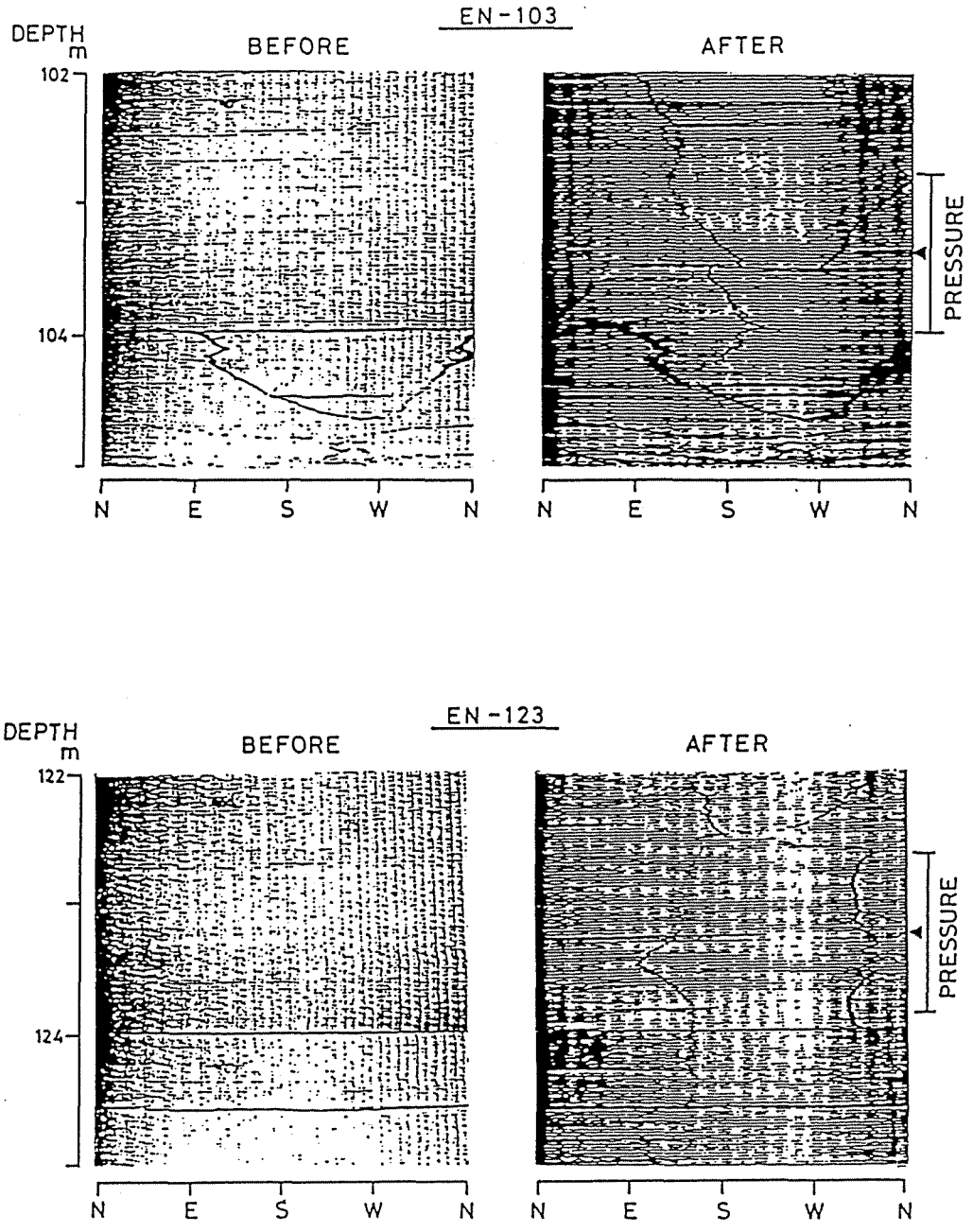

Fig.4.2: Ultrasonic borehole televiewer records before (left-hand) and after (right-hand) the hydraulic fracturing around the depths of 103 m and 123 m in the Enzan well.

rate, and the borehole wall conditions. The P_r is detected basically by reading the deviation point from the linear part of the pressure buildup curve. Special attention must be paid to the flow rate in this analysis.

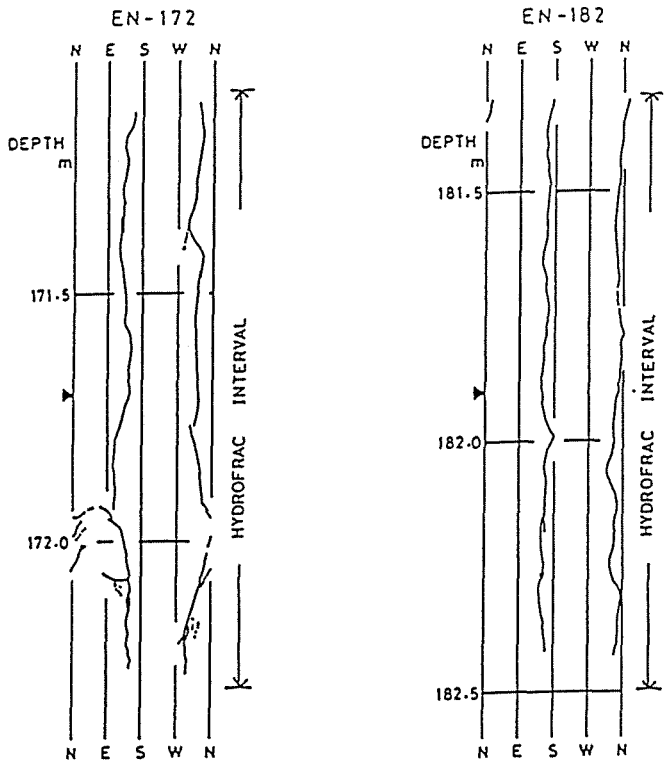

Fig.4.3: Copies of fractures printed on the surface of impression packers after the hydraulic fracturing around the depths of 172 m and 182 m in the Enzan well.

This is because, if the flow rate is not suitable for the hydrofractures' reopenings, an over-estimation of the P_r value can be caused by an over-flow rate. This tendency is stronger in the [EN] well probably because of the small diameter of the well. By changing the flow rate, as seen on the F-T curves in Fig. 4.1, it is possible to read the correct P_r value under the suitable flow rate for each experiment point. The P_s value is detected by the "Curve Fitting Method". Moreover, the vertical hydrofractures must be discriminated from the horizontal and/or preexisting fractures by the total information obtained from the core, well logs, the BHTV and the impression packer.

The results from 4 depths out of the 13 depths seemed to be caused or influenced by existing fractures according to the results of the BHTV and the impression packer. The stress magnitudes obtained from 4 out of the 9

depths are absolutely reliable, that is only the vertical fractures are detected. The rest of the 5 depths' results include both the vertical and the horizontal fractures. For example, in the BHTV's results of Fig. 4.2, the influence of the preexisting fractures is seen to be strong in the 103 m-depth (EN-103) experiment, but the vertical hydrofractures excel in the 123 m-depth's. In the impression packer's results shown in Fig. 4.3, a horizontal fracture is also recognized. The in situ stress depth distribution calculated in the [EN] well is shown in Fig. 4.4. The data indicated by the circles are superior to the data by the triangles in quality. Both the circled and the triangulated data are essentially regressive to straight lines, except for in the case of the 182 m depth's data. In the case of the triangulated data, it is difficult to identify the moment when the vertical or horizontal fractures are created. However, it appears from the above information that they reflect in situ stress. The depth of 182 m is an area where the existing fractures are few but the electrical resistivity is low. Also, the azimuth of the hydrofractures at 182 m is from 25° to 35° different from other depths (see Fig. 4.3). From this it may be inferred that the stress magnitudes obtained from 182 m characterize this depth. Both stresses, S_{Hmax} and S_{Hmin}, increase with depth almost linearly. The best fit regression lines obtained by the least squares method are denoted by broken lines:

$$S_{Hmax}=7.2\times10^{-2}h-2.2$$

and

$$S_{Hmin}=4.9\times10^{-2}h-1.7$$

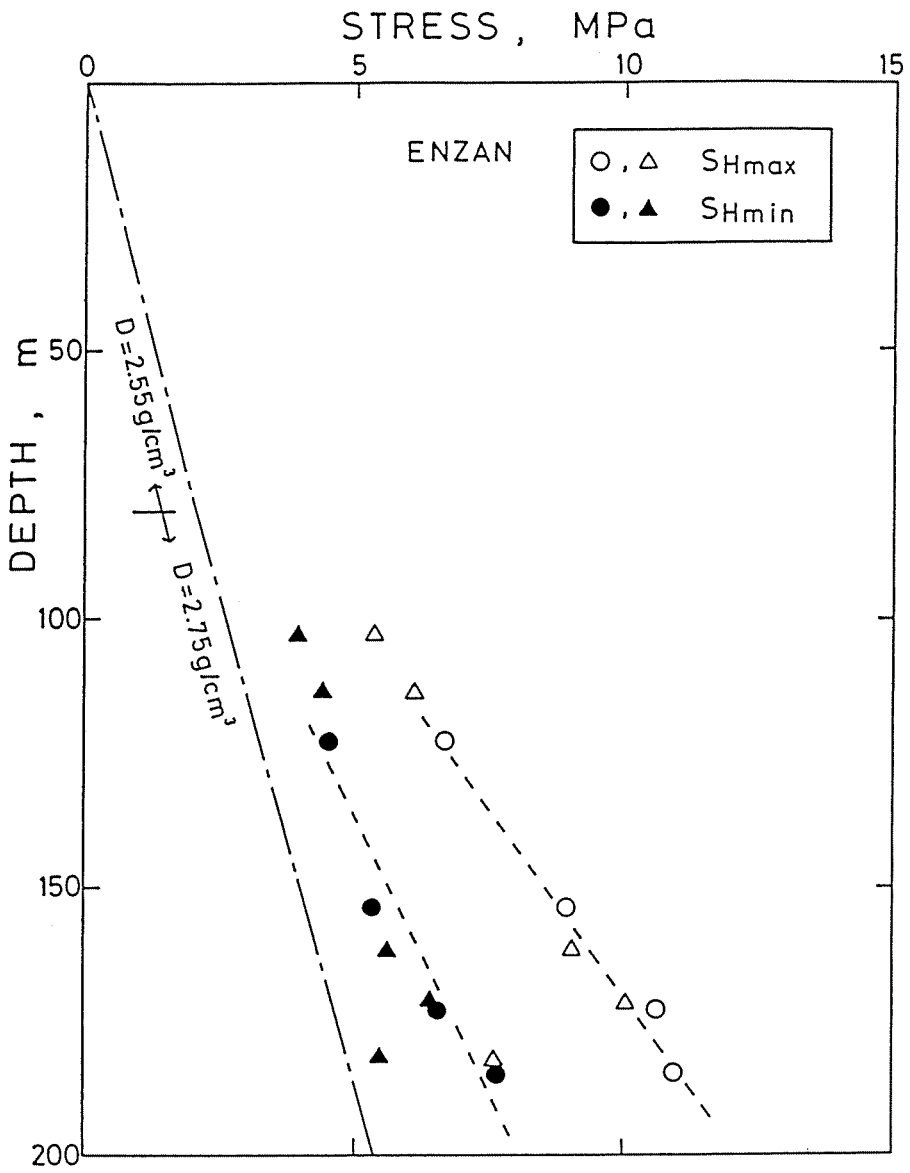

Fig.4.4: In situ stress depth distribution in the Enzan well. Data are classified into two groups by detail analysis of fracture occurrence. The circles are superior to the triangles in quality. Dashed lines indicate the best fit obtained by the least squares method using the data as shown from the circles.

where the unit of the stresses is MPa, and h is the depth in meters. The vertical stress is calculated by Eq. (12) using the rock densities, D=2.55 g/cm^3 (for h=0~80 m) and D=2.75 g/cm^3 (for h=80~200 m), taken from the logging data:

$$S_V = 2.55 \times 10^{-2} h \qquad \text{(for h=0~80 m)}$$

$$= (2.75h - 16) \times 10^{-2} \qquad \text{(for h=80~200 m)}$$

The orientation of the maximum compressive stress is N50°W, which is obtained from the average azimuth of the four depths circled.

The water pressure data P_b, P_r, and P_s, and stresses S_{Hmax}, S_{Hmin}, and S_V, from all 21 measurement sites, are summarized in Table 4.1. S_{Hmax} S_{Hmin} are obtained by Eqs. (10) and (11) in which the pore pressure P_p is taken as the hydrostatic pressure at that depth because the water table was near the surface at all sites. S_V is calculated by Eq. (12) by using the average rock density D of each site. The maximum shear stress, S_S, and effective normal stress, S_N, are also shown in Table 4.1. If S_{max} and S_{min} are defined as the maximum and minimum stresses of three principal stresses, respectively, and the shear planes are assumed to make an angle of 45° from these S_{max} and S_{min} axes, S_S and S_N are given by:

$$S_S = (S_{max} - S_{min})/2 \tag{13}$$

$$S_N = (S_{max} + S_{min})/2 - P_p \tag{14}$$

(e.g., JAEGER and COOK, 1976). Both stresses are fundamentally important stresses for the consideration of the stress distribution or earthquake occurrence mechanisms.

Table 4.1 (a): HYDRAULIC FRACTURING DATA AND IN SITU STRESSES

Depth (m)	Hydrofrac. data (MPa)			Stress(MPa)					Frac. azimuth
	Pb	Pr	Ps	SHmax	SHmin	Sv	SS	SN	
Hamaoka[HM], D=2.0									
119.0	10.8	4.7	3.2	3.7	3.2	2.4	0.65	1.86	N70°W
178.0	15.4	4.8	4.4	6.6	4.4	3.6	1.50	3.32	N75°E
247.0	15.0	5.6	5.1	7.2	5.1	4.9	1.15	3.58	-
									Av. N90°W
Okabe-M[M], D=2.4									
81.0	4.9	4.1	3.8	6.5	3.8	1.9	2.30	3.39	-
83.0	6.7	4.2	3.7	6.1	3.7	2.0	2.05	3.22	-
90.0	5.9	3.6	3.5	6.0	3.5	2.2	1.90	3.20	-
Okabe-K[K], D=2.4									
77.0	9.5	3.8	3.2	5.0	3.2	1.8	1.60	2.63	-
95.0	11.8	8.0	5.3	7.0	5.3	2.3	2.35	3.70	S35°W
Okabe-OK[OK], D=2.4									
218.0	15.1	9.9	7.2	9.5	7.2	5.2	2.15	5.18	N50°W
221.0	16.8	10.5	8.3	12.2	8.3	5.3	3.45	6.55	N50°W
225.0	12.8	9.7	7.2	9.7	7.2	5.4	2.15	5.30	N45°W
304.0	15.3	12.5	10.8	16.9	10.8	7.3	4.80	9.06	-
352.0	11.9	10.6	10.7	18.0	10.7	8.4	4.80	9.68	-
405.0	17.7	11.9	12.1	20.4	12.1	9.7	5.35	11.00	-
409.0	13.1	13.1	12.6	20.6	12.6	9.8	5.40	11.11	-
413.0	12.5	11.6	11.1	17.6	11.1	9.9	3.85	9.62	-
417.0	21.2	13.7	13.2	21.7	13.2	10.0	5.85	11.68	N55°W
425.0	19.0	17.9	13.7	18.9	13.7	10.2	4.35	10.30	S85°W
429.0	20.1	17.7	13.9	19.7	13.9	10.3	4.70	10.71	-
									Av. N50°W
Tsuru[TR], D=2.7									
75.0	6.2	5.3	4.3	6.8	4.3	2.0	2.40	3.65	N60°W
241.0	12.2	11.4	9.4	14.4	9.4	6.5	3.95	8.04	-
301.0	9.5	7.6	7.0	10.4	7.0	8.1	1.70	5.69	N55°W
389.0	16.0	13.9	14.9	26.9	14.9	10.5	8.20	14.81	N60°W
									Av. N60°W
Ashigawa[AS], D=2.6									
128.0	10.8	9.5	5.9	6.9	5.9	3.3	1.80	3.82	N40°W
133.0	10.5	9.6	5.6	5.9	5.6	3.5	1.20	3.37	-
140.0	13.3	10.6	6.7	8.1	6.7	3.6	2.25	4.45	-
147.0	11.5	7.4	6.9	11.8	6.9	3.8	4.00	6.33	-
159.0	11.6	10.3	7.3	10.0	7.3	4.1	2.95	5.46	-
162.0	16.8	9.5	8.6	14.7	8.6	4.2	5.25	7.83	N85°E
168.0	18.1	13.0	11.1	18.6	11.1	4.4	7.10	9.82	-
171.0	19.7	11.8	11.0	19.5	11.0	4.4	7.55	10.24	-
175.0	21.9	13.0	9.6	14.0	9.6	4.6	4.75	7.61	N50°W
182.0	20.8	11.2	9.8	16.4	9.8	4.7	5.85	8.73	-
189.0	15.6	9.6	8.0	12.5	8.0	4.9	3.80	6.81	-
193.0	21.6	12.9	8.9	11.9	8.9	5.0	3.45	6.52	N80°W
									Av. N60°W

Table 4.1 (b):

Depth (m)	Hydrofrac. data (MPa)			Stress(MPa)					Frac. azimuth
	Pb	Pr	Ps	SHmax	SHmin	Sv	SS	SN	
Enzan[EN], D=2.55(0-80m) & 2.75(80-200m)									
103.0	10.7	5.4	3.9	5.3	3.9	2.7	1.30	2.97	-
114.0	13.5	6.1	4.4	6.0	4.4	3.0	1.50	3.36	-
123.0	12.6	5.7	4.5	6.6	4.5	3.2	1.70	3.67	N55°W
154.0	14.7	5.5	5.3	8.9	5.3	4.1	2.40	4.96	N50°W
162.0	18.4	6.2	5.6	9.0	5.6	4.3	2.35	5.03	-
172.0	14.9	7.5	6.4	10.0	6.4	4.6	2.70	5.58	-
173.0	12.6	7.2	6.5	10.6	6.5	4.6	3.00	5.87	N55°W
182.0	15.2	6.8	5.4	7.6	5.4	4.8	1.40	4.38	N20°W
185.0	16.1	10.1	7.6	10.9	7.6	4.9	3.00	6.05	N45°W
								Av.	N50°W
Tanzawa[TZ], D=2.45									
91.0	7.9	4.6	4.5	8.0	4.5	2.2	2.90	4.20	N45°W
125.0	8.1	6.2	5.7	9.7	5.7	3.1	3.30	5.15	-
134.0	7.1	6.0	4.9	7.4	4.9	3.3	2.05	4.01	-
136.0	10.0	7.5	6.9	11.8	6.9	3.3	4.25	6.19	-
Nishiizu[NI], D=2.6									
263.0	22.2	12.5	11.1	18.2	11.1	6.8	5.70	9.87	N20°E
303.0	15.8	12.1	12.4	22.1	12.4	7.9	7.10	11.97	-
343.0	23.7	-	12.3	-	12.3	8.9	-	-	S40°W
409.0	14.8	14.1	13.0	20.8	13.0	10.6	5.10	11.61	-
423.0	19.6	16.7	14.6	22.9	14.6	11.0	5.95	12.72	-
436.0	17.3	13.9	13.1	21.0	13.1	11.3	4.85	11.79	N20°E
								Av.	N20°E
Shuzenji[SZ], D=2.2									
136.0	10.8	4.6	4.1	6.3	4.1	3.0	1.65	3.29	N25°E
329.0	31.5	9.8	8.1	11.2	8.1	7.2	2.00	5.91	N15°E
395.0	12.4	9.9	8.4	11.4	8.4	8.7	1.50	5.95	-
								Av.	N20°E
Shimoda[SM], D=2.2									
71.0	3.1	1.4	1.5	2.5	1.5	1.6	0.48	1.31	N25°W
216.0	11.8	7.1	5.3	6.6	5.3	4.8	0.90	3.54	-
253.0	15.9	8.1	6.9	10.1	6.9	5.6	2.25	5.32	-
390.0	19.8	10.2	8.1	10.2	8.1	8.6	1.05	5.25	-
416.0	23.0	-	9.5	-	9.5	9.2	-	-	-
422.0	19.6	9.0	9.4	15.0	9.4	9.3	2.85	7.93	N50°W
437.0	21.6	11.1	9.7	13.6	9.7	9.6	2.00	7.23	-
444.0	20.9	10.5	9.1	12.4	9.1	9.8	1.65	6.31	N35°W
								Av.	N35°W
Yokosuka[YK], D=2.1									
107.0	5.0	5.0	3.6	4.7	3.6	2.1	1.30	2.33	-
187.0	6.3	6.1	5.1	7.3	5.1	3.9	1.70	3.73	N 5°W
200.0	7.9	7.4	5.1	5.9	5.1	4.2	0.85	3.05	-
Chikura[CK], D=2.0(0-400m) & 2.1(400-800m)									
94.0	2.4	1.6	1.4	1.7	1.4	1.9	0.25	0.71	-
155.0	4.4	2.2	2.0	2.3	2.0	3.1	0.55	1.00	N40°W
264.0	7.4	4.1	3.7	4.4	3.7	5.3	0.80	1.86	N90°W
357.0	7.3	5.6	5.4	7.0	5.4	7.1	1.70	2.68	-
516.0	9.1	6.2	6.1	6.9	6.1	10.4	2.15	3.09	N25°W
623.0	10.0	8.1	7.7	8.8	7.7	12.8	2.55	4.02	N65°W
735.0	13.8	10.0	9.9	12.3	9.9	15.0	2.55	5.10	-
756.0	14.4	11.4	10.6	12.6	10.6	15.5	2.45	5.49	-
773.0	14.5	10.3	10.1	12.3	10.1	15.8	2.85	5.22	-
784.0	18.8	11.8	11.0	13.4	11.0	16.1	2.55	5.71	N50°W
								Av.	N45°W

Table 4.1 (c):

Depth (m)	Hydrofrac. data (MPa)			Stress(MPa)					Frac. azimuth
	Pb	Pr	Ps	SHmax	SHmin	Sv	SS	SN	
Futtsu[FT], D=2.0									
101.0	3.6	1.7	2.0	3.3	2.0	2.0	0.65	1.65	-
178.0	7.7	3.0	3.3	5.1	3.3	3.6	0.90	2.42	-
213.0	6.3	4.1	4.3	6.7	4.3	4.2	1.25	3.32	N55°W
254.0	5.7	4.3	4.8	7.6	4.8	5.1	1.40	3.66	-
279.0	19.7	6.8	6.0	8.4	6.0	5.6	1.40	4.21	N50°W
285.0	13.2	6.8	6.2	9.0	6.2	5.7	1.65	4.50	N40°W
308.0	16.6	5.6	6.2	9.9	6.2	6.2	1.85	4.97	-
335.0	12.8	8.3	7.3	10.3	7.3	6.7	1.80	5.15	-
418.0	8.9	7.1	8.3	13.6	8.3	8.4	2.65	6.77	-
437.0	19.0	7.5	8.5	13.6	8.5	8.7	2.55	6.68	-
									Av. N50°W
Tsukuba[TK], D=2.0(0-410m) & 2.5(410-600m)									
435.0	21.4	17.4	14.4	21.4	14.4	8.8	6.30	10.75	-
557.0	-	-	-	-	-	-	-	-	N45°W
599.0	26.3	22.0	18.5	27.5	18.5	13.0	7.25	14.26	-
Ishige[IS], D=2.0(0-518m) & 2.5(518-900m)									
438.0	7.7	6.5	5.8	6.5	5.8	8.6	1.40	2.82	N30°W
555.0	21.0	14.6	14.4	23.1	14.4	11.1	6.00	11.55	N20°W
573.0	22.3	16.1	14.9	22.9	14.9	11.5	5.70	11.47	N10°E
586.0	20.9	18.1	15.9	23.7	15.9	11.8	5.95	11.89	N 5°E
606.0	19.9	17.1	16.8	27.2	16.8	12.3	7.45	13.69	-
744.0	40.6	29.9	30.9	55.4	30.9	15.7	19.85	28.11	N80°W
784.0	44.5	26.3	25.8	43.3	25.8	16.7	13.30	22.17	N40°W
826.0	33.9	28.3	30.3	54.3	30.3	17.7	18.30	27.74	-
844.0	35.4	33.6	30.9	50.7	30.9	18.1	16.30	25.96	N20°W
847.0	31.3	27.5	28.5	49.5	28.5	18.2	15.60	25.32	-
868.0	40.4	27.7	26.7	43.7	26.7	18.7	12.50	22.52	-
873.0	30.2	27.2	27.7	47.2	27.7	18.8	14.20	24.27	-
									AV. N25°W
Nakaminato[NA], D=2.3									
217.0	6.6	6.6	6.4	10.4	6.4	5.0	2.70	5.53	N45°E
245.0	9.6	7.2	6.7	10.5	6.7	5.6	2.45	5.60	-
248.0	9.9	7.7	6.7	9.9	6.7	5.7	2.10	5.32	-
275.0	14.0	7.6	7.5	12.1	7.5	6.3	2.90	6.45	N65°E
326.0	11.4	9.6	8.8	13.5	8.8	7.5	3.00	7.24	-
347.0	18.0	11.0	9.8	14.9	9.8	8.0	3.45	7.98	N50°E
351.0	20.4	9.5	9.3	14.9	9.3	8.1	3.40	7.99	S50°W
383.0	21.1	11.6	11.4	18.8	11.4	8.8	5.00	9.98	-
434.0	14.1	9.3	10.5	17.9	10.5	10.0	3.95	9.61	-
									Av. N50°E
Hasaki[HS], D=1.9(0-650m) & 2.1(650-800m)									
519.0	9.1	7.2	7.2	9.2	7.2	9.9	1.35	3.36	N25°W
521.0	9.1	7.8	7.4	9.2	7.4	9.9	1.25	3.44	-
630.0	11.3	10.1	9.7	12.7	9.7	12.1	1.50	4.90	-
648.0	17.5	11.6	10.9	14.6	10.9	12.5	1.85	6.27	N20°W
680.0	18.0	11.6	10.5	13.0	10.5	13.1	1.30	5.00	N25°W
702.0	18.9	11.5	11.0	14.5	11.0	13.5	1.75	5.73	-
778.0	25.8	14.4	14.1	20.1	14.1	15.1	3.00	9.32	N45°W
792.0	22.2	15.5	14.7	20.7	14.7	15.3	3.00	9.78	-
									Av. N30°W

Table 4.1 (d):

Depth (m)	Hydrofrac. data (MPa)			Stress(MPa)					Frac. azimuth
	Pb	Pr	Ps	SHmax	SHmin	Sv	SS	SN	
Choshi[CH], D=2.2									
60.0	4.0	4.0	2.6	3.2	2.6	1.3	0.95	1.65	-
97.0	4.0	3.5	3.3	5.4	3.3	2.1	1.65	2.78	N85°E
123.0	5.7	4.4	3.8	5.8	3.8	2.8	1.50	3.07	-
165.0	5.6	5.6	4.4	6.0	4.4	3.6	1.20	3.15	-
202.0	7.4	7.4	6.4	9.8	6.4	4.4	2.70	5.08	-
391.0	10.7	10.7	9.2	13.0	9.2	8.6	2.20	6.89	-
Hannou[HN], D=2.5									
58.0	3.4	3.2	3.2	5.8	3.2	1.4	2.20	3.02	-
110.0	10.6	7.0	4.8	6.3	4.8	2.7	1.80	3.40	N30°E
172.0	11.8	6.5	7.6	14.6	7.6	4.2	5.20	7.68	N45°E
186.0	14.7	9.9	9.7	17.3	9.7	4.6	6.35	9.09	N60°E
247.0	11.2	9.3	9.4	16.4	9.4	6.1	5.15	8.78	-
280.0	11.5	9.8	8.8	13.8	8.8	6.9	3.45	7.55	N20°E
516.0	24.2	22.2	19.7	31.7	19.7	12.6	9.55	16.99	-
538.0	25.4	15.9	15.9	26.4	15.9	13.2	6.60	14.42	-
598.0	45.8	22.0	21.0	35.0	21.0	14.7	10.15	18.87	-
601.0	21.3	21.0	20.5	34.5	20.5	14.7	9.90	18.59	-
603.0	22.7	17.0	18.0	31.0	18.0	14.8	8.10	16.87	-
758.0	47.0	20.8	19.5	30.1	19.5	18.6	5.75	16.78	-
761.0	35.5	20.4	19.6	30.8	19.6	18.6	6.10	17.10	-
									Av. N40°E
Awano[AW], D=2.45									
51.0	3.0	2.7	2.3	3.7	2.3	1.2	1.25	1.94	-
144.0	6.5	5.5	4.9	7.8	4.9	3.5	2.15	4.21	N70°W
163.0	7.2	5.9	4.1	4.8	4.1	4.0	0.40	2.77	N60°W
278.0	9.4	8.2	7.5	11.5	7.5	6.8	2.35	6.37	-
377.0	12.1	9.8	9.1	13.7	9.1	9.2	2.25	7.68	-
535.0	16.4	16.2	14.8	22.9	14.8	13.1	4.90	12.65	-
595.0	22.4	22.0	19.4	30.2	19.4	14.6	7.80	16.45	-
655.0	21.2	20.9	20.7	34.7	20.7	16.0	9.35	18.80	-
711.0	27.1	23.5	22.0	35.4	22.0	17.4	9.00	19.29	-
721.0	25.2	22.9	21.6	34.7	21.6	17.7	8.50	18.99	N60°W
750.0	23.6	23.9	22.9	37.3	22.9	18.4	9.45	20.36	-
764.0	29.0	28.0	23.0	33.4	23.0	18.7	7.35	18.41	-
773.0	29.6	28.7	26.1	41.9	26.1	18.9	11.50	22.68	-
									Av. N60°W

Pb:initial breakdown, Pr:reopening, and Ps:instantaneous shut-in pressures.
SHmax:horizontal maximum, SHmin:horizontal minimum, and Sv:vertical stresses.
SS:shear stress, and SN:effective normal stresses.
D:Density. Av.:Average azimuth of fractures.

4.2 Vertical distribution of stress magnitude

Stresses for each site are plotted against the depths in Fig. 4.5. The results of three sites, [EN], [TZ] and [AS], are explained in detail in Section 5.2 and shown in Fig. 5.6. Open and black circles indicate S_{Hmax} and S_{Hmin}, respectively. The best fit obtained by the least squares method is denoted by a solid line. Chain lines indicate S_V. The coefficients of these approximate stress-depth relationship lines are shown in Table 4.2, where the unit of stress is MPa and the depth is in meters. It can be seen from these figures that both stresses, S_{Hmax} and S_{Hmin}, increase with depth. However, the absolute stress values are quite different from site to site. Some other characteristics of the stress magnitude distribution can be observed.

Relative magnitude relationship of stresses:

The stress state denoted by the normal fault type, $S_V > S_{Hmax} > S_{Hmin}$, throughout the measurement depth occurred only in the [CK] well. In the case of the [NI] well, the stress state near the surface is the reverse fault type, $S_{Hmax} > S_{Hmin} > S_V$, and that of a deeper area is suggested to become the normal fault type. In contrast with this, as in the [HS] and [IS] cases the stress state is of the normal type near the surface and that of the deeper area is the reverse. In the cases of the [SZ], [SM], [HM], and [FT] wells, the stress state of a strike-slip fault type, $S_{Hmax} > S_V > S_{Hmin}$, seems to appear at the deeper areas. However, it is not obvious because of a slight difference between S_{Hmin} and S_V.

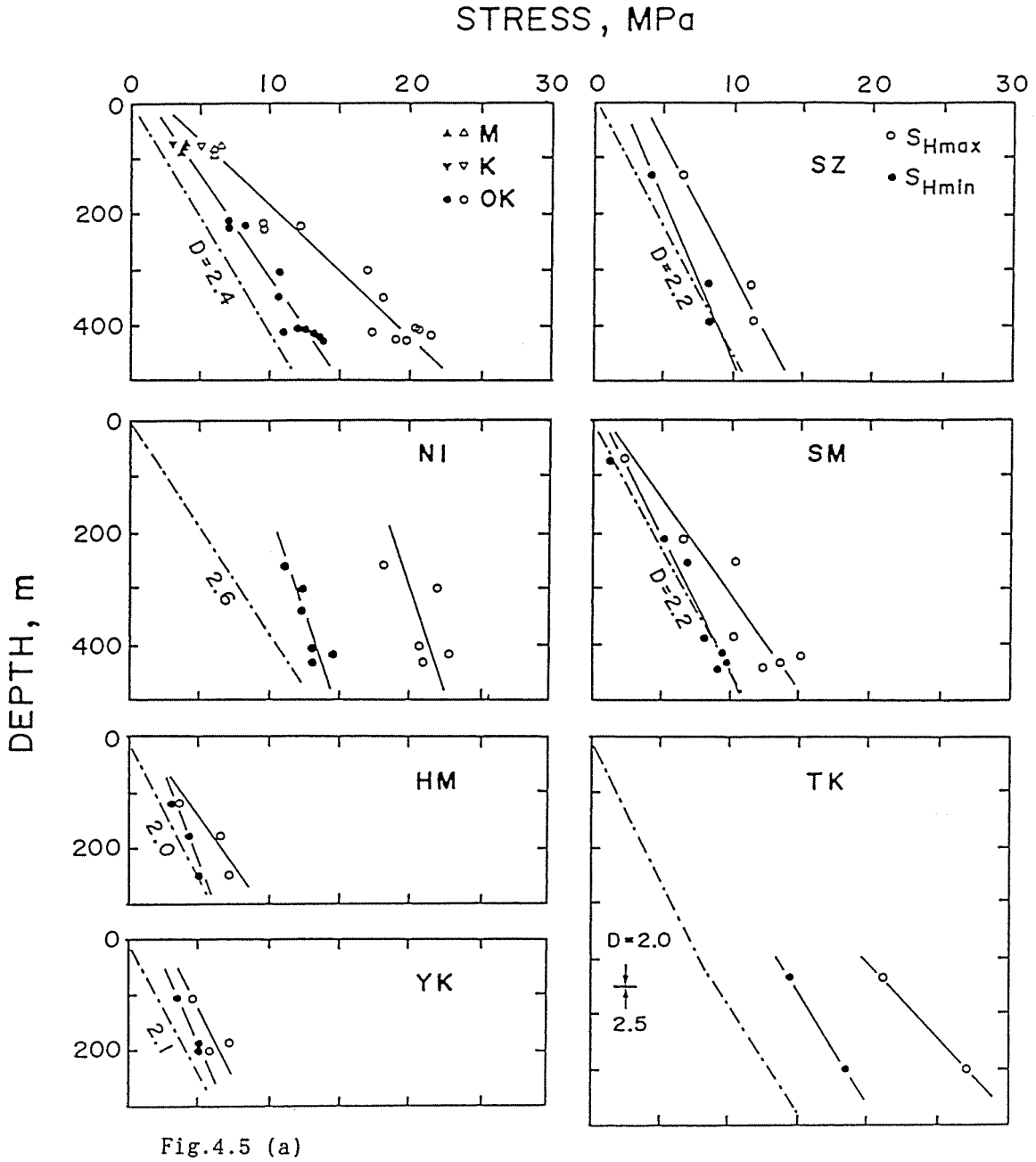

Fig.4.5 (a)

Fig.4.5: Plots of the stresses as a function of depth. Site names correspond to those in Table 4.1. Open and black circles indicate the maximum and minimum horizontal compressive stresses, respectively. Solid lines indicate the best fit obtained by the least squares method. Chain lines give the lithostatic pressure, which is calculated from the density log data and/or core sample density.

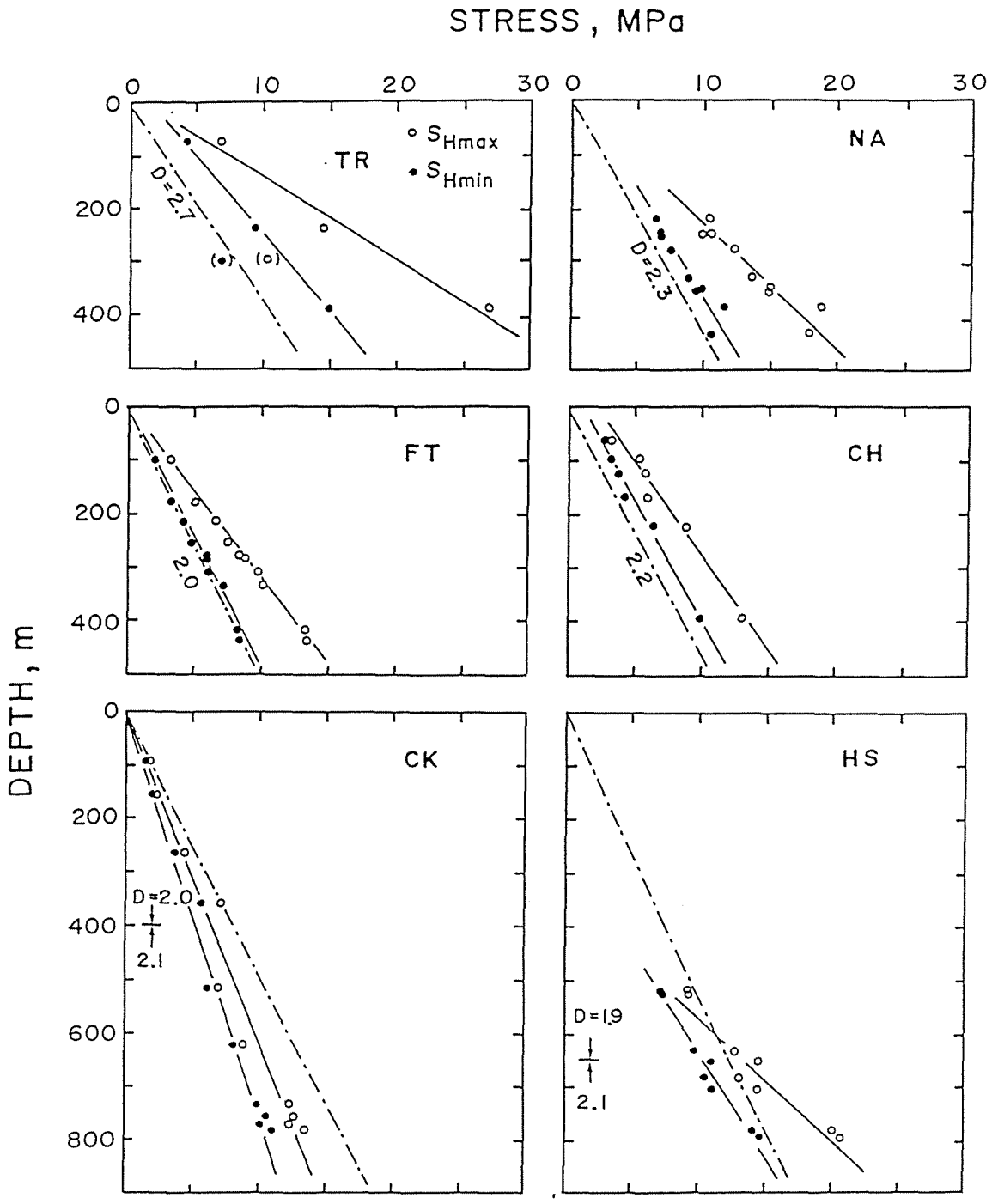
STRESS, MPa
DEPTH, m
TR
NA
FT
CH
CK
HS
S_{Hmax}
S_{Hmin}
D=2.7
D=2.3
2.0
2.2
D=2.0
2.1
D=1.9
2.1

Fig.4.5 (b)

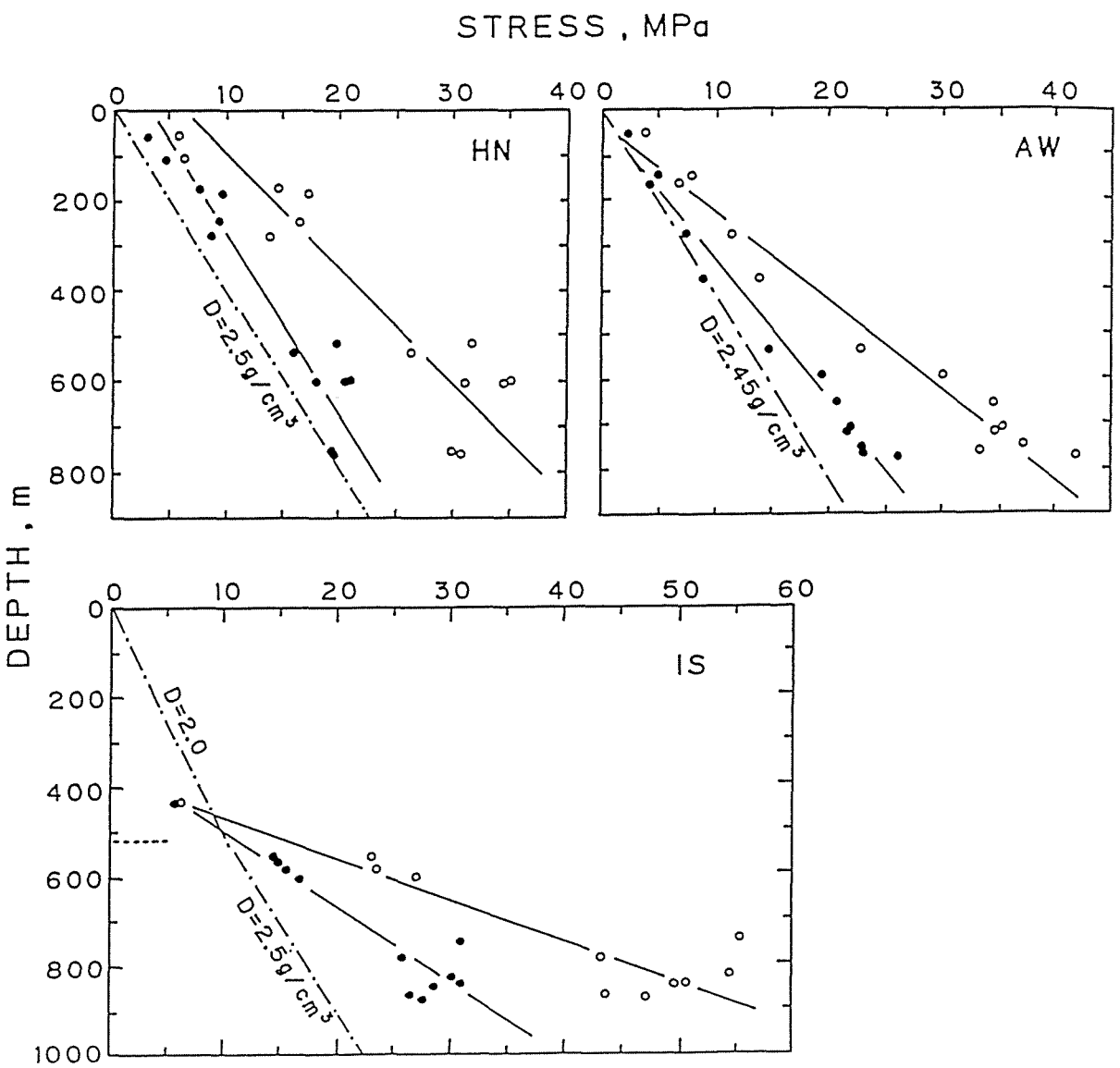

Fig.4.5 (c)

Stress magnitude gradient with depth:

The stress magnitude increases with depth by different gradients from that of the lithostatic pressure, and the gradient differs from site to site. The gradient of each stress, S_{Hmax}, S_{Hmin}, and S_V, is represented by the coefficient a, c, and e, respectively, in Table 4.2. The relation of c<e<a is frequently seen in many sites. However, the [OK], [TR] and [HS] sites show a relation where e<c; whereas the [NI], [SZ] and [CK] sites show a relation where e>a. With regards to each site, several sites show a linear increase of the stresses with depth. In other sites, the stresses at any depth are extremely larger (or lower) than adjacent areas. In general, the data obtained in large density rocks, in other words in hard rocks, show that the stresses tend to fluctuate largely. In contrast with this fact, in soft rocks both S_{Hmax} and S_{Hmin} increase linearly with depth by only a small fluctuation. The tendency of the S_S variation is about the same.

Table 4.2: COEFFICIENTS OF APPROXIMATE STRESS-DEPTH LINES

Site	SHmax=ah+b		SHmin=ch+d		Sv=eh	
	a/100	b	c/100	d	e/100	
HM	2.7	1.0	1.5	1.6	2.00	
M,K,OK	4.3	2.1	2.8	1.4	2.40	
TR	6.4	1.1	3.4	1.6	2.70	
AS	13.3	-9.0	6.2	-1.8	2.60	
EN	7.2	-2.2	4.9	-1.7	2.55	(0-80m)
					2.75	(80-200m)
TZ	4.1	4.3	3.4	1.4	2.45	
NI	1.3	16.2	1.4	7.8	2.60	
SZ	2.1	3.6	1.8	1.8	2.20	
SM	2.9	0.9	2.0	0.7	2.20	
YK	2.0	2.7	1.7	1.8	2.10	
CK	1.6	0.0	1.3	0.1	2.00	(0-400m)
					2.10	(400-800m)
FT	3.1	0.3	2.1	0.1	2.00	
TK	3.7	5.2	2.5	3.5	2.00	(0-400m)
					2.50	(400-600m)
IS	9.7	-31.9	5.2	-14.9	2.00	(0-518m)
					2.50	(518-900m)
NA	4.3	0.1	2.4	10.4	2.30	
HS	4.4	-15.2	2.6	-6.4	1.90	(0-650m)
					2.10	(650-800m)
CH	2.9	2.1	2.2	1.1	2.20	
HN	3.9	6.2	2.5	3.3	2.50	
AW	5.1	-1.7	3.2	-0.7	2.45	

SHmax, SHmin, & Sv= MPa; h= m.

Vertical distribution summarized by all stress data:

An average horizontal stress magnitude, $S_{Hav}=(S_{Hmax}+S_{Hmin})/2$, is plotted versus the depth in Fig. 4.6 for all measured data. This figure outlines the average stress state to the depth of 1,000 m in the Kanto-Tokai area. One of the characteristic tendencies of the vertical distribution of the stress magnitude is a convergence at or near the surface with fluctuation at the deeper areas. The principle stresses and the average horizontal stress calculated by the least squares method are:

$$S_{Hmax}=0.043h-0.65$$

$$S_{Hmin}=0.026h+0.74$$

$$S_{Hav}=0.035h+0.1$$

$$S_{v}=0.023h$$

where the unit of stresses is MPa and the depth is in meters. Accumulated data also indicate that the reverse fault type stress state is excellent in the Kanto-Tokai area.

Fig. 4.7 shows the gradient with the depth of the average horizontal stress for each site. The average horizontal stress of all sites, $S_{Hav}=0.035h+0.1$, elucidates the characteristics concerning the absolute stress value. Two groups divided by this line of the average horizontal stress have both characteristics. The higher stress site, which belongs to the group above this line, has a relatively higher density of rocks. Here the critical density of rocks is 2.3 g/cm^3. This feature suggests that the difference of rock hardness influences the vertical distribution of the stress magnitude.

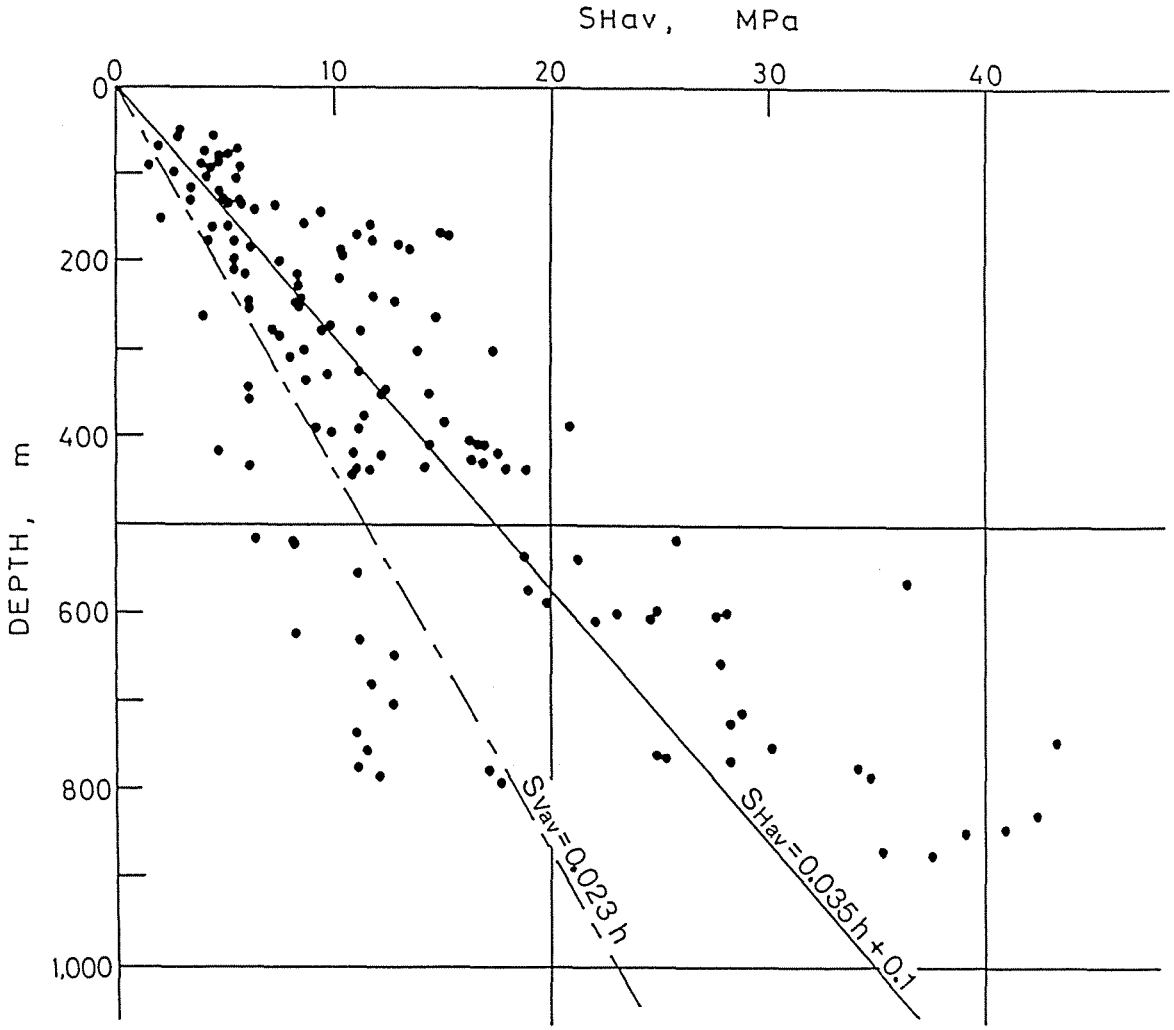

Fig.4.6: Mean horizontal stress, average of the horizontal maximum and minimum stresses, distribution with depth for all measured data. S_{Hav} shown by the solid line is obtained by the least squares method. The average of the vertical stresses, S_{vav}, is drawn as a reference.

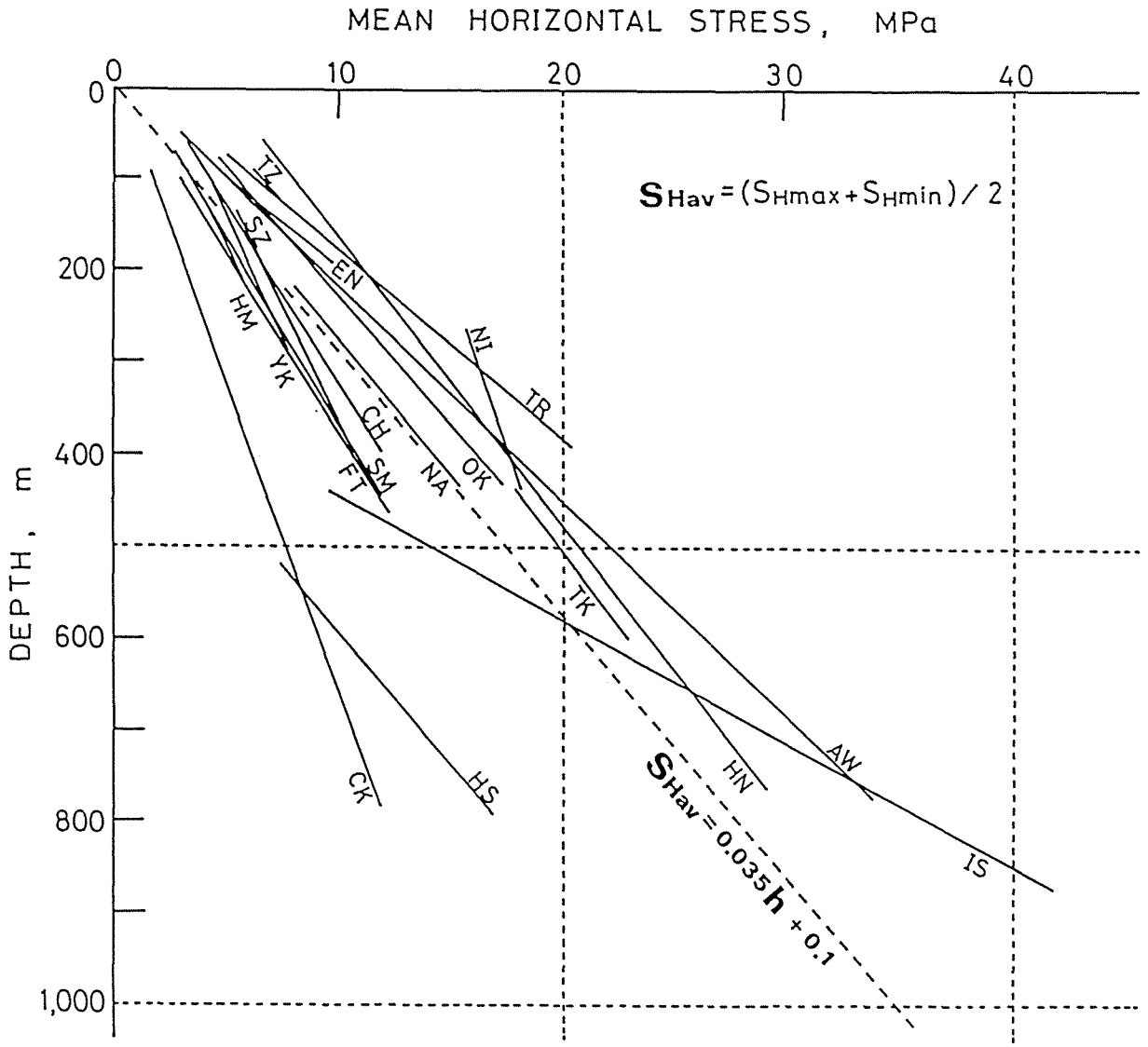

Fig.4.7: Average gradient of the mean horizontal stress for each site.

4.3 Orientation of maximum horizontal compressive stress

The azimuth of the hydrofractures, which indicates the orientation of S_{Hmax}, is shown in Table 4.1. The measurement depths where the hydrofractures are detected by the BHTV are 95 m in [K]; 263 m, 343 m and 436 m in [NI]; 254 m in [FT]; 438 m in [IS]; 217 m in [NA]; and 123 m in [EN]. All the others are detected by the impression packer. Since the BHTV uses an ultrasonic reflection, the hard rocks which strongly reflect the ultrasonic wave have an advantage over the soft rocks. However, when a newly created fracture closes completely after releasing the water pressure, the percentage of success is low. On the contrary, the impression packer can force a closed hydrofracture to reopen by being impressed to the borehole wall by a pressure a little greater than the reopening pressure. The percentage of success of the impression packer is more than 80 percent.

As seen in Figs. 4.2 and 4.3, each fracture has an irregular shape which leads to errors in the estimation of the mean fracture azimuth. Also, the mean fracture azimuth fluctuates with depth in the same borehole. However, the depth distribution of the S_{Hmax} orientation at any site does not vary systematically with depth. The scattering appears to be mostly due to the inhomogeneous nature of the rocks. The average S_{Hmax} direction of each measurement site is indicated on the map shown in Fig. 4.8. The stress orientation in this area is believed to be complicated since this area is a junction of the three plates, as mentioned above. The orientations obtained are scattered from site to site as expected. This phenomena will be discussed below in Section 7.1.

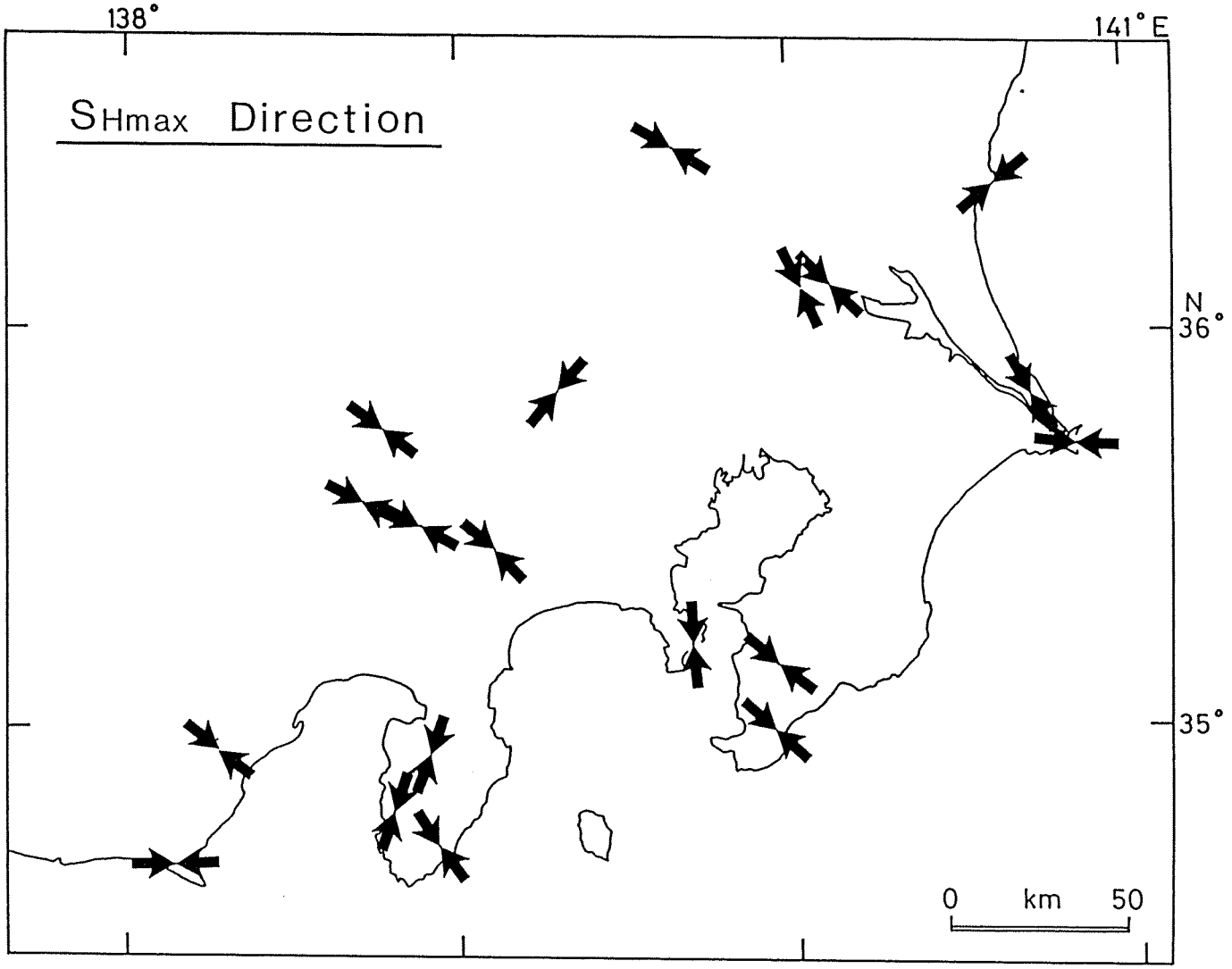

Fig.4.8: Maximum horizontal stress direction measured by hydraulic fracturing for each site.

CHAPTER 5:

PHYSICAL MECHANISM CONTROLLING VERTICAL DISTRIBUTION OF STRESSES

In order to better understand the stress magnitude depth distributions, in situ data measured at each site have been accumulated. It is still difficult to estimate the stress state at the deeper areas or around the sites from the data collected. This is because a specific theory or general rule to explain quantitatively the stress distributions has not been proposed yet. If a physical mechanism controlling the stress state in the basement is revealed, it might be possible to apply this mechanism to the estimation.

Horizontal stresses increase with different gradients from that of the overburden pressure, and the gradients vary in each site as shown in Figs. 4.5 and 4.7. From the stance of the rock material properties, the depth distribution of stresses in a relatively soft rock basement have a tendency to have only slight variations in comparison with that of those in a hard rock basement.

In this section, the main physical mechanism controlling the stress state in a shallow crust is studied by considering the characteristics of the two different rock types, soft and hard. First, the stress gradient in the soft rocks, of whose properties seem to be easily understood, is examined. Then this study is developed and applied to hard rocks. Here, the rock density D is used as an index of the hardness of rocks. D=2.4 g/cm^3 is taken as the dividing value between hard and soft rocks. This is because the stresses obtained in rocks smaller than D=2.4 g/cm^3 tend to increase linearly with depth (TSUKAHARA and IKEDA, 1989a). The locations of the measurement sites discussed below are shown in Fig. 5.1. Open circles

indicate the sites with soft rocks and black circles indicate those with hard rocks.

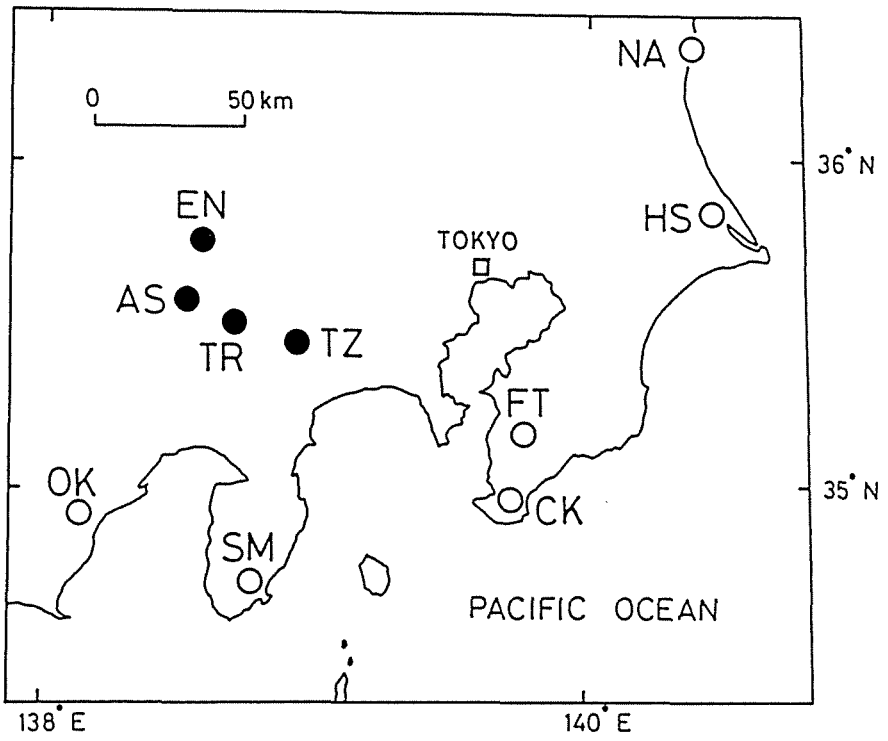

Fig.5.1: Stress measurement sites located in soft (open circles) and hard (closed circles) rocks.

5.1 Frictional sliding in soft rocks

TSUKAHARA and IKEDA (1989a) explained the stress depth distribution in the soft rocks by a "yield stress model". That is, the stress level in the soft rocks is maintained by a successive occurrence of frictional sliding, and the stress is considered to be a critical value for sliding at any depth. Therefore, the stress profiles in the soft rocks are characterized by the yielding which is controlled by the frictional sliding of the micro-fractures. Since the yielding stress increases with depth, the shear stress also increases linearly with depth.

The data used for this study fulfill the following conditions: 1) the data was taken from a depth deeper than 100 m to avoid topographically influenced data, 2) the data was taken from basements where the rock density was smaller than 2.4 g/cm^3, as mentioned above, and 3) the data was taken from sites which included more than five pairs of horizontal stresses in the same borehole. There are 6 measurement sites, [HS], [CK], [NA], [FT], [OK] and [SM], which satisfy these conditions. All these sites are comprised of sedimentary rocks dating from Cretaceous to Pliocene. Their stress depth distributions are shown in Fig. 4.5.

It is obvious that the main physical mechanism controlling the stress distribution is reflected in the maximum differential stress, that is the maximum shear stress, S_S. For example, the S_S distribution with the depths obtained from three sites, [NA], [FT] and [CK], are shown in Fig. 5.2 in comparison with the principal stress distribution. Solid lines in Fig. 5.2 indicate the best fit by the least squares method. The S_S increases almost linearly with depth. To explain this S_S depth distribution, a relationship between S_S and the effective normal stress S_N, which is calculated from the measured stress magnitudes, is examined. Fig. 5.3 shows S_S versus S_N for each site. Solid lines in Fig. 5.3 are drawn by connecting the point of the maximum ratio S_S/S_N with the origin. Two distinct characteristics are found in this figure: 1) The gradients of the solid lines are from 0.35 to 0.71. These values are consistent with the frictional coefficients (μ) of the rocks: μ=0.25~0.7, which are obtained by laboratory experiments (e.g. BYERLEE, 1978). 2) The data are distributed around the solid line. These are the characteristics of the "yield stress model", itself. However, the data are not plotted just on the solid line. The main reason for this

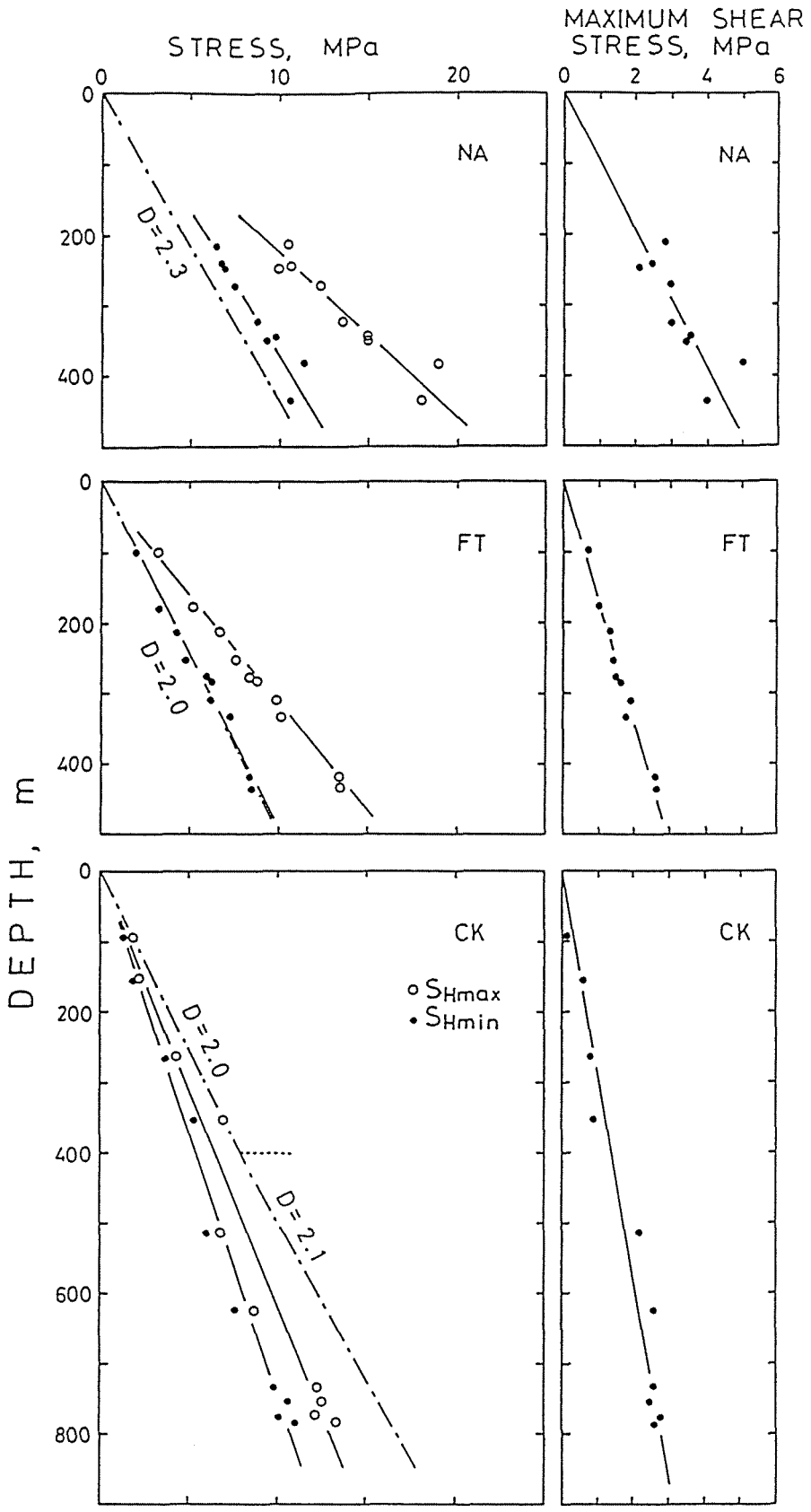

Fig.5.2: Examples of in situ stress and maximum shear stress profiles of the soft rock sites. Solid lines are all obtained by the least squares method.

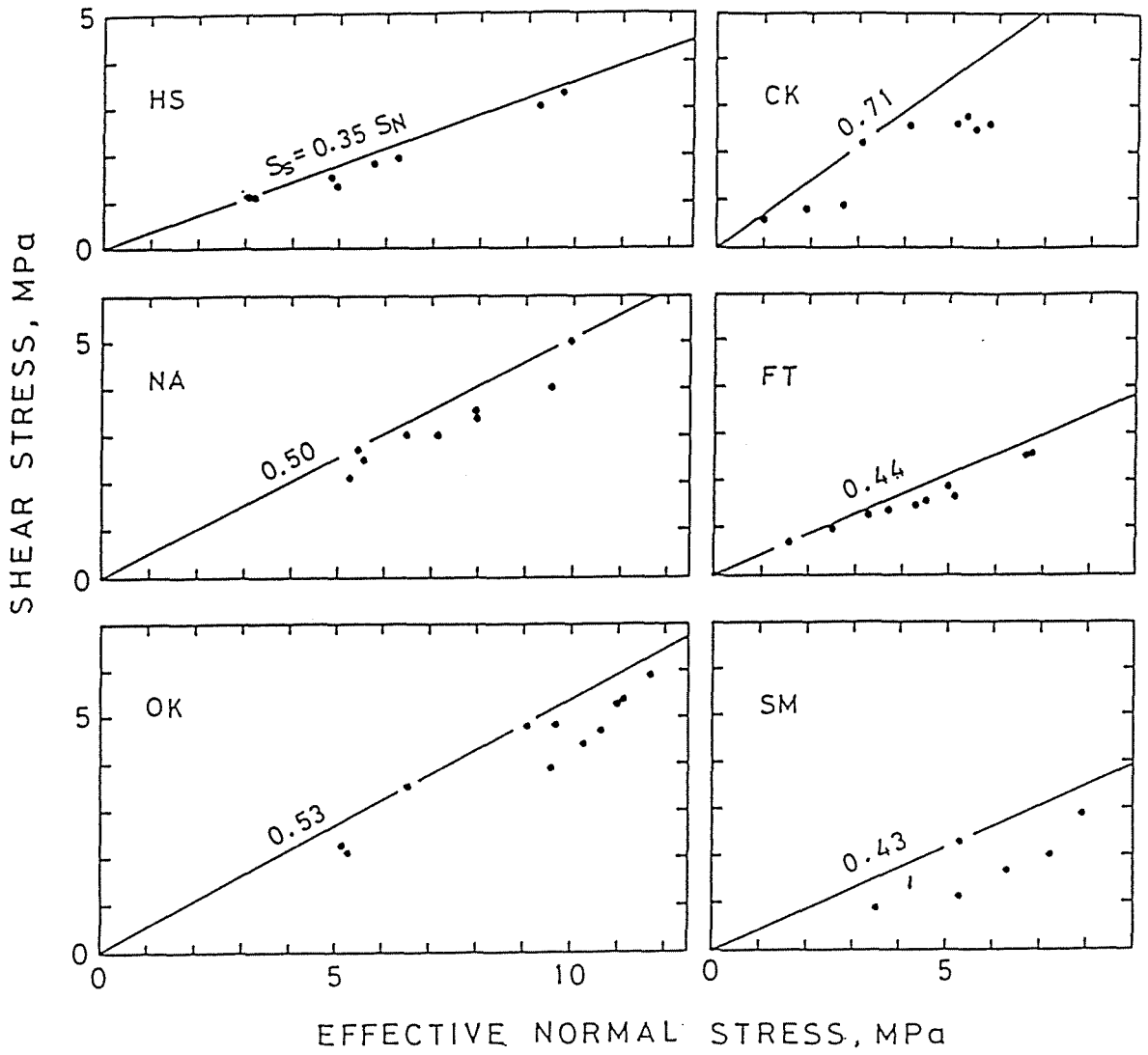

Fig.5.3: In situ shear stress measured in soft rocks plotted as a function of effective normal stress. Solid lines indicate the maximum ratio S_S/S_N for each measurement site with each frictional coefficient.

feature appears to depend on the heterogeneity of the rocks of each site. For example, the rocks of the [FT] well are more homogeneous than the other sites, so the plotted data are not very scattered due to a slight variation of the μ value. The μ value difference among the sites is represented as the difference of the gradient of the solid lines in Fig. 5.3.

Fig. 5.4 is drawn schematically as the "yield stress model". The straight line $S_S=\mu S_N$ indicates the critical state of stress for yielding. A stable stress state is in the area of $S_S<\mu S_N$, because frictional sliding will occur in the area over the line. Micro-fractures are countless in rocks. When the shear stress is added over the frictional strength of rocks, frictional sliding of the micro-fractures will occur, and the shear stress will decrease. It is also known that in proportion to the normal stress increase with depth, the shear stress also increases with depth.

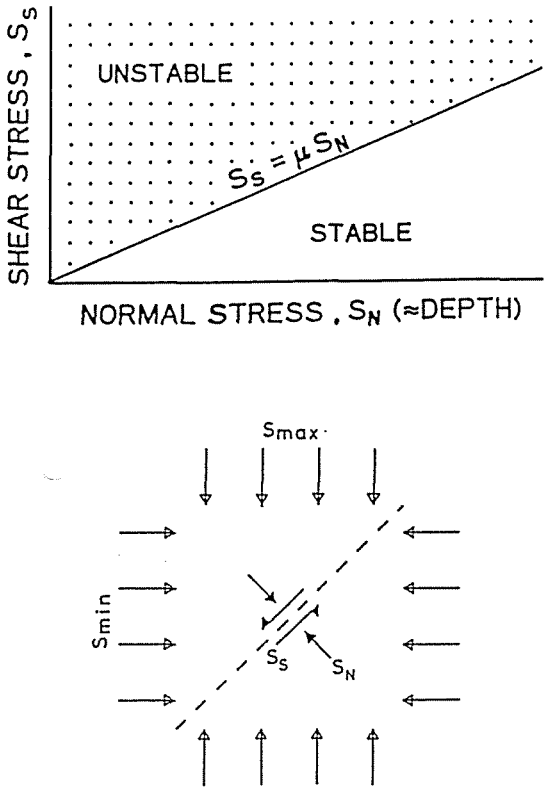

Fig.5.4: Schematic diagram of "Yield Stress Model".

5.2 Frictional sliding in hard rocks

The deeper areas of the crust consist of hard rocks. To reveal the stress state in these areas, it is necessary to understand the physical mechanism controlling the stress depth distribution in the hard rocks. Exposures of the hard rocks in the Kanto-Tokai area are seen in a narrow region such as the mountainous area in the Kanto area and Mt. Tsukuba. Therefore, the data obtained in the hard rocks in the shallower crust are important. In situ stress measurements by hydraulic fracturing were conducted at four sites, [EN], [TZ], [AS] and [TR], located in the hard rocks around the Kofu basin and near Mt. Tanzawa as shown in Fig. 3.1. The resulting data were found to be both regionally and vertically dense. This makes it possible to compare the stress distributions between the hard and soft rocks. Three of the sites, [EN], [TZ], and [AS], contained granitic rocks, and the [TR] well is located in an andesitic tuff area. Therefore, the stress distribution in the hard rocks is discussed by comparing the former three sites' results.

Fig. 5.5 shows the lithological columns and borehole logging data of the three sites. The lithology of the [EN] well is divided into two formations. Granodiolites are present beneath river sedimentary sand and gravel beds which total about 50 meters thick. The granodiolites are grayish white, crystalline and medium- to coarse textured. Stress magnitudes were obtained at 9 points below the depth of 100 m. At the [TZ] well, granodiolites are found about 8 m below the surface of the sand and gravel beds. The [TZ] well proved to be not good for the stress measurement because many natural fractures were observed on the borehole wall by the BHTV log.

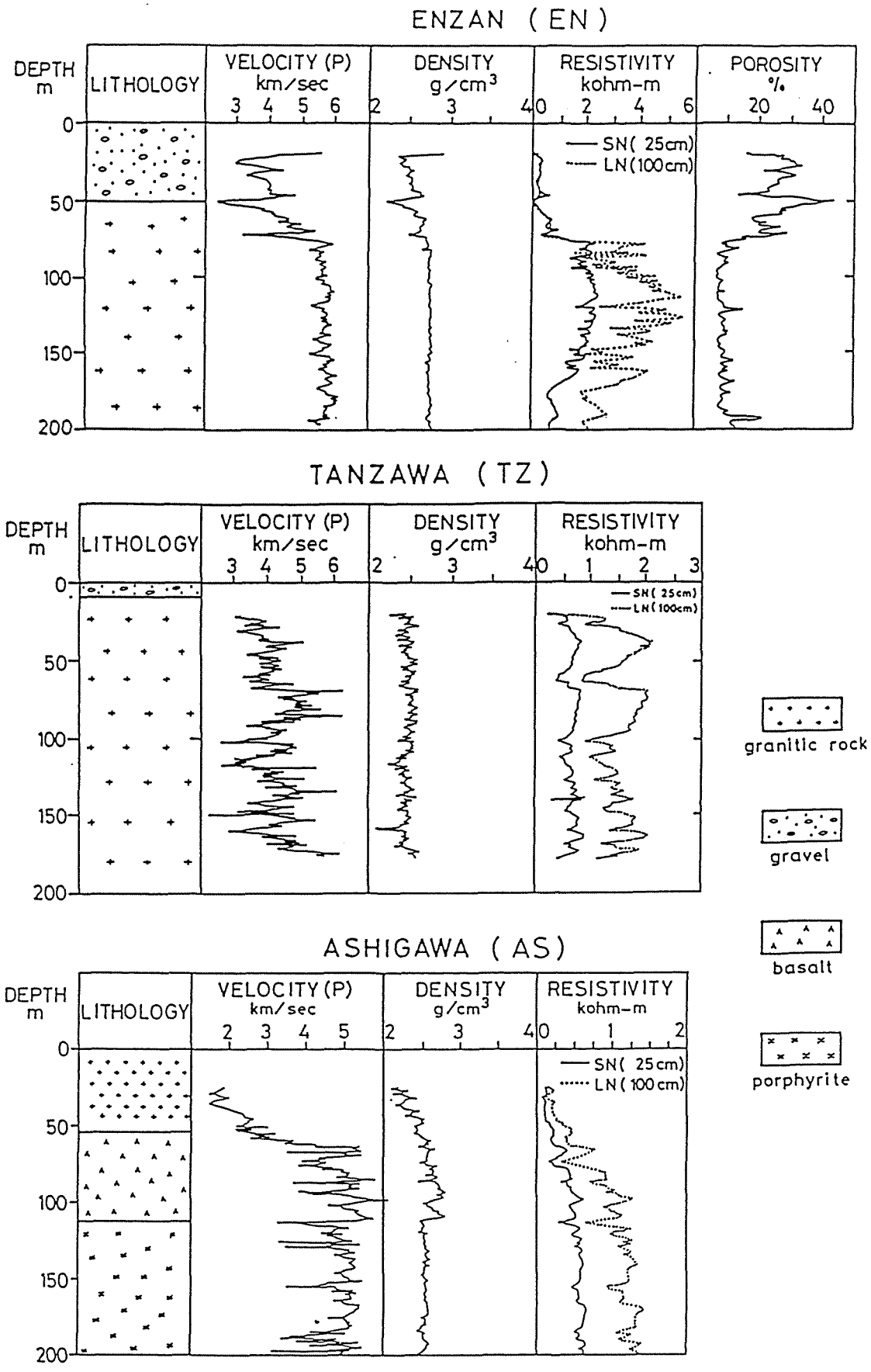

Fig.5.5: Lithological and geophysical logs in the hard rock boreholes.

The stress magnitudes were obtained at 4 points between the depths of 90 m and 136 m. The lithology of the [AS] well is divided into three formations: diolites (0~61.5 m), basaltic lavas (61.5~113.3 m) and porphyrites (113.3~203 m). The basalts have a larger density but are more fractured than the porphyrite. Stress magnitudes from this well were obtained at 12 points below 120 m.

Fig. 5.6 shows the stress depth distribution obtained from the three sites. While the distributions of both the horizontal- and shear stresses at the [AS] and [TZ] wells fluctuate largely, those of the [EN] well increase with the depth with little or no fluctuation. In particular, the [AS] well shows a characteristic feature, that is a stress concentration zone of about a 30 m interval around the depth of 170 m exists. The difference of these features is of particular importance in considering the mechanism of the stress distribution. By comparing the lithologies and logging data between three sites in Fig. 5.5, it is evident that the basement of the [EN] site is homogeneous and stable, as seen on the average value below the depth of 80 m where the P-wave velocity Vp (sonic log), the density D (gamma-ray log), and the porosity ϕ (neutron log), is 5.7 km/sec, 2.75 g/cm^3, and 10 %, respectively. On the other hand, in both the [TZ] and [AS] sites the Vp fluctuates greatly in the range of 2.5~6 km/sec at the [TZ] site and 3~6 km/sec at the [AS] site, in spite of a nearly constant density 2.4~2.5 g/cm^3 at the [TZ] site and 2.6 g/cm^3 at the [AS] site. In the hard rocks, there is a large gap in the material properties between the fractured parts and non-fractured parts. This appears to affect the stress distribution in the hard rocks as there is a greater fluctuation than in the soft rocks. It is also suggested that the stress distribution in the hard rocks, as in the case of a homogeneous

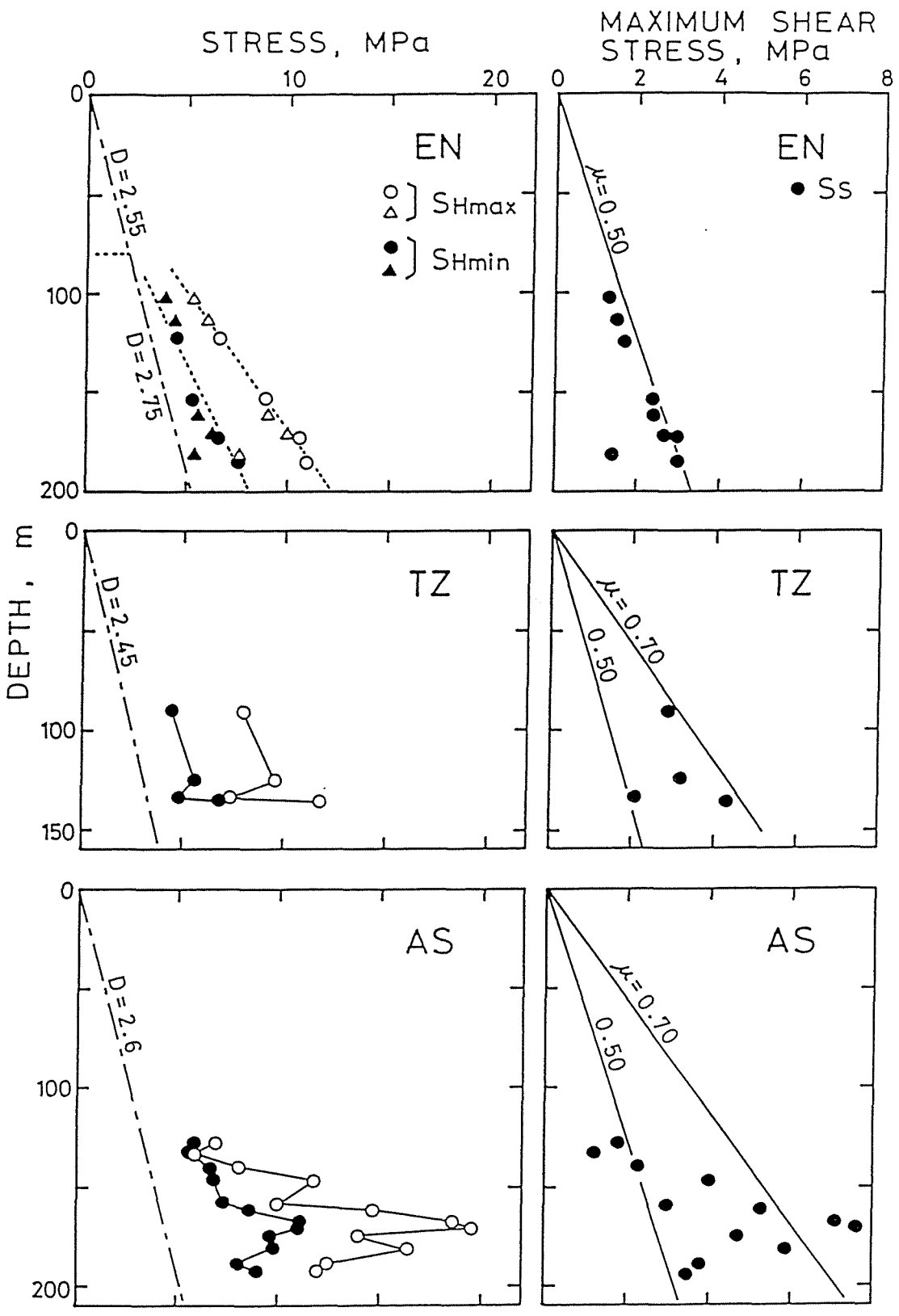

Fig.5.6: In situ stress and maximum shear stress profiles of hard rock sites. Solid lines in the shear stress-depth relation are drawn by calculating with the frictional coefficients, 0.5 and 0.7.

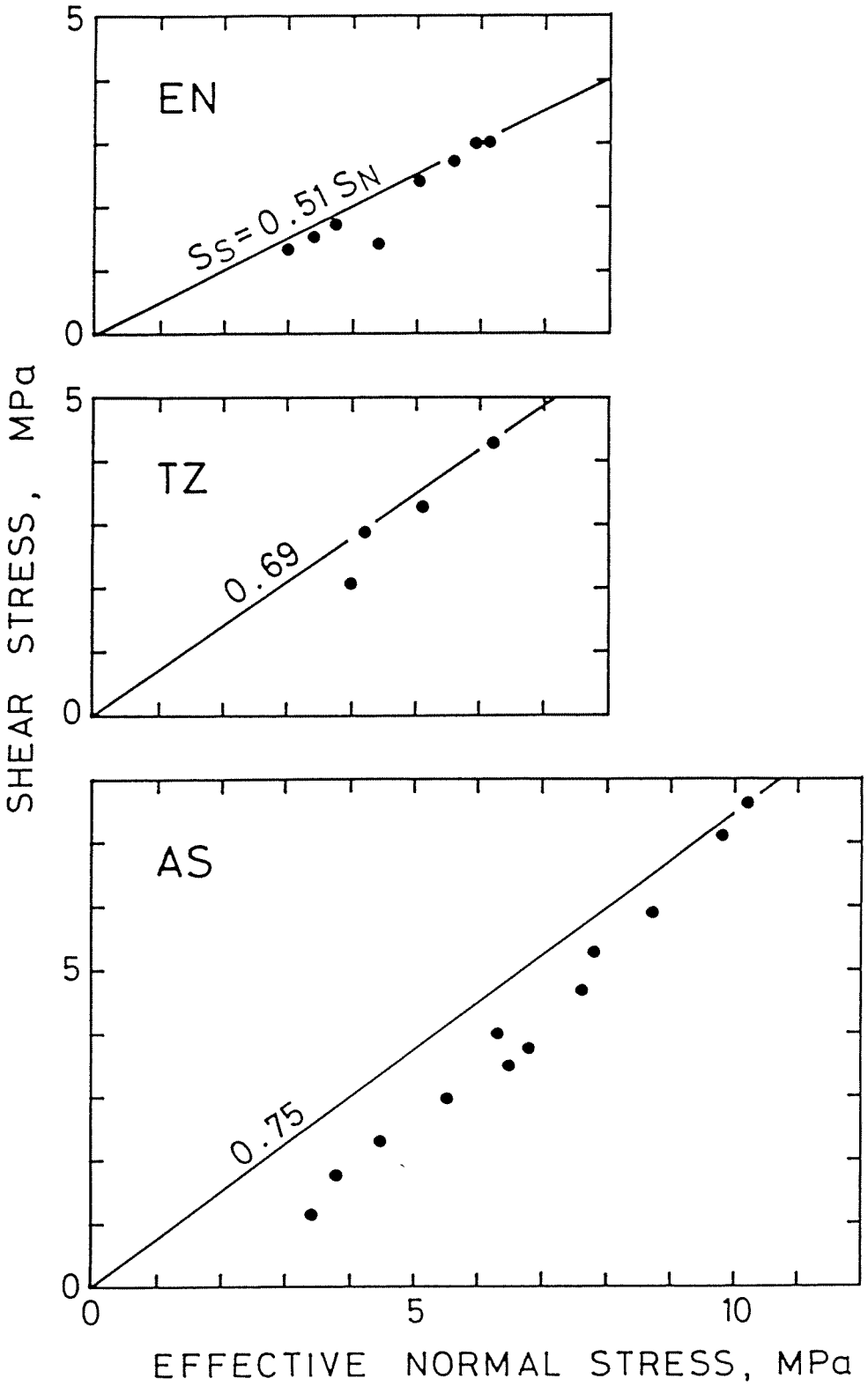

Fig.5.7: In situ shear stress measured in hard rocks plotted as a function of effective normal stress. Solid lines indicate the maximum ratio S_S/S_N for each measurement site with each frictional coefficient.

basement which contains few natural fractures or faults like the [EN] well, is as monotonous as in the soft rocks.

Fig. 5.7 shows the relation between S_S versus S_N of the three sites. Solid lines indicate the maximum ratio S_S/S_N for each measurement site in the same way as that of Fig. 5.3. The same tendency as in the case of the soft rocks is present, that is the data concentrate around the line $S_S=\mu S_N$. The frictional coefficient μ differs among the three sites: it ranges from 0.51 at the [EN] well to 0.75 at the [AS] well. The shear stress depth distribution is considered in terms of the μ value. The measured horizontal stresses are all larger than the vertical stresses. Therefore, under the condition of $S_V=Dgh=S_{min}$, the maximum shear stress which can maintain this vertical stress as the minimum compressive principal stress, can be calculated by using the μ value:

$$S_S=\mu S_N=\mu\left[(S_{max}+S_{min})/2-P_p\right]$$

$$=\mu(S_S+S_{min}-P_p)$$

$$=\mu gh(D-1)/(1-\mu) \qquad (15)$$

where P_p is assumed to be the hydrostatic pressure.

The maximum shear stress depth distribution calculated by Eq. (15) is shown as solid lines in the right hand of Fig. 5.6. The values of $\mu=0.5$ for the [EN] well, and $\mu=0.5$ and 0.7 for the [TZ] and [AS] wells are taken for the calculations. In proportion to the increase of the vertical stress with depth, the shear stress, which is required for frictional sliding, also increases with depth. In the case of the [EN] site, the measured shear stress increases with depth linearly, and the frictional coefficient is in agreement with $\mu=0.5$. These facts support the idea that the "yield stress

model", which is controlled by the frictional sliding, is applicable to the mechanism of the stress distribution in hard rocks. In brief, the calculated solid line in Fig. 5.6 is equivalent to the critical stress value for the frictional sliding. When the shear stress is added to the basement to a value more than the frictional strength, frictional sliding of the microfractures will occur. Consequently, the shear stress regresses to this solid line. However, the μ value is variable depending on the conditions of the basement.

The data from the [TZ] well are too few to describe in detail. In the case of the [AS] well, some data are over the line of μ=0.7, but half of the data concentrate around the line of μ=0.5. In considering μ=0.5 at the [EN] site, the value of 0.5 is inferred as a representative frictional coefficient of the granitic rocks in this region. In the area controlled by the shear stress over the line of μ=0.5, the μ value will vary depending on the homogeneity of the lithology. As a result of this variation of μ, it can be stated that the stress distribution in the hard rocks fluctuates greatly.

5.3 Frictional coefficient and stress estimation

In reference to the estimation of the stress state at a deeper area for each site, it is necessary to determine the frictional coefficient μ from the in situ stresses measured in any given length, usually about 30 meters. Using the μ value, the maximum stress (S_{max}) or minimum stress (S_{min}) can be calculated if one of the values is known (TSUKAHARA and IKEDA, 1989a). Using Eqs. (13) and (14) and the relation $S_S=\mu S_N$, S_{max} and

S_{min} are given as follows:

When S_{min} is known,

$$S_{max}=(1+\mu)S_{min}/(1-\mu)-2\mu P_p/(1-\mu) \quad (16)$$

and when S_{max} is known,

$$S_{min}=(1-\mu)S_{max}/(1+\mu)+2\mu P_p/(1+\mu) \quad (17)$$

In addition, the vertical stress (S_V) can be calculated approximately by using the rock density. Hence, in the cases of the stress state of both the normal fault type ($S_V=S_{max}$) and the reverse fault type ($S_V=S_{min}$), the unknown stress magnitude can be calculated without the measured stress data:

When the stress state is the normal fault type,

$$S_{max}=S_V=Dh/100 \quad (18)$$

and

$$S_{min}=S_{Hmin}=[Dh(1-\mu)/(1+\mu)+2\mu P_p/(1+\mu)]/100 \quad (19)$$

when the stress state is the reverse fault type,

$$S_{min}=S_V=Dh/100 \quad (20)$$

and

$$S_{max}=S_{Hmax}=[Dh(1+\mu)/(1-\mu)-2\mu P_p/(1-\mu)]/100 \quad (21)$$

where D is the rock density (g/cm^3), h is the depth (m) and the unit of the stresses is MPa. When a rock property has an extreme variation, the stress increasing gradient also changes at a remarkable depth due to the variation

of the μ value.

Fig. 5.8 summarizes the relations between S_S and S_N, and classifies the hard (black circles) and soft (open circles) rocks. The data from the [TR] site are included. The solid line is the best fit drawn by the least squares method for all the data. The gradient of this line is, that is the frictional coefficient, $\mu = 0.52$. Most of the data tend to concentrate around this line. Some of the hard rock data, however, deviate largely from this line. The deviation comes from data which belong to the stress concentration zone of the [AS] site.

The μ value is not always the same as that determined from the laboratory experimental data. This is because the μ might be varied by the effect of the geological scale or strain ratio. BYERLEE (1978) reported the following relations between S_S and S_N, in which the S_N ranges from 20 bars to 17 kilobars by rock friction experiments:

$$S_S = 0.85 S_N \qquad (\text{for } S_N < 2\text{kb})$$

$$S_S = 0.60 S_N + 0.5 \qquad (\text{for } 2\text{kb} < S_N < 17\text{kb})$$

BYERLEE's study further stated that these relations were realized without regard to the rock types, a temperature range of up to 500°C and the strain ratio. Fig. 5.9 shows the result of the S_S versus the S_N relationship for all the data in the Kanto-Tokai area. The following relation is calculated by the least squares method with the correlation coefficient of 0.96:

$$S_S = 0.57 S_N - 0.61$$

The value where $\mu = 0.57$ is an average value which includes both hard and soft rocks. However, it is evident that this value differs from the value

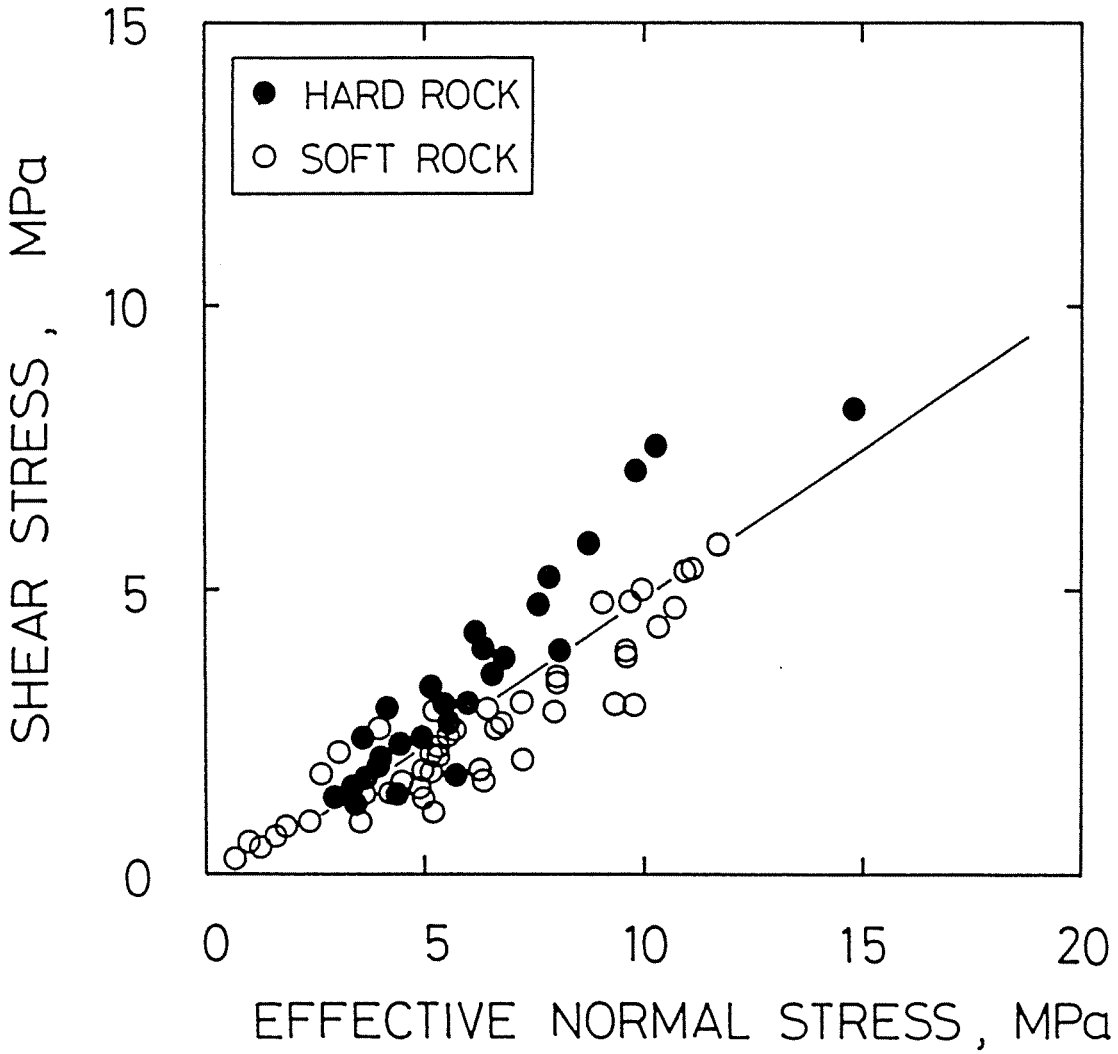

Fig.5.8: In situ shear stress versus effective normal stress for both the soft and hard rocks. The solid line indicates the best fit obtained by the least squares method for all the data.

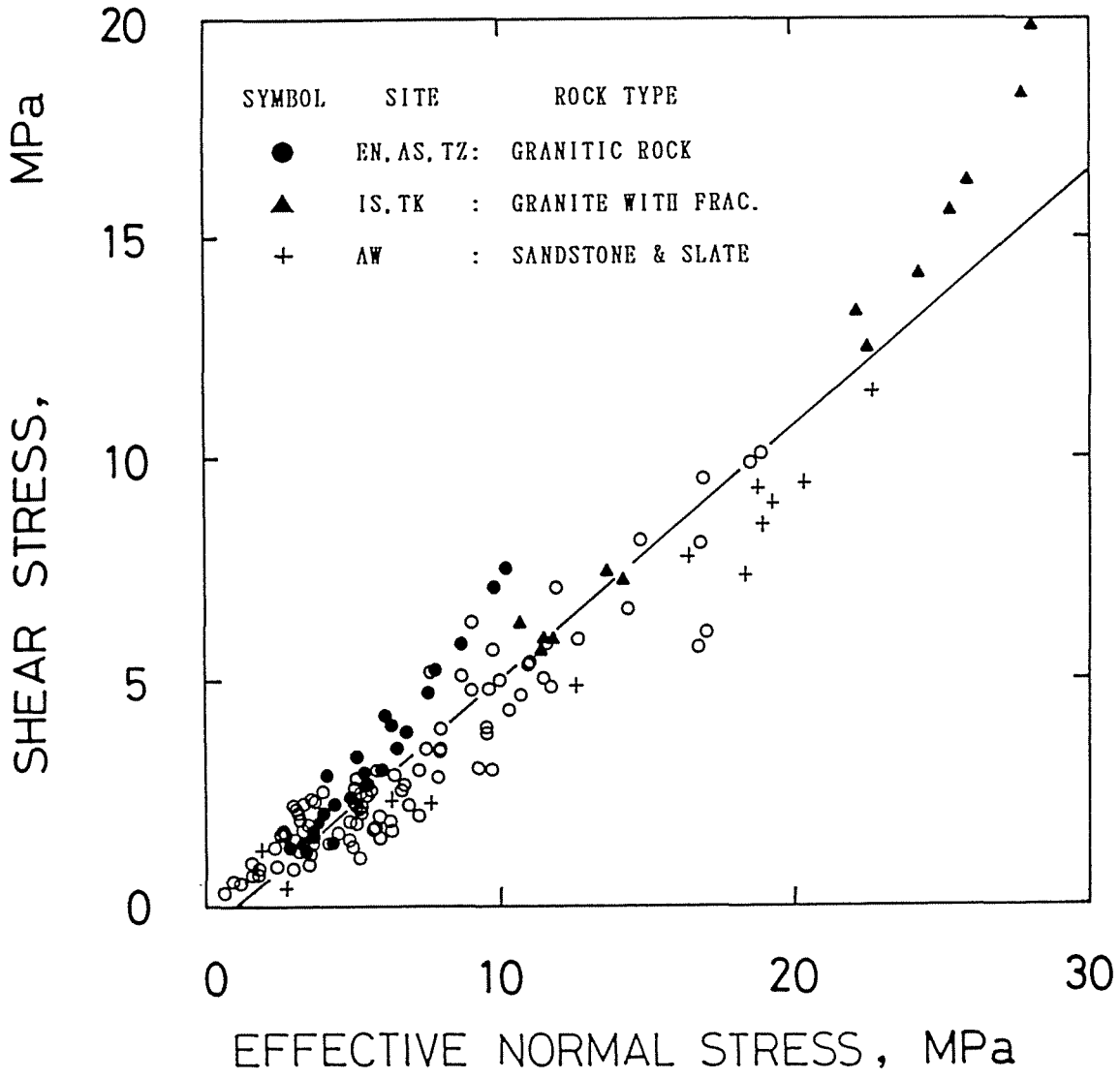

Fig.5.9: In situ shear stress versus effective normal stress for all sites. The solid line indicates the best fit obtained by the least squares method for all sites' data.

of μ=0.85 obtained by the laboratory experiment. The data deviating largely from the line of μ=0.57 belong to a characteristic area with a stress concentration zone as in hard rocks. Since the in situ value of μ can not be determined quantitatively from the rock types, it is desirable to evaluate the value from the in situ measurement data, and apply it to Eqs. (19) and (21). The value of about μ=0.6, which does not contradict BYERLEE's (1978) results, is considered as a criterion for the estimation of the deeper stress state.

5.4 Conclusions

From the above discussion it is concluded that the main physical mechanism controlling the state of stress in the shallower part of the crust is the frictional sliding based on the relation $S_S=\mu S_N$. An abnormal stress state, such as the stress concentration zone at the [AS] site, is noticeable in hard rocks because of their large contrast of homogeneity. The value of μ varies by not only rock type but the conditions surrounding the rocks. Consequently, each measurement site has its own characteristic μ value. The relationship between S_S and S_N, $S_S=0.57S_N-0.61$, represents the average state in the Kanto-Tokai area.

CHAPTER 6:

CRACK DENSITY AND STRESS DISTRIBUTIONS

The hydraulic fracturing method can measure stresses to a considerable depth, however it does have limits within itself. In the former section, it was revealed that the main physical mechanism controlling the stress distribution is the frictional sliding which relates to the microcracks. Upon closer investigation it is found that the stress distribution corresponds to well-known material constants or the geophysical structure data of the basement. This leads to a better understanding of the stress states at deeper areas or around the sites which have preexisting conditions making it difficult for the stress measurements.

This section presents the relationships between crack densities and elastic velocities of the core materials extracted from the stress measurement depth. Furthermore, an examination is undertaken by using the borehole log data, applying it, and expanding it to one order larger to understand better the formation. From these examinations, the features of the cracks in the rocks or formations which are in abnormal stress states are examined. Rock properties in regard to the differences between rocks under either an abnormal stress state or normal state are studied. An abnormal stress state was one of the features of the stress concentration zone at the [AS] site. This concentration of stress plays the most important role in the eventual occurrence of earthquakes and their relation to crustal strength.

6.1 Crack density estimation on cores by sonic wave velocities

The elastic wave velocity distribution in the earth is investigated by the analysis of earthquakes or seismic surveys. Furthermore, ultrasonic velocities in cores have been studied in connection with other physical and lithological rock properties. The influence of the size, shape and density of the cracks on the elastic properties of the rocks have been recognized for some time. The effects of cracks are most apparent in the elastic wave velocities measured in rock samples. From this point of view, the crack density has been estimated by the sonic velocity measurements on core samples and the relationship between the distributions of crack density and in situ stresses has been studied. For this study cores were extracted continuously from the stress measurement borehole at the [AS] site.

Composition of cores

The cores which were used in this study of the [AS] site contain the following components: quartz, 34~48 % (excellent grain size is 0.1~2.5 mm); plagioclase, 33~46 % (excellent grain size is 0.1~4.3 mm); and potassium feldspar is not present. The cores used for this analysis were sampled from the depths of 147.7 m, 177.1 m, and 192.9 m in the [AS] well. They are classified as tonalite based upon the IUGS's granitic rock classification. The result of the analysis of the whole-rock chemistry of the cores is shown in Fig. 6.1. The rocks include 62~77 % of SiO_2 which ranges in composition from diorite to granite.

The porosity of the rocks was obtained by measuring the dry and saturated weight of the core material. Table 6.1 shows these results. The core

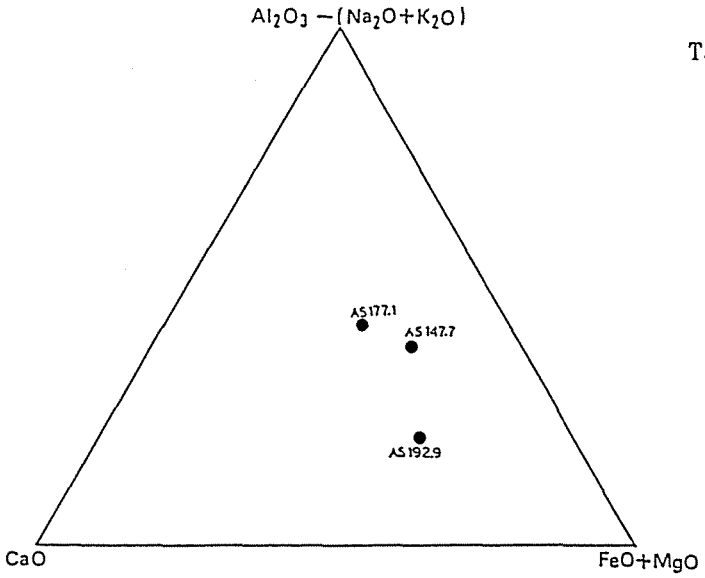

Table 6.1: Porosity of the [AS] cores

depth(m)	porosity(%)
135.2	4.9
147.7	4.5
161.4	5.4
170.5	2.7
173.6	2.6
187.25	4.3
197.55	1.2

Fig.6.1: Chemical component diagram of rock specimens from the Ashigawa well used for core tests by a fluorescence X-ray analyzing method.

material taken from the 197.55 m-depth has a slightly different quality from the others, which seems to be the same for that of the 192.9 m-depth in Fig. 6.1. Except for the 197.55 m core material, the rocks which belong to the stress concentration zone show relatively small porosity.

Breaking strength of cores

Since all of the core material was collected between the depths of 125 m and 195 m in the [AS] well, this interval was found to be suitable for the vertical continuous examination of rocks. Cores of 75 mm in diameter are extracted and arranged in a cylindrical shape, then the unconfined compression test (45 mm diameter, 90 mm length) and the tension test (45 mm diameter, 45 mm length) were conducted (SATO et al., 1987). 45 samples were taken with almost an equal sampling interval of 1.58 m, plus or minus 0.8 m.

The breaking strength distributions with the depths resulting from both tests are shown in Fig. 6.2 in comparison with the hydraulic fracturing experiment results (the same as Fig. 5.6). In the case of the unconfined compressive strength, the most adjacent depth data are mutually correlated, nevertheless large fluctuations exist. However, the tensile strength of the core rocks has no correlation to the depth distribution. In general, it has been considered that the tensile strength of the core material shows considerable fluctuation. On the contrary, the tensile strength (T_0) obtained from the hydraulic fracturing experiments shows a continuous, gradual variation with depth. The T_0 was calculated by Eq. (9), where both S_{Hmax} and S_{Hmin} were not connected with T_0. This continuity suggests that the given measurement interval was long enough to study the spatial distribution of both the in situ stress and the strength of the borehole basement.

Velocity measurement on the core materials

Ultrasonic wave velocities, Vp and Vs, were measured on the same core materials that were used for the unconfined compression test after being submerged in water for 48 hours. Axial Vp and Vs were determined by a common mid-point refraction experiment which used a pulse (200 kHz for Vp and 50 kHz for Vs) for transmission. Both velocities are plotted as a function of the depth in Fig. 6.3. A dynamic Poisson's ratio, ν_d, and a dynamic Young's modulus, E_d, are calculated from the Vp and Vs by the following equations:

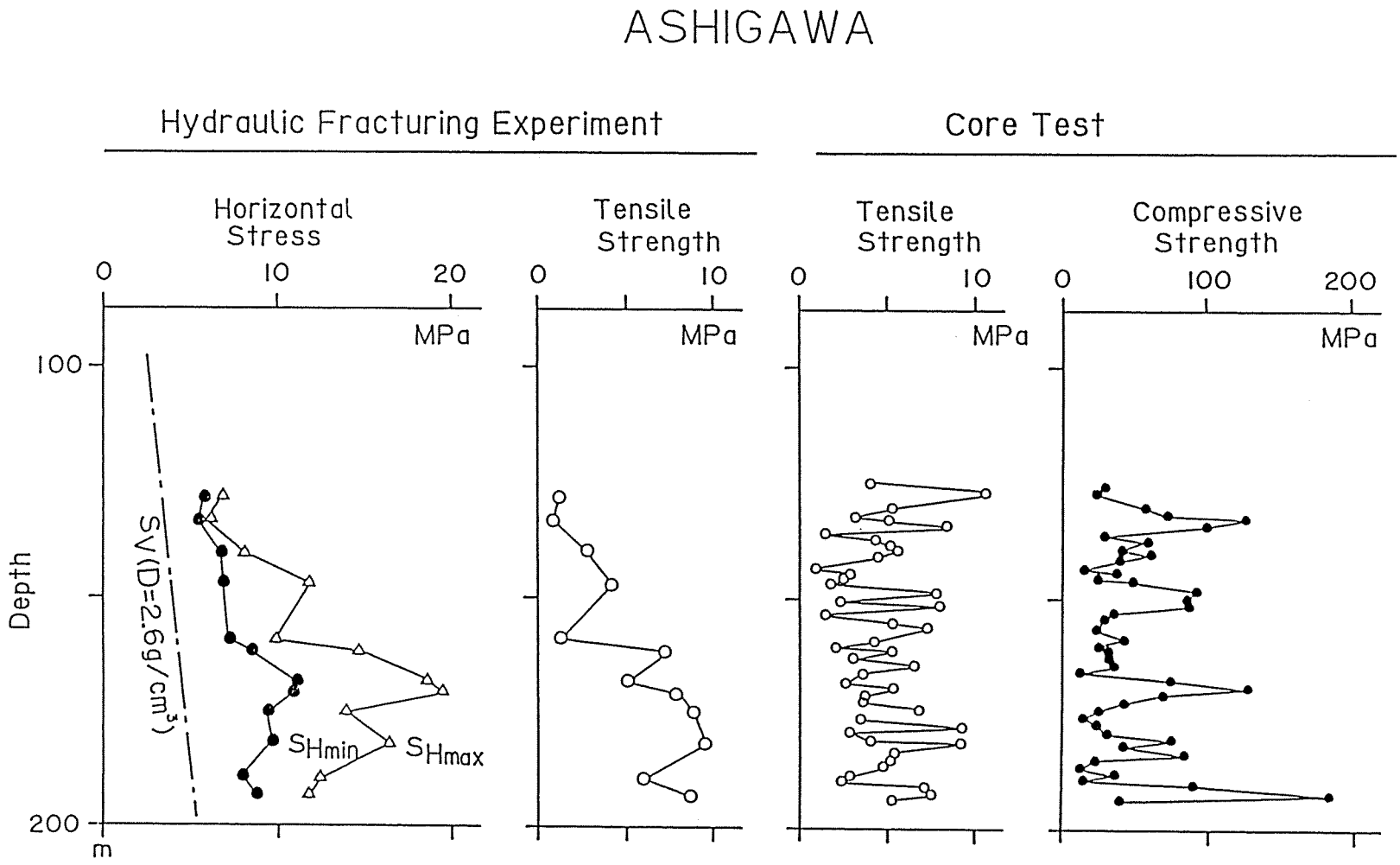

Fig.6.2: Core tensile strength and compressive strength distributions with depth. Horizontal stresses and tensile strength obtained by the hydraulic fracturing stress measurement are also shown for comparison [after SATO et al. (1987)].

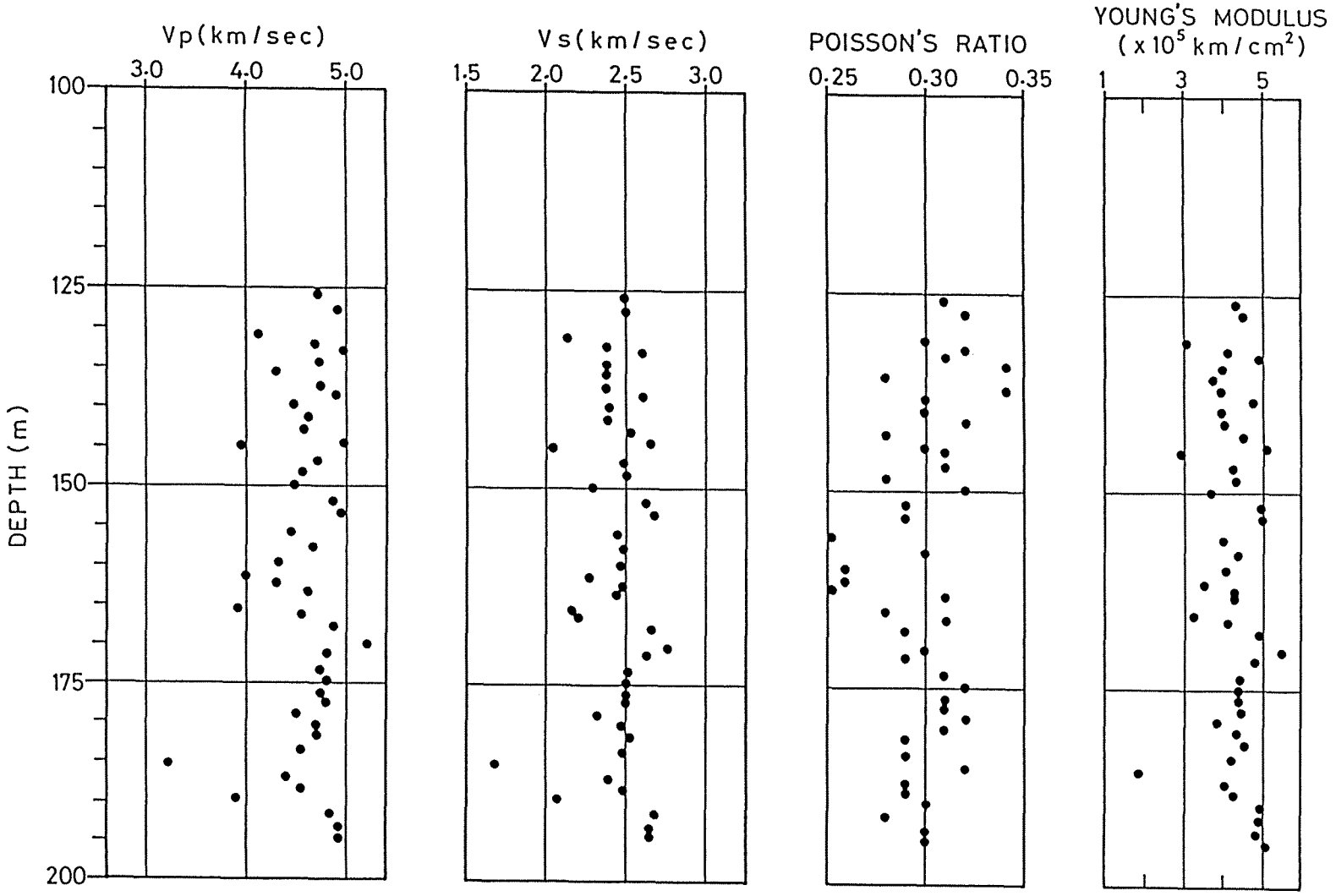

Fig.6.3: Vp and Vs measured on core specimens. Elastic constants are calculated by the velocities.

$$\nu_d = [(Vp/Vs)^2 - 2] / 2[(Vp/Vs)^2 - 1] \quad (22)$$

$$E_d = Vp^2 D[(1+\nu_d)(1-2\nu_d)/(1-\nu_d)]/g \times 10^7 \quad (23)$$

The range of ν_d is from 0.25 to 0.34 and its average is 0.30 with a standard deviation 0.02 as shown in Fig. 6.4. It is difficult to find immediately the correlation between the distributions of the P- and S-velocities and the stress depth distribution as shown in Fig. 6.2. This is the same situation between the compressive strength or tensile strength and the stresses.

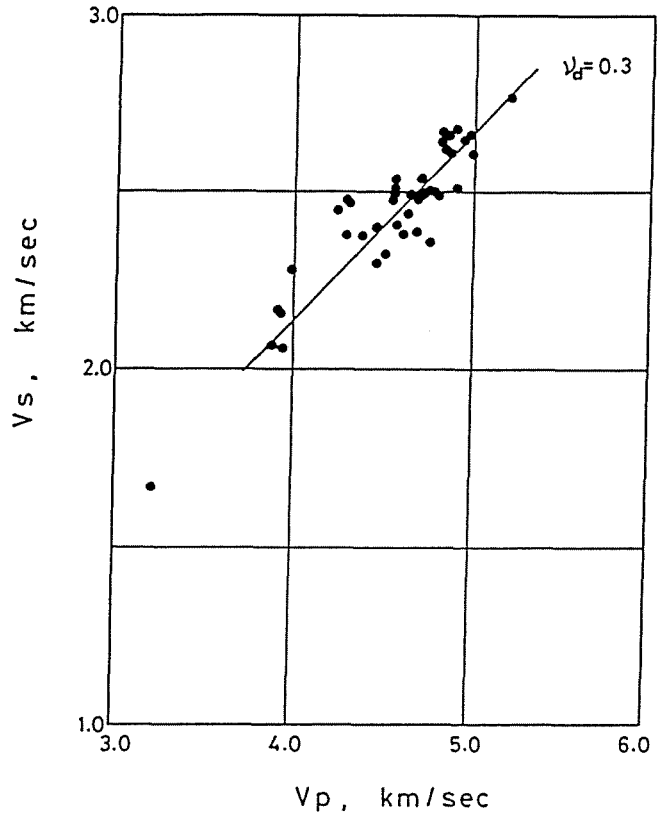

Fig.6.4: Poisson's ratio calculated by Vp and Vs.

Theories for estimation of crack density and saturated fraction

O'CONNELL and BUDIANSKY (1974) analyzed the relationships between seismic wave velocities and crack density in terms of elastic moduli. The elastic moduli were calculated through estimating the isothermal potential energy (strain energy plus load potential) of cracked bodies by using a self-consistent approximation. Their study represented the results for some cases of completely dry or saturated cracks, mixtures of dry and saturated cracks, and cracks saturated with a compressible fluid.

The crack density parameter for circular cracks is defined by:

$$\varepsilon = (\Sigma \alpha^3) / V = N < \alpha^3 > \tag{24}$$

where α is the radius of cracks, V is the whole volume, and N is the number of cracks per unit volume. It is assumed that each crack in a body is distributed randomly and partially filled with fluid. The elastic moduli of the cracked body, effective bulk modulus, K^*, effective Young's modulus, E^*, and effective shear modulus, G^*, can be calculated by using the crack density parameter, ε, the effective Poisson's ratio, ν^*, and a saturated fraction, ξ, as follows:

$$K^*/K = 1 - 16/9 \times [(1-\nu^{*2}) / (1-2\nu^*)] (1-\xi) \varepsilon \tag{25}$$

$$E^*/E = 1 - 16/45 \times (1-\nu^{*2}) [3(1-\xi) + 4/(2-\nu^*)] \varepsilon \tag{26}$$

$$G^*/G = 1 - 32/45 \times (1-\nu^*) [(1-\xi) + 3/(2-\nu^*)] \varepsilon \tag{27}$$

where K^*, E^*, and G^* are normalized by the values of K, E, and G for uncracked bodies, respectively. The velocities of shear and compression

elastic waves can be obtained directly from these equations. The normalized shear wave velocity, Vs^*, the compression wave velocity, Vp^*, and the ratio of the velocities, Vp^*/Vs^*, are expressed by:

$$Vs^*/Vs = (G^*/G)^{1/2} \tag{28}$$

$$Vp^*/Vp = [(1-\nu^*)(1+\nu)K^*/(1+\nu^*)(1-\nu)K]^{1/2} \tag{29}$$

$$(Vp^*/Vs^*)/(Vp/Vs) = [(1-\nu^*)(1-2\nu)/(1-2\nu^*)(1-\nu)]^{1/2} \tag{30}$$

where ν is the Poisson's ratio for uncracked bodies. Both the seismic wave velocities decrease with an increase in the crack density. The velocity ratio, Vp^*/Vs^*, decreases for dry cracks and increases for saturated cracks.

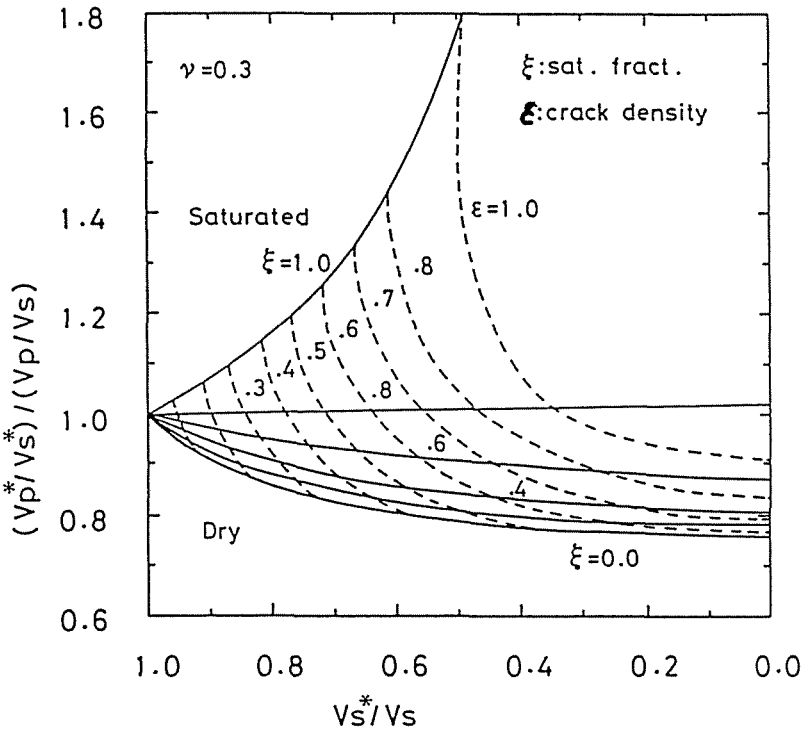

Fig.6.5: Calculated crack density and saturated fraction for Poisson's ratio of 0.3.

In the analysis, by plotting the Vp^*/Vs^* versus Vs^*, the crack density and the saturated fraction can be obtained simultaneously in a unique way. Fig. 6.5 shows the calculated result for the case of $\nu=0.3$ which is obtained from the [AS] core materials as described above. The velocity ratio, $(Vp^*/Vs^*)/(Vp/Vs)$, versus the shear wave velocity, Vs^*/Vs, is plotted for a partially saturated cracked body, which is expressed by the variation of the saturated fraction, ξ. The dashed curves indicate the constant contours of the crack density, ε.

Crack density in rocks

The effective velocities, Vp^* and Vs^*, in the above theory equal the velocities, Vp and Vs, measured on core rocks, respectively. The strict estimation of the velocities of the uncracked bodies for normalization is very difficult. It was assumed here that Vp=5.21 km/sec and Vs=2.77 km/sec, which are the highest values obtained from the core specimen at a depth of 171.15 m, and it was also assumed that they are the velocities of the uncracked bodies. Consequently, the calculated crack density and the saturated fraction of each core specimen are relative values against that of the 171.15 m core material.

Fig. 6.6 shows the normalized Vp^*/Vs^* plotted against Vs^*, overlaying the theoretical curves of Fig. 6.5. The data are classified into three groups by the frictional coefficients represented in Fig. 5.6. That is, rocks which belong to the area of $0.7<\mu$ are shown by black circles, rocks for the area of $0.6<\mu<0.7$ are shown by open circles, and other rocks of $\mu<0.6$ are shown by stars. Fig. 6.6 illustrates the following features: 1) In the case of rocks under high shear stresses of $0.7<\mu$, the crack

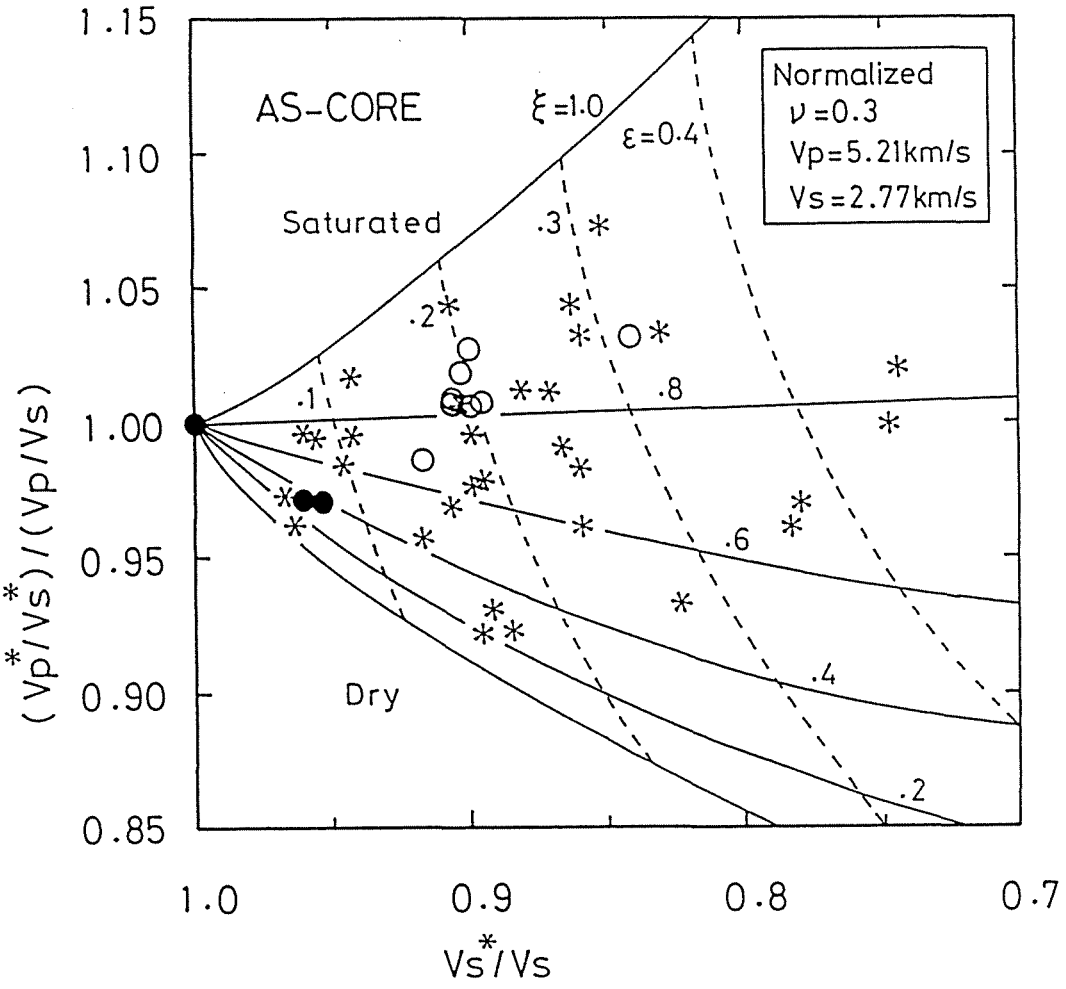

Fig.6.6: Crack density distribution on core specimens from the Ashigawa well. The data are classified into three groups by the value of frictional coefficients (see text and Fig. 5.6).

density parameters are $\varepsilon<0.1$. However, this condition is rarely observed. The saturated fractions are also relatively small, around $\xi=0.4$. 2) In the case of rocks where $0.6<\mu<0.7$, the ε varies between 0.15 and 0.32 and the ξ is around 0.8. This shows that the cracks are increased and saturated more than in the case of $0.7<\mu$. 3) In the case of rocks where $\mu<0.6$, both values of the ε and ξ tend to scatter, which suggests that various kinds of cracks are present.

In consideration of the stress distribution at the [AS] well, the features described above suggest that the number of cracks remains few in the high shear stress state before the occurrence of frictional sliding. Then the cracks increase in the process of stress yielding to the frictional sliding. In the state immediately "after" this yielding, the mixing of open and closed cracks occurs. It is also noted that the rock properties connected with cracks is a large factor for the stress heterogeneity, such as that which is evident in the [AS] well.

It has been recognized that the elastic wave velocities change due to the opening of new cracks as a function of the hydrostatic pressure in laboratory experiments (e.g. LOCKNER et al., 1977; KAJIKAWA et al., 1990). It is questionable whether it is possible to compare directly these results with the rock breakout test under high pressure. However, it is consistent with the fact that the elastic wave velocity increases with an increase in the external pressure. This effect is interpreted as the fact that the cracks are squeezed and ultimately closed to an inelastic state by external pressure (O'CONNELL and BUDIANSKY, 1974). It is of particular interest to note that the stress magnitude relates to the elastic wave velocities from the stance of the rock properties in connection with their cracks.

6.2 Crack density estimation in formations by sonic log data

Coring from any given depth in each borehole is sometimes difficult, so it is not always good or possible to compare the rock properties by using core materials from different sites. On the other hand, the geophysical logging data are used for comparison studies because they can be obtained from all depths in each site. In this section, sonic log data are examined and applied by the same way as the core materials' analysis in consideration of the formation fractures. It is a matter of course that the log data reflect the in situ state such as the degree of saturation, pressure conditions and the size of fractures, to name a few.

Sonic log data

Sonic log data were obtained all the way to, as well as from, the bottom of both the [AS] and the [EN] wells. Commercial equipment (Sonic Sonde by Geophysical Surveying and Consulting Co., Ltd.) for sonic logging (transmitter-receiver interval, 3 feet; natural frequency, 25 kHz) was used, and only the p-wave velocity, Vp, was shown for the sonic log results (see Fig. 5.5). It is a rarity that the shear wave velocity, Vs, is shown. However, wave train records for every 10 meters and continuous variable intensity records were obtained as the sonic log data. It is possible to read the arrival time of the P- and S-waves, and hence the reciprocal of the Vp and Vs. Fig. 6.7 shows examples of the wave train records from the depths of 130 m, 170 m and 197 m in the [EN] well. Based on the travel times over a unit distance on the wave train records, both velocities were determined at every 25 cm interval on the variable intensity log records

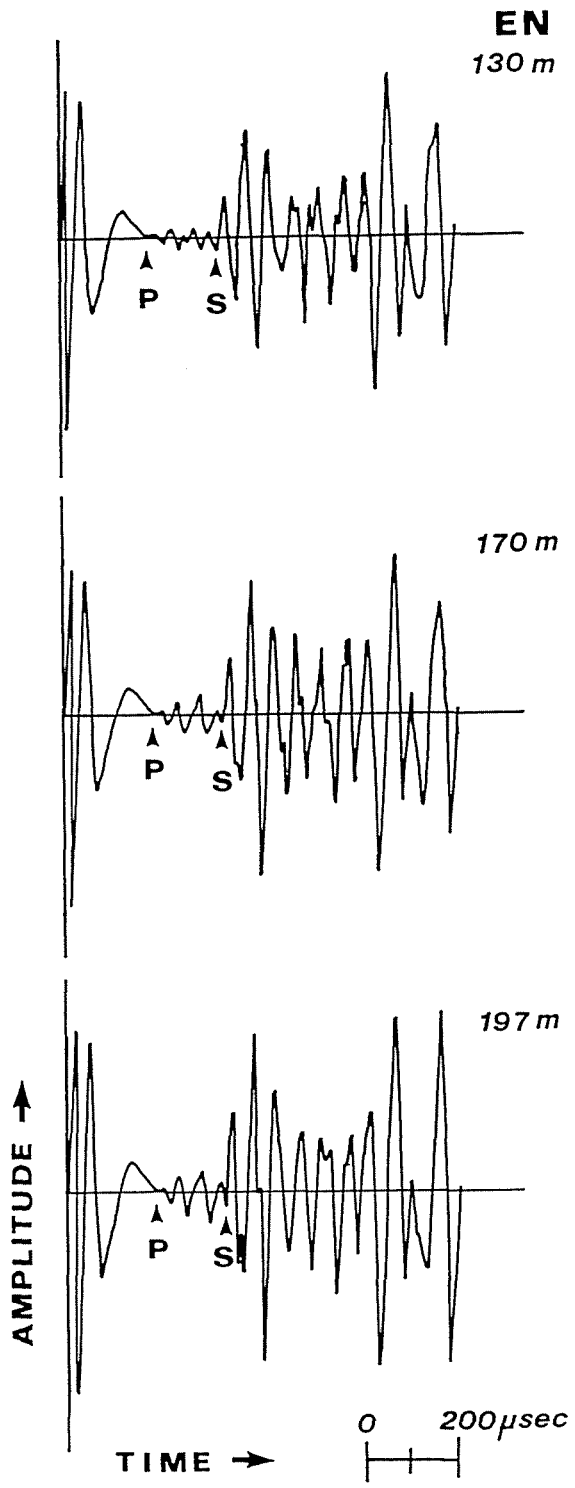

Fig.6.7: Examples of wave train by sonic log at the depths of 130m, 170m and 197m in the Ashigawa well.

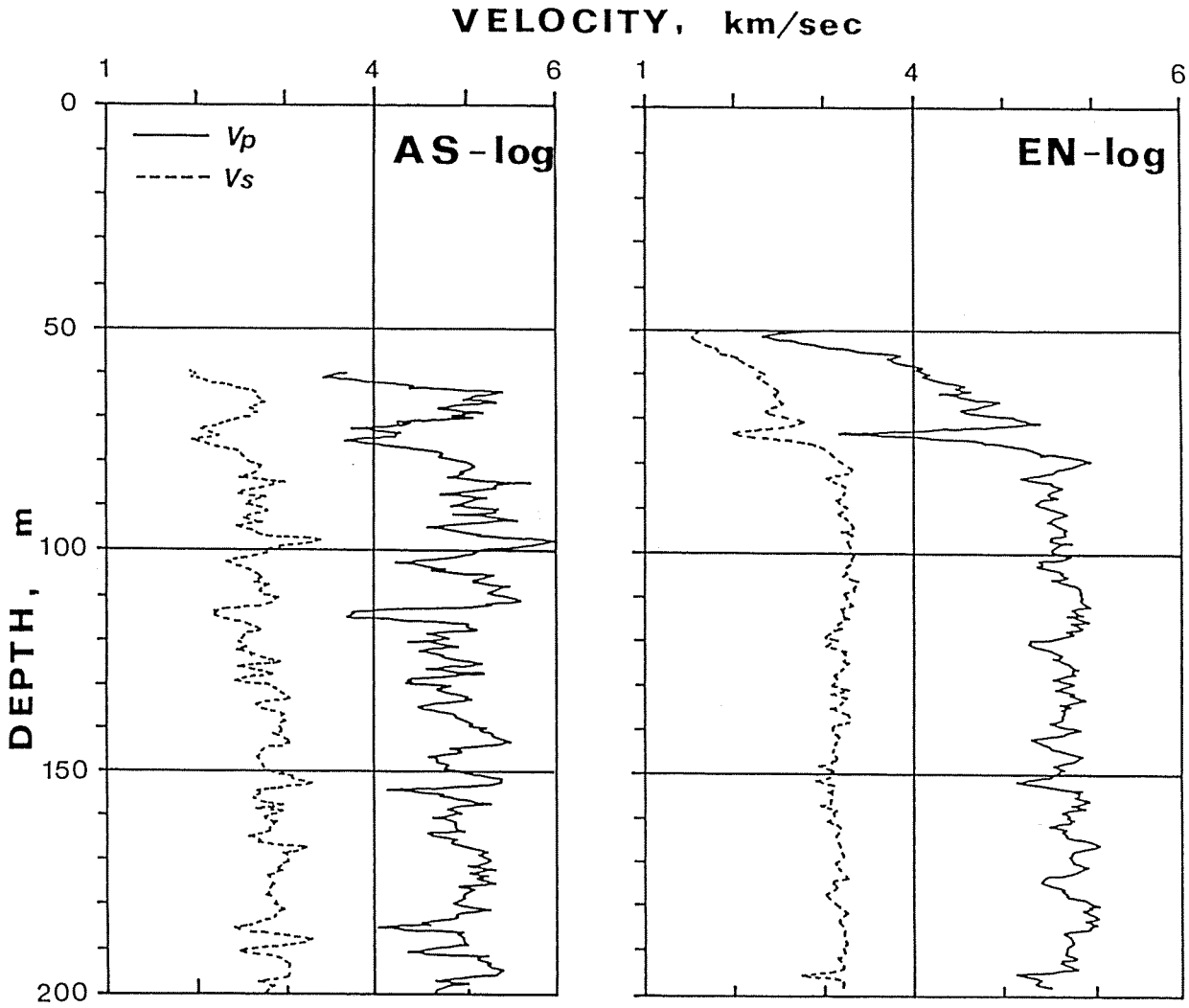

Fig.6.8: Velocity profiles obtained by sonic logs in both the Ashigawa and Enzan wells.

with a calibrating borehole diameter measured by caliper logging.

Fig. 6.8 shows the velocity depth variations obtained for both the [AS] and [EN] wells. The log velocity data in the [AS] well corresponds to the core velocity data (Fig. 6.3) on the whole, while locally some fluctuations, which seem to be influenced by in situ lithological fractures, are also seen in the log data. SATO et al. (1987) presented the autocorrelation of this fluctuation in the log and core velocity data in the direction of the depth in the [AS] well. As a function of the depth, h, the fluctuation, $\delta\phi(h)$, is determined by subtracting the average value, ϕ_0, from the measured value, $\phi(h)$. Then the autocorrelation function, N(u), is calculated as a function of the lag, u. As a result, the autocorrelation of the Vp log data is 13% at a lag of 1.5 m and 33% at a lag of 3 m, and it has the fluctuation of about a 3 m wavelength. On the other hand, the Vp core data is below 10% at a lag of 1.58 m as the sampling interval. When comparing the [AS] with the [EN] log data, a larger fluctuation in the velocities is shown in the [AS] well. It appears that the heterogeneity of the basement lithology effects this fluctuation. The heterogeneity of both sites were examined in terms of the crack density distribution, as in the same manner with the core data.

Crack density in strata

The log data for the [AS] well is shown in Fig. 6.9, plotted on the figure of $(Vp^*/Vs^*)/(Vp/Vs)$ against Vs^*/Vs, as reproduced from Fig. 6.6. For the normalization, however, Vp and Vs were not assumed to be the highest measured values. Considering the situation that some areas of the borehole wall happen to be in a completely saturated condition (ξ=1.0),

the velocities for normalization were determined reversely by shifting the curves to adjust any data to the curve of ξ=1.0. Consequently, Vp=5.73 km/sec and Vs=3.54 km/sec were determined to be the normalization values. The data in Fig. 6.9 are also classified into three groups, the same as Fig. 6.6. In comparison with these two figures, the absolute values of the crack density and saturated fraction are different due to the influence of the Vp and Vs used for the normalization, so only the relative variation tendency of the crack distribution must be discussed.

The data (black circles) in the high shear stress state are generally in the region of ε=0.25~0.4 and ξ=0.8~1.0. In view of the estimated errors of the data, no significance can be placed on the detailed variations. Nevertheless, it is obvious that the data correspond to predominantly saturated cracks of the crack density ε=~0.3. In the case of the data (open circles) which are in the process of stress yielding to the frictional sliding, the crack density increases to the range of ε=0.35~0.5. The saturated fraction, however, is ξ=0.8~1.0, and is almost the same condition as it is in the high shear stress state. The increase of the crack density accompanies the rise in the Vp^*/Vs^* ratio. This is illustrated in Fig. 6.9 and shows that the Vs^* decreases instead of a nearly constant Vp^*, which is dependent on the crack growth. Crack growth under constant saturation suggests a supply of fluids from the surrounding areas. In the case of the data (star symbols) which are in the state "after" the yielding, the mixing of open and closed cracks occurs as shown by the scattering of the crack density and the saturated fraction. This mixing seems to contribute to the supply of fluids. Further, the decrease of the Vp^*/Vs^* occurs at various crack densities. This feature suggests that low saturated parts

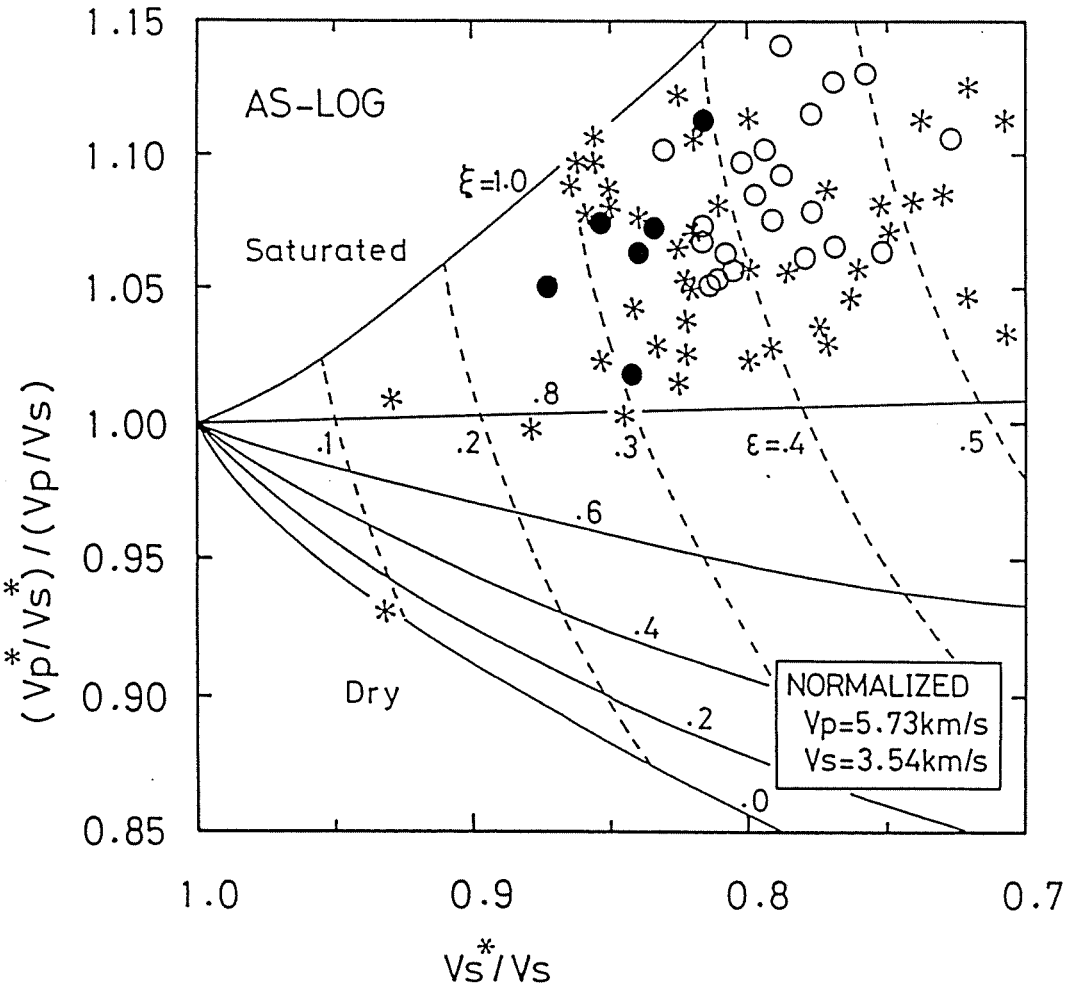

Fig.6.9: Crack density distribution obtained by sonic log data on the Ashigawa well. The data are classified into three groups, the same as Fig. 6.6.

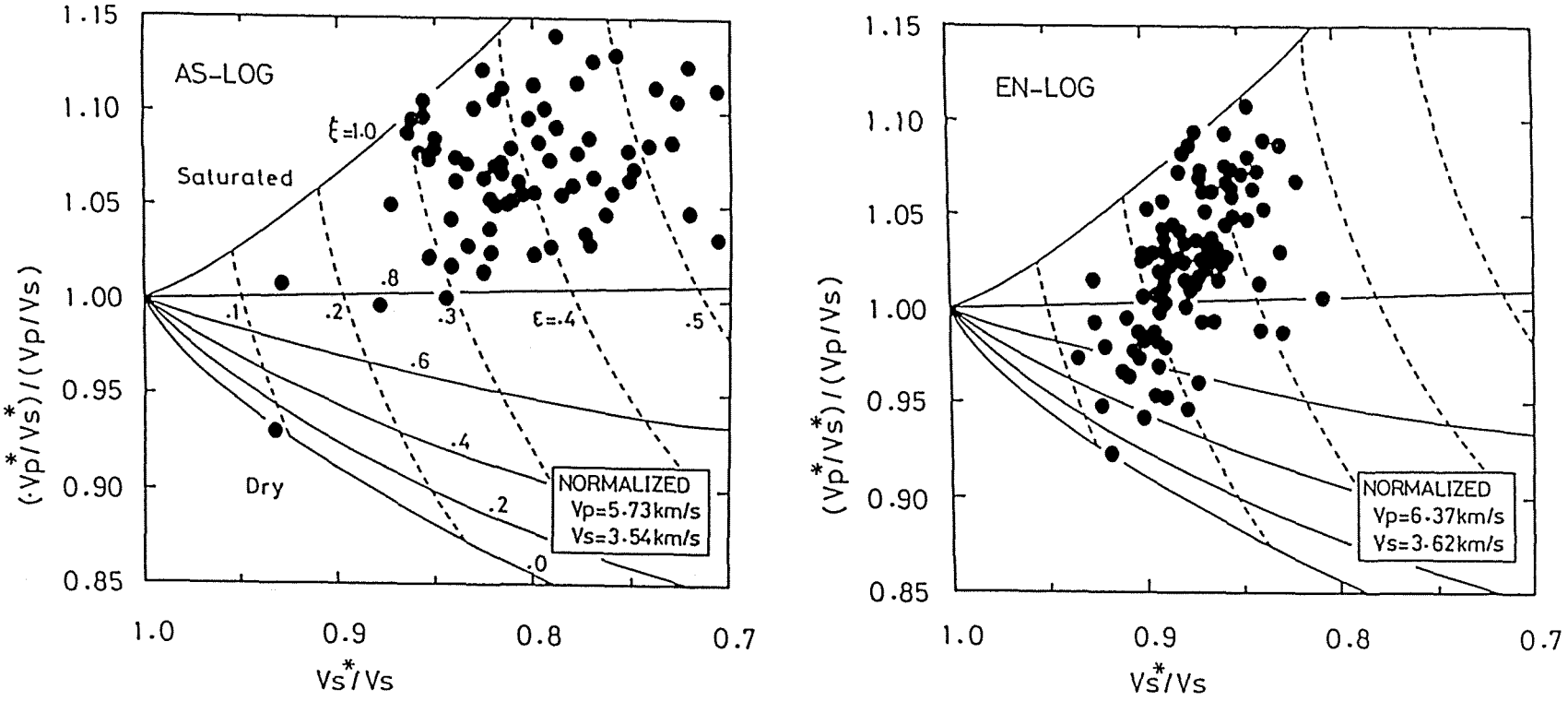

Fig.6.10: Comparison of crack density distribution obtained by sonic log data between the Ashigawa and Enzan wells.

have developed in the area that was previously completely filled with fluid.

Fig. 6.10 shows the comparison of the crack density distributions between the [AS] and the [EN] wells. The crack density distribution of the [AS] well varies much more than that of the [EN] well. The presence of various states of cracks is effected strongly by the lithological heterogeneity and also by the stress variations. This effect appeared markedly in the [AS] well. Also, this heterogeneity is revealed by the relationships between the measured Vs* and the crack density as shown in Fig. 6.11.

6.3 Conclusions

The analysis of crack density using core materials and logging data revealed that the lithological heterogeneity, which is provided by the velocity variation, contributes greatly to the local stress distributions such as stress concentration. In the case of absolutely homogeneous lithology, the stresses increase with depth with little or no fluctuation, without regard to the rock types. This fact infers that stress distribution in the shallower part of the crust complies basically with the "yield stress model" controlled by the slidings of microfractures. On the contrary, as in the case of heterogeneous hard rocks, large stress yielding occurs in areas with many fractures. Consequently, the relatively hard areas with few or no fractures compensate the stress yielding and cause high stress areas such as the stress concentration zone. To cause this abnormal stress state, the relatively hard area is needed to continue for an interval with a scale of 30 m or more, as determined from the estimation of the [AS] well.

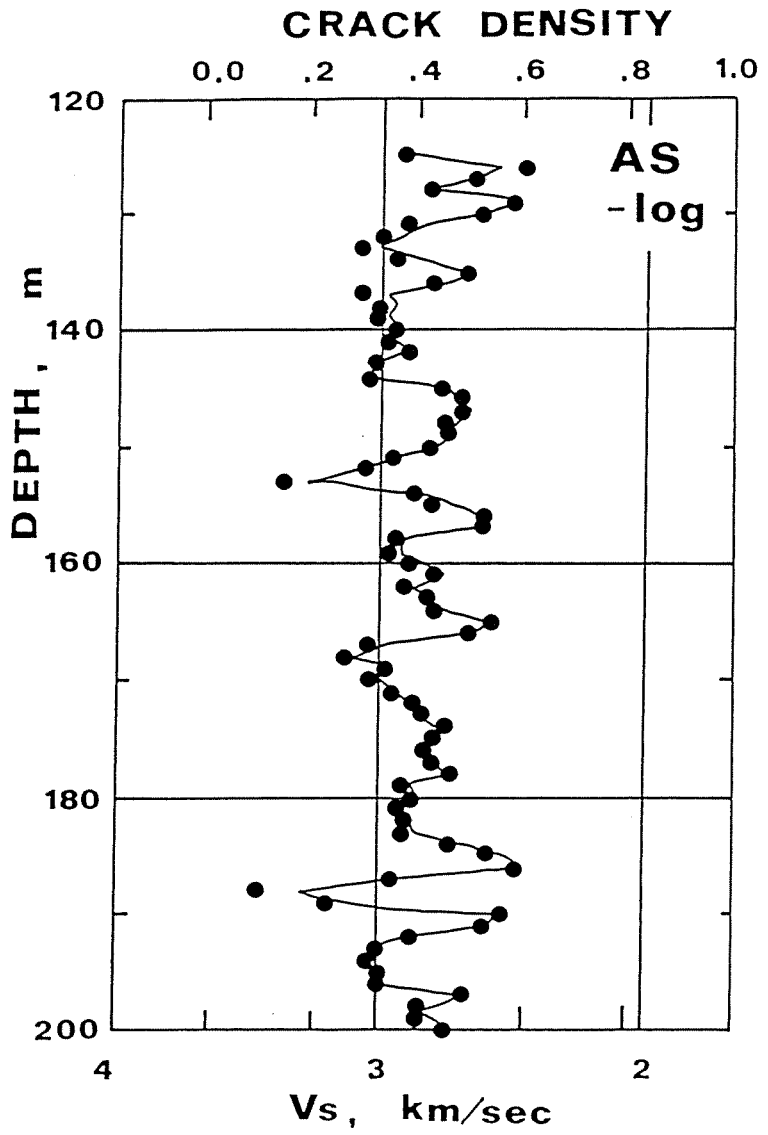

Fig.6.11: Crack density is compared with Vs as a function of depth in the Ashigawa well.

CHAPTER 7:

STRESS DISTRIBUTION MAP

A regional distribution map of the stress orientation is indispensable for the consideration of tectonic problems. A "World Stress Map" has been drawn with stress data collected from all over the world (ZOBACK et al., 1989; MASTIN et al., 1989). In regard to the Kanto-Tokai area some stress orientation maps have been proposed and the relationship of regional tectonics and the stress orientation have been studied by TSUKAHARA and IKEDA (1983b, 1986, 1987, 1989b and 1991), and SUZUKI (1989), to name a few. Compiled stress orientation data include not only in situ measurement data but seismological and geological data. However, a stress distribution map for the stress magnitude has not yet been summarized to date. This is because the comparison and discussion of the different regional stress states are very difficult due to the lack of the measurement data from deeper crustal areas and the complexity of the geological conditions of each site. In this chapter, a stress magnitude map reflecting the physical mechanism of the control of the stress distribution is proposed. The stress magnitude is proportional to the amount of strain accumulated up to the present. Therefore, it is very important to compare the absolute stress values between the areas for the estimation of the possibility of earthquake occurrence.

7.1 Stress orientation map

The directions of S_{Hmax} measured by hydraulic fracturing are shown in Fig. 4.8. The stress orientation distribution in the Kanto-Tokai area is

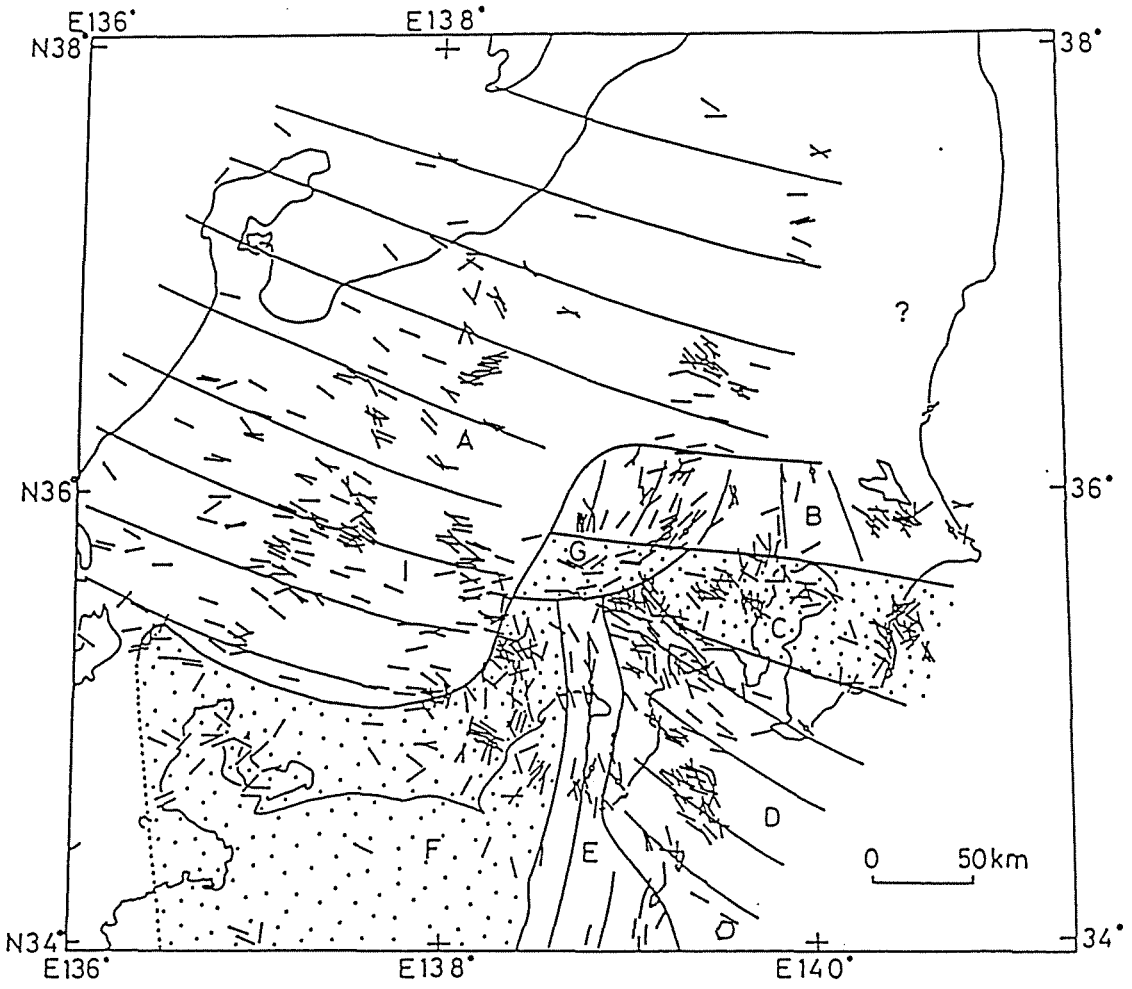

Fig.7.1: Stress province map. A thick line indicates the boundary between the stress provinces, and a thin line indicates the average S_{Hmax} direction for each stress province [after Tsukahara and Ikeda (1991)].

expected to be very complicated because of the influence of the relative movements among the three plates, the Philippine Sea, Pacific and Eurasian plates (see Fig. 3.1). The measurement results shown in Fig. 4.8 also seem initially to be not systematic. Recently, TSUKAHARA and IKEDA (1991) explained the existence of stress provinces and discussed their causes. Their study was based on a stress province map of the central part of Japan, including the Kanto-Tokai area, which was a compilation of the stress orientation data measured in situ and obtained by the focal mechanism analyses. A stress province map is shown in Fig. 7.1. The earthquakes used for the focal mechanism analysis are those that occurred at depths shallower than 35 km with magnitudes ranging from about 2.5 to 7.0 on the Richter scale. In this figure, the relative magnitude relationships between the horizontal stresses and the vertical stress, in other words the fault types, are considered but the absolute values of the stresses are not discussed. In situ stress measurement is the only way to obtain the stress magnitude in spite of the limitation of the measurement data itself. Especially for the areas where earthquakes rarely occur, in situ stress measurement plays an extremely important role in understanding the stress states there.

7.2 Stress magnitude map

Fig. 7.2 shows an example of a stress magnitude map. Each site's stress magnitude at the depth of 500 m is obtained by the extension of the line with an average stress-depth gradient (see Table 4.2). Further, the major axis of the ellipse indicates the S_{Hmax} direction for each site. Since this kind of figure can elucidate directly the in situ stress magni-

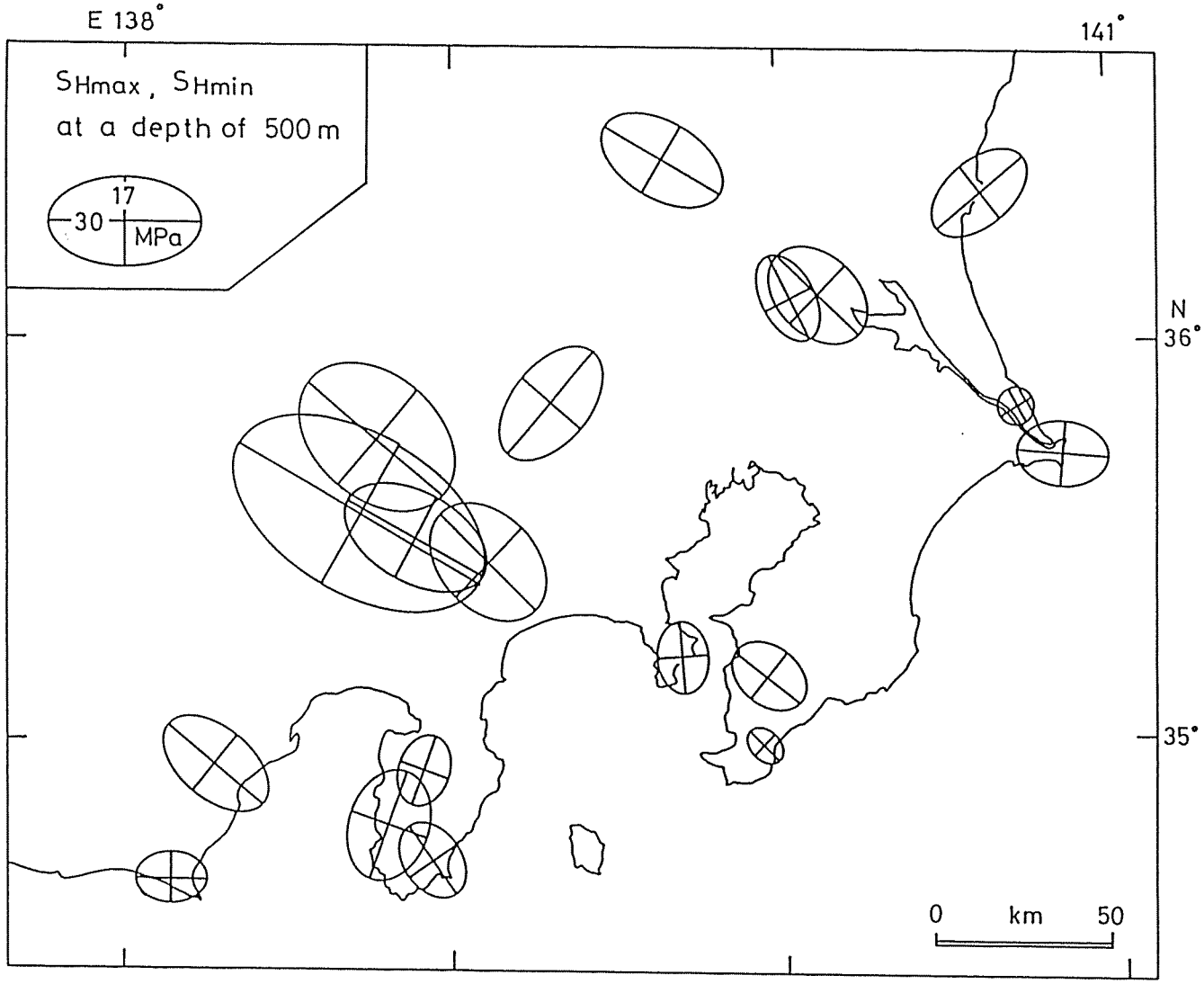

Fig.7.2: Stress magnitude map at the depth of 500m. The long line in each ellipses indicates the S_{Hmax} direction.

tude at any depth for each site, it is very useful. However, it is questionable whether the regional or tectonic stresses are reflected appropriately in these stress values because of the linear approximation of the stress-depth distribution. For example, in an area around the Kofu basin where the hard rocks are distributed, as discussed in Chapter 5, extreme stress differences seem to appear. This is because the abnormal stress distribution feature of each site is not considered in Fig. 7.2. Thus it is noted that various geological conditions should be taken into consideration to compare the tectonic stresses among sites.

Looking at stress magnitude distribution on a scale, it is apparent that there are different scale orders which can be considered: for example, a wide area tectonic stress scale, from several tens to hundreds of kilometers, or a rock mechanical local stress scale, ranging from several meters to tens of meters. If the scales can be divided into three orders, local, regional, and tectonic stress orders, each of them could be defined as follows: Local stress: small geological (rock quality or formation) unit scale stress that has individual characteristics for measurement sites or boreholes. Regional stress: large geological (stress province) unit scale stress which is characterized by the fault movement or focal mechanisms. Tectonic stress: stresses caused by the relative movement of plates. On closer analysis regarding which stress orders are included in the measured stress magnitudes, one can come to a better understanding of the real tectonic stress state in a given area.

It has become evident that the heterogeneity of the formations is one of the important influencing factors on local stress distribution, as was previously indicated. It has also been pointed out that there is a close relationship between the shear stress distribution and the seismic wave

structure which reflects the heterogeneity of the formations. The P-wave velocity, Vp, obtained from the borehole logging is plotted against the average shear stress gradient for each site in Fig. 7.3. The average shear stress gradient tends to increase with an increasing Vp value. Additionally, it seems to reflect the regional differences. For example, the values of the average shear stress gradient are distributed widely around the range of Vp=4 km/sec. It has been revealed that each region has its own frictional coefficient, μ, as described in Chapter 5. This difference of the μ value causes the variation of the shear stress gradient. Therefore, the shear stress gradient estimated by using the μ value reflects the regional stress. In addition, it is reasonable to consider that the average of the shear stress gradient, excluding the abnormal stress areas, represents this regional stress. This is because the shear stress yields in an almost equal fashion throughout any given formation which is comprised of basically homogeneous rock properties. Fig. 7.4 is a stress magnitude map in which the size of the circles indicates the average shear stress gradient value. The numbers near each circle indicate the mean μ value for each site. The contrast of the stress magnitude seems to be well represented in this map. It is necessary to use the data measured from at least a 200~300 m long continuous interval, as well as from several neighboring sites to discuss the tectonic stress state of any given region.

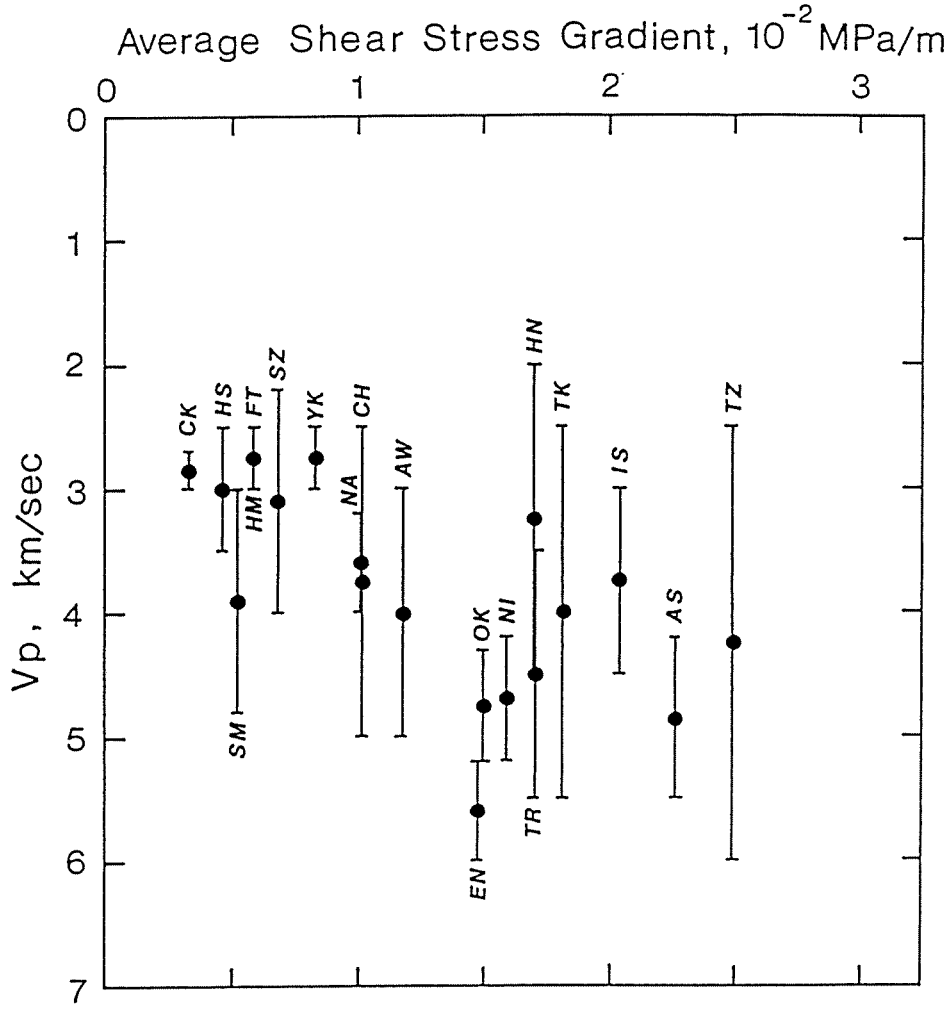

Fig.7.3: Average shear stress gradient versus Vp which is obtained by the sonic log in each well.

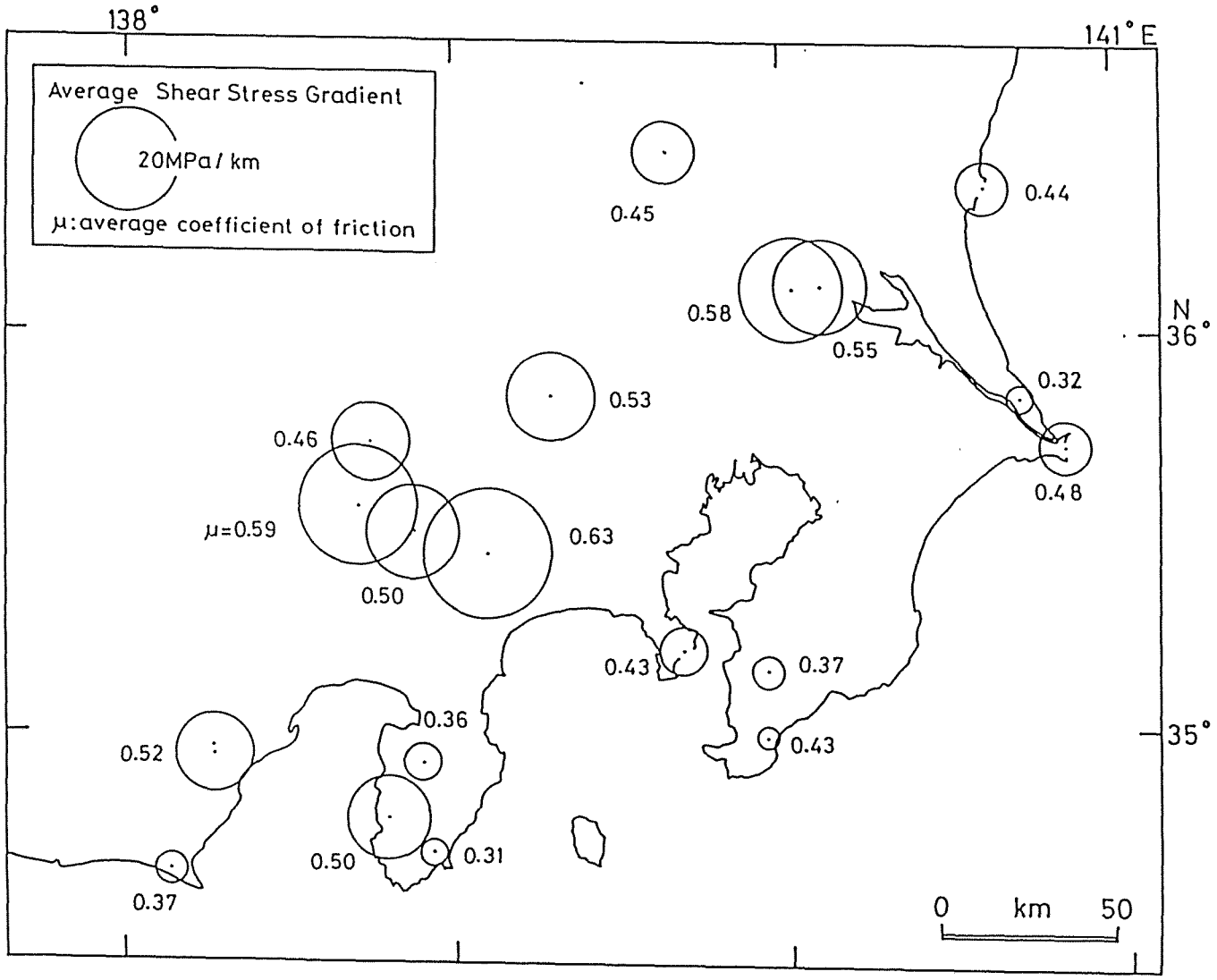

Fig.7.4: Stress magnitude map drawn by the average shear stress gradient. The numbers near each circle indicate the mean frictional coefficient for each site.

CHAPTER 8:

SUMMARY

It is indispensable for the research of earthquake occurrence mechanisms and/or tectonics to reveal the state of stress magnitude distributions in the crust. Up to now very little has been stated about the physical mechanism(s) and the controlling factors concerned with these stress magnitude distributions. One of the reasons is that there have not been enough measurements taken of in situ stresses for this kind of analyses. Another reason is the difficulty of the analyses due to the fact that geological and tectonic conditions influence and complicate the in situ measured data. Based on these facts, the principal object of this study was to reveal the characteristics and physical mechanism(s) of the in situ stress spatial distribution from the analyses of the stress data measured sensitively by the hydraulic fracturing method. In order to better understand these characteristics and mechanism, the rock material properties have been investigated in relation to the stress magnitude distributions. A regional distribution map of the stress magnitude is also proposed by applying these summarized results for the purpose of further tectonic studies.

In conclusion, the following can be summarized:

1) New techniques (a measurement system, including high pressure pumps, multiple impression packers, etc.) and a "curve fitting method" for the interpretation of the shut-in pressure are proposed for the hydraulic fracturing stress measurement. As a result, both the stress magnitude and orientation data can be obtained sensitively throughout the entire depth of

a 1,000 m class borehole.

2) The stress states are revealed at 20 sites in the Kanto-Tokai area. Accumulated data indicate that the reverse fault type of a stress state is prevalent in the Kanto-Tokai area. The vertical distribution of the average horizontal stress of all the sites is expressed as $S_{Hav}=0.035h+0.1$, where the unit of stress is MPa and the depth (h) is in meters. The higher stress sites, which belong to the group above this approximate line, are composed of relatively hard rocks, of which the density is larger than 2.3 g/cm^3. With regards to each site, the stress magnitude distribution often shows a heterogeneous state, which is influenced by the inhomogeneity of rocks or formations which are on a small scale geological unit. In general, the data obtained in hard rocks show that the stresses tend to fluctuate largely. Maximum shear stress depth distributions are found to be in almost the same way as this large fluctuation tendency of the principal stresses.

3) It is revealed that the main physical mechanism controlling the state of stress in the shallower part of the crust is the yielding of the basements dominated by the frictional sliding of the micro-cracks. An abnormal stress state, such as a higher stress area compared to its surrounding area, is noticeable in hard rocks. The value of the frictional coefficient, μ, varies by not only the rock types but also the conditions surrounding the rocks. Consequently, each measurement site has its own characteristic μ value. The relationship between S_S and S_N, $S_S=0.57S_N-0.61$, represents the average shear stress state in the Kanto-Tokai area.

4) The difference of rock material properties connected with cracks is an important factor which contributes greatly to the occurrence of

stress heterogeneities, such as stress concentration areas in the formations. This fact is indicated by the result of the comparison between the crack densities, which are obtained from the core materials and logging data and the shear stress distributions. The following phenomena are recognized by this comparison: The number of cracks remains few in a high shear stress state before the occurrence of frictional sliding. Then the cracks increase in a process of the stress yielding to the frictional sliding. In the state immediately "after" this yielding, the mixing of open and closed cracks occurs. These phenomena suggest that a relatively hard area with few or no fractures is needed to continue for an interval with a scale of 30 m or more to cause the abnormal stress state.

5) For regional stress magnitude maps, it is proposed that a shear stress depth-gradient map reflects the frictional coefficients characteristic for each site. It will be very useful for further investigations to examine the association of the stress orientation map with regional tectonics.

To estimate accurate stress states at deeper areas, other additional problems should be solved. For example, the hydraulic fracturing stress measurement method has been established through its techniques; however, at very deep areas, deeper than 5,000m, the capacity of the measurement equipment is not enough owing to the high pressure and high temperature present at such depths. Further, it is considered that hydraulic fractures must occur on the borehole wall due to high mud water pressure during the drilling process. Therefore, the estimation of the stresses by other methods is necessary. Such methods useful for this estimation could be the borehole breakout method, which detects the deformation in a borehole itself, or the

strain recovery method, which uses core materials.

Since rocks are dense and hard with an increase in depth, the amount of stress yielding is smaller than in a shallower area. The tectonic stress directly reflects the rocks in the deep areas. However, the problem of how the cracks or fractures contribute to the stress distributions must be considered. Consequently, a better evaluation method for the quantity of in situ cracks and fractures is necessary, as well as an understanding of their occurrence mechanisms. Useful evaluating techniques, such as the S-wave logging, have to be developed more fully. To discuss the proposed stress magnitude map with regard to the earthquake occurrence possibility, two basic questions have to be discussed: How large is the actual maximum shear stress magnitude for breaking the crust? And is it possible to apply the shear stresses measured at the shallower crust to the real depth where earthquakes are occurring? These problems still remain unsolved. The influences of the temperature and pore pressure also have to be taken into consideration to solve these problems. In the future, these points and problems will have to be studied more completely in order for scientists to better understand and perhaps someday predict the fundamental forces which cause earthquakes and crustal deformations.

APPENDIX A:

FIELD EQUIPMENT

Inflatable packer

Much time is needed to place down and pull up the pressurization line equipped with inflatable packers as the measuring depth and points increase. A pressurization system using a wireline has been developed (HAIMSON and LEE, 1987; RUMMEL, 1988). Since this system uses a high-pressure hose as the pressurization line, it has advantages in efficiency for shallow depth measurements. At deeper positions, however, the handling of the hose is too difficult. From the beginning of our experiments, drilling pipes (89 cm in diameter) have been used for the pressurization line, particularly in considering the safety of the handling of the equipment and pressurization of the wells.

Two types of inflatable packers are used. The mechanisms of a conventional packer system, which was used during the period of 1978 to 1984, is illustrated schematically in Fig. A1. It works mainly with a check valve and a shear-pin. The diameter and the length of the packer used for our experiments are 12 cm and 170 cm, respectively. The interval needed for the pressurization between two packers is about 220 cm.

A new packer system, which has been used since 1985, is shown in Fig. A2. It works with a standing valve instead of the shear-pin. After the inflatable packers are set and pressure in the work string is released, the standing valve is lifted by wireline to open the work string through the packer. The diameter and the length of this packer are almost the same as the previous one. The interval for pressurization is variable from 70 cm to

200 cm. This system has an advantage to save time for experiments because it can be run at several depths with only one insertion of the packer into the borehole.

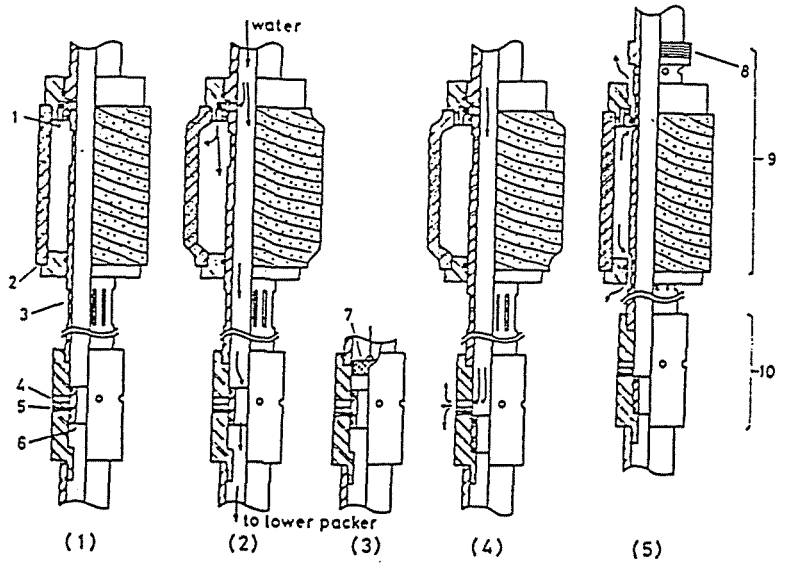

Fig.A1: Schematic illustration of the inflatable packer, a shear-pin type. (1) Before inflation, (2) Inflation, (3) Opening of injection ports, (4) Water injection, and (5) Deflation.
1. Check valve, 2. Packer element, 3. Grooves for releasing, 4. injection ports, 5. shear-pins, 6. Sleeve, 7. Weight, 8. Right-turn releasing thread, 9. Inflatable packer, and 10. Injection valve.

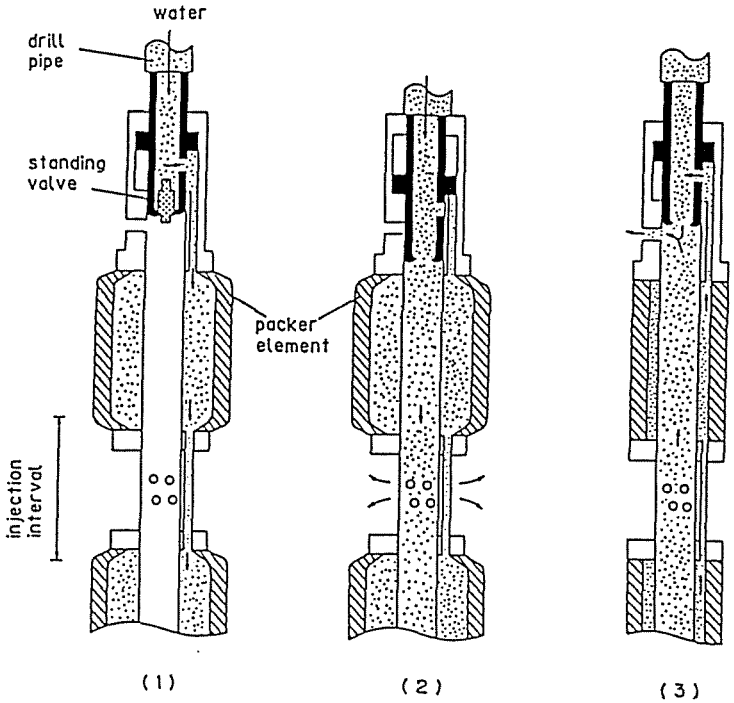

Fig.A2: Schematic illustration of the inflatable packer, a standing valve type. (1) Inflation, (2) Water injection, and (3) Deflation.

Ultra-sonic borehole televiewer

To detect hydraulic fractures and to inspect borehole wall conditions, an unique logging tool, called the borehole televiewer (BHTV), has been developed. Fig. A3 shows the schematic illustration of the BHTV logging system. The most important characteristic of the BHTV is that it works well even in drilling mud in the borehole where an optical instrument cannot be used.

ZEMANEK et al. (1969) explains the following fundamental mechanisms of the BHTV: A piezoelectric transducer probes the borehole wall with bursts of acoustic energy. A flux-gate magnetometer senses the earth's magnetic field and provides the means for determining the orientation of the log. A motor rotates the transducer and magnetometer within the tool about the vertical axis at approximately 3 revolutions/sec. Appropriate electronic circuits process signals from the transducer and magnetometer for use at the surface. The transducer serves as a transmitter and receiver of acoustic energy whose predominant frequency is about 1.2 MHz (in our case). Pulses of acoustic energy are directed toward the borehole wall at a rate of 2,000 pulses/sec. Because the tool is moved vertically and simultaneously with the transducer rotation, a spiral strip of the borehole wall is probed.

The amount of energy reflected by the borehole wall is a function of the physical properties of the surface. A smooth surface will reflect better than a rough surface, hard better than soft, a surface perpendicular to the transducer better than skew, etc. In general, any irregularities will reduce the amplitude of the reflected signal.

According to laboratory experiments, the BHTV can define induced and natural fractures on the borehole wall beneath the drilling mud of within a thickness of 4 mm. It is possible to detect fractures under 1 mm width if the borehole condition is good (OHKAWARA et al., 1980).

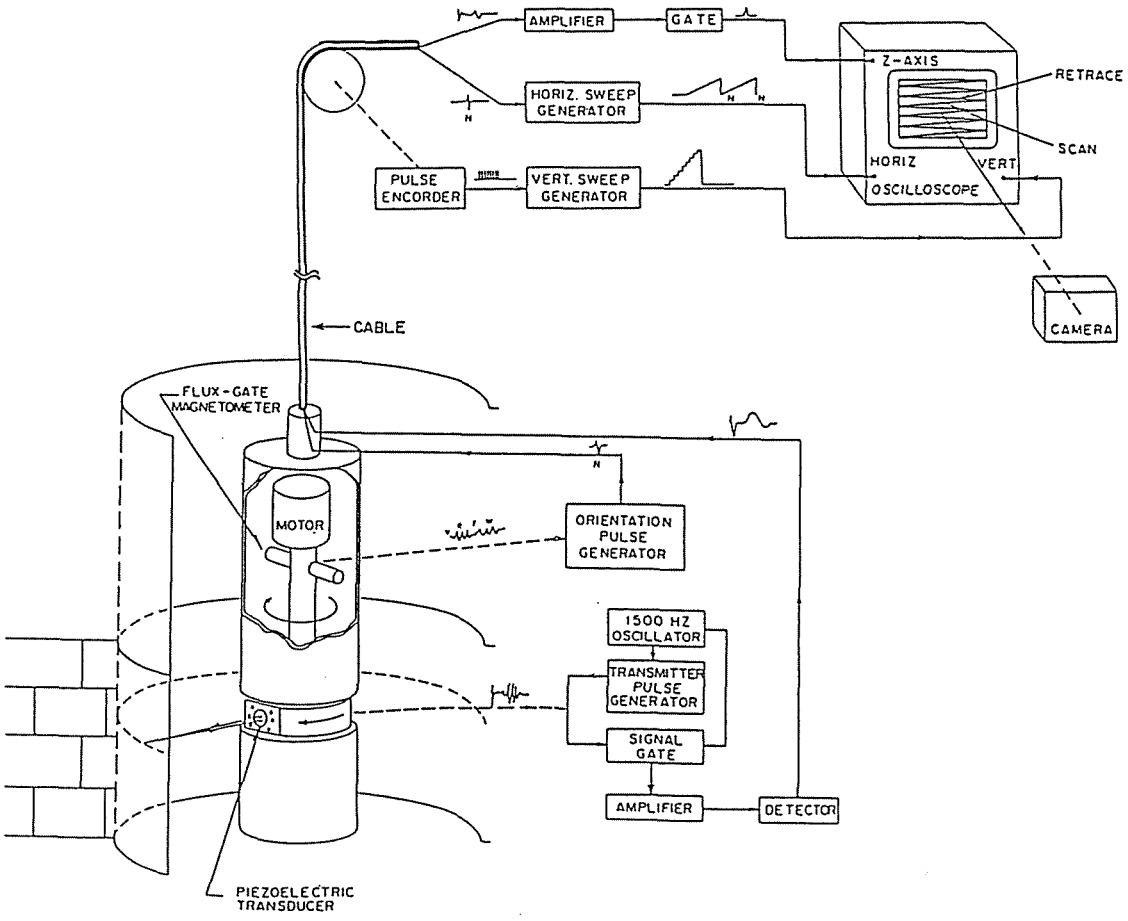

Fig.A3: Schematic illustration of the borehole televiewer [after ZEMANEK et al. (1969)].

Impression packer

The impression packer is a device for obtaining the fracture traces on the wall of a borehole (ANDERSON and STAHL, 1967). The impression material, which is wound around the inflatable packer, is a soft, partially cured, rubber with little or no elasticity. The range of the inflating pressure is several MPa higher than the reopening pressure of the hydraulic fractures, and it is held constant for about 30 minutes. Magnetic north is measured by the magnetic direction detector set in the non-magnetic pipe just above the impression packer. The softness of the rubber, the inflating holding time, and the rock qualities influence whether the impression succeeds or fails. The rate of success is about 80 %, which is higher than that of the BHTV, because the impression packer can reopen forcibly the fractures that are shut-in.

Since a lot of time is needed to place down and pull up the pressurization line, a new dual impression packer was developed (IKEDA and TSUKAHARA, 1989). It can measure at two depths by only one insertion of the packers into the borehole. Fig. A4 shows the running procedure of the dual impression packer. At first, the bottom packer is run to the setting depth (1). Then a small ball is dropped in to seal the bottom landing sub. In order to take the impression by the bottom packer, the pressure is raised to the desired level (2). After the impression is taken, the impression packer is deflated and moved to the next impression point (3). A large ball is dropped to the top landing sub. The pressure is then again raised and the top impression packer is inflated (4). After the impression is taken, the top packer is deflated and all lines are pulled up to the surface (5).

This simple mechanism and procedure can be applied to not only two impressions but more by using different diameter balls.

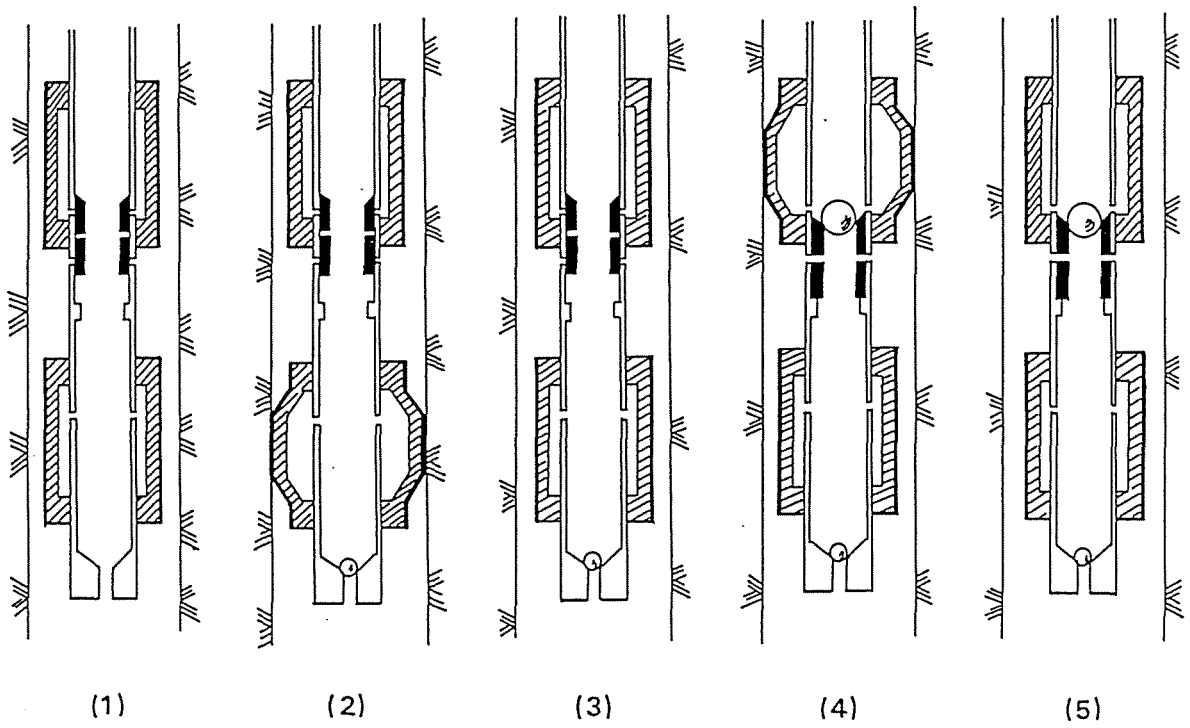

Fig.A4: Schematic illustration of the operation of the dual impression packer system.

APPENDIX B:

LITHOLOGY AND GEOPHYSICAL LOGGING OF EACH WELL

The lithologies were determined by drilling cuttings and cored samples. They are shown in the first column of each well record along with the geophysical logs. The papers referred to in each figure caption are papers other than TSUKAHARA and IKEDA (1987). The results of the sites, Enzan [EN], Tanzawa [TZ] and Ashigawa [AS] are shown in Section 5 in the text.

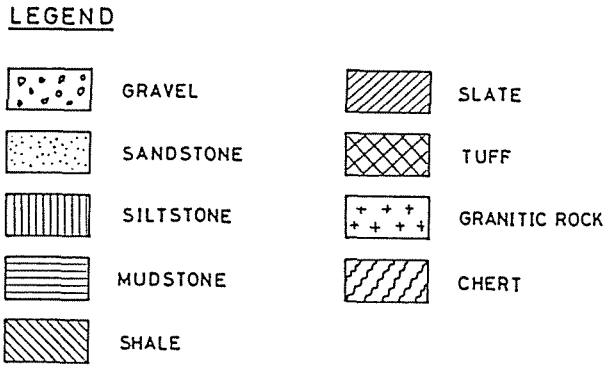

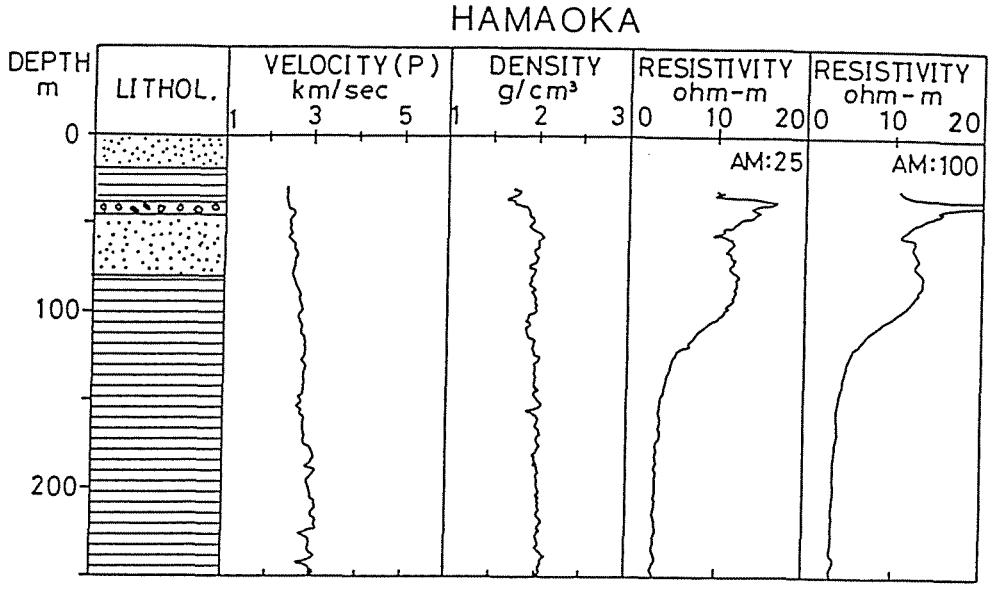

Fig.B1: HAMAOKA [HM]. Quaternary sand exists to the depth of 18 m. Below this depth, the Sagara Group of Neogene age is composed mainly of mudstone and interbedded with thin sandstones (IKEDA and TSUKAHARA, 1987a).

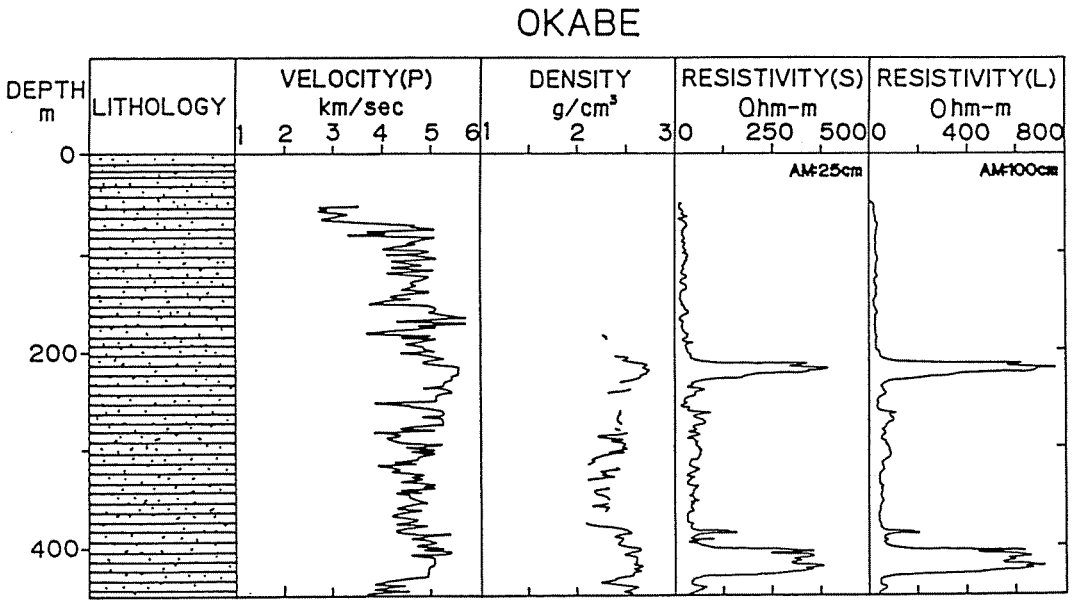

Fig.B2: OKABE [M][K][OK]. The [M] and [K] wells were drilled to the depth of 100 m in 1978. The [OK] well, which is 3 km apart from the [M] well and 10 m from the [K] well, was drilled to the depth of 450 m in 1981. The formation of each well consists of mainly mudstone and sandstone alternating with clayey beds of Paleogene age (the Setogawa Group) (TSUKAHARA et al., 1978, 1983a).

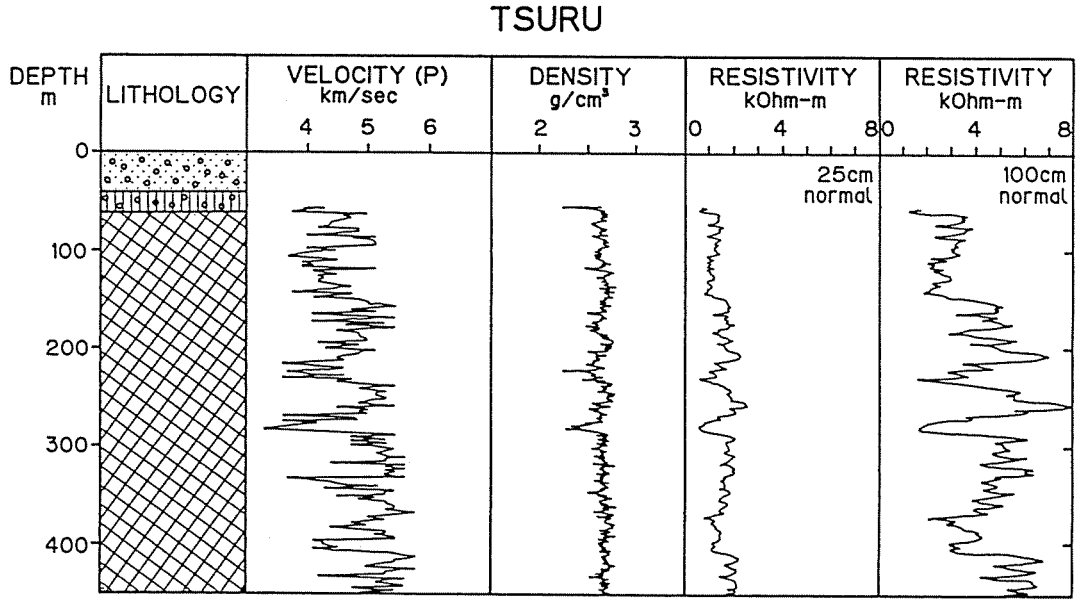

Fig.B3: TSURU [TR]. Below the depth of 60 m to the bottom, andesitic tuff and tuff breccia of Miocene age (the Misaka Group) exist (IKEDA and TSUKAHARA, 1987b).

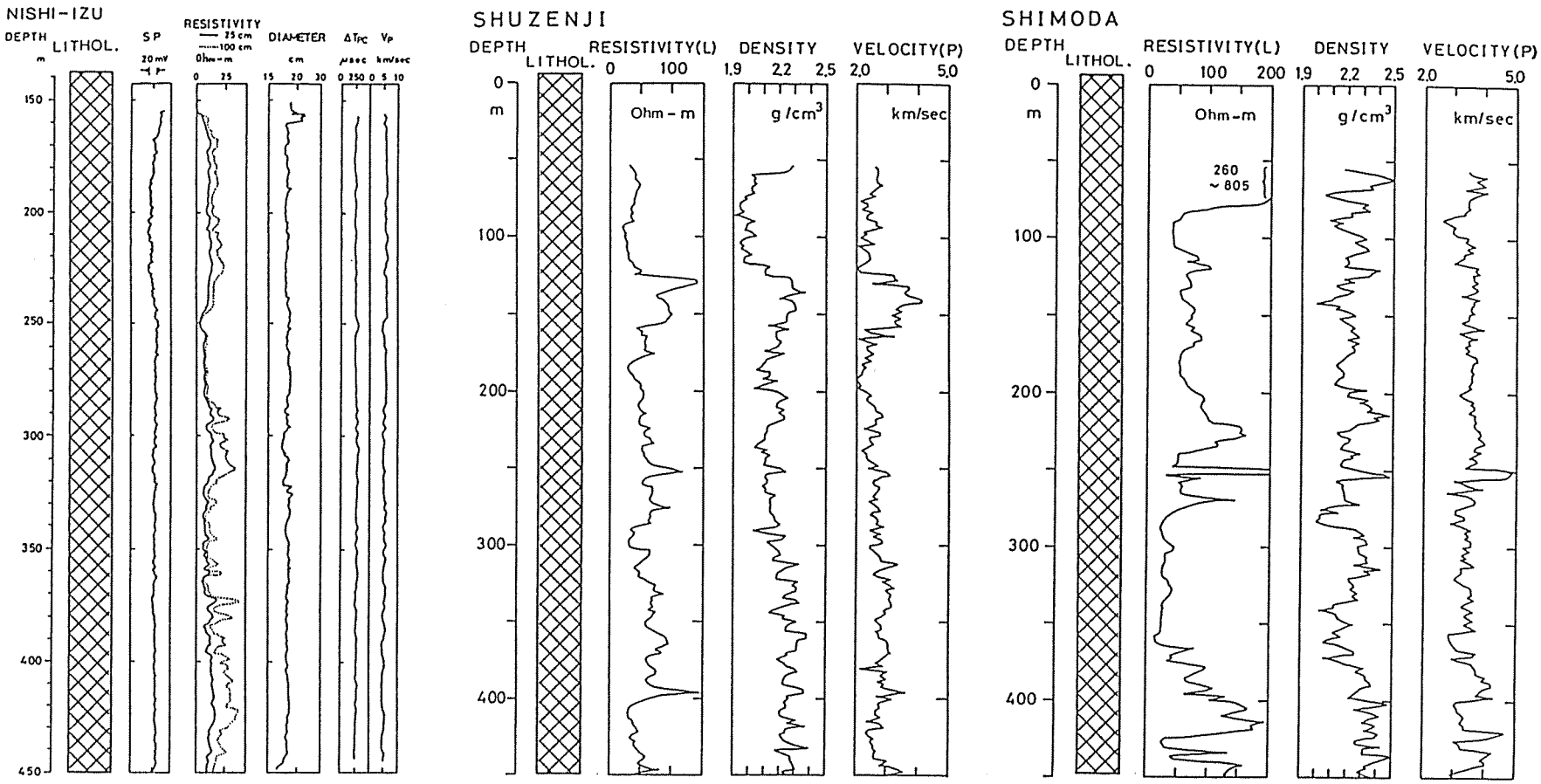

Fig.B4: NISHI-IZU [NI], SHUZENJI [SZ], SHIMODA [SM]. From the surface to the bottom of each well, andesitic tuff and tuff breccia of Miocene age (the Yugashima Group) exist (TSUKAHARA et al., 1980, 1983a).

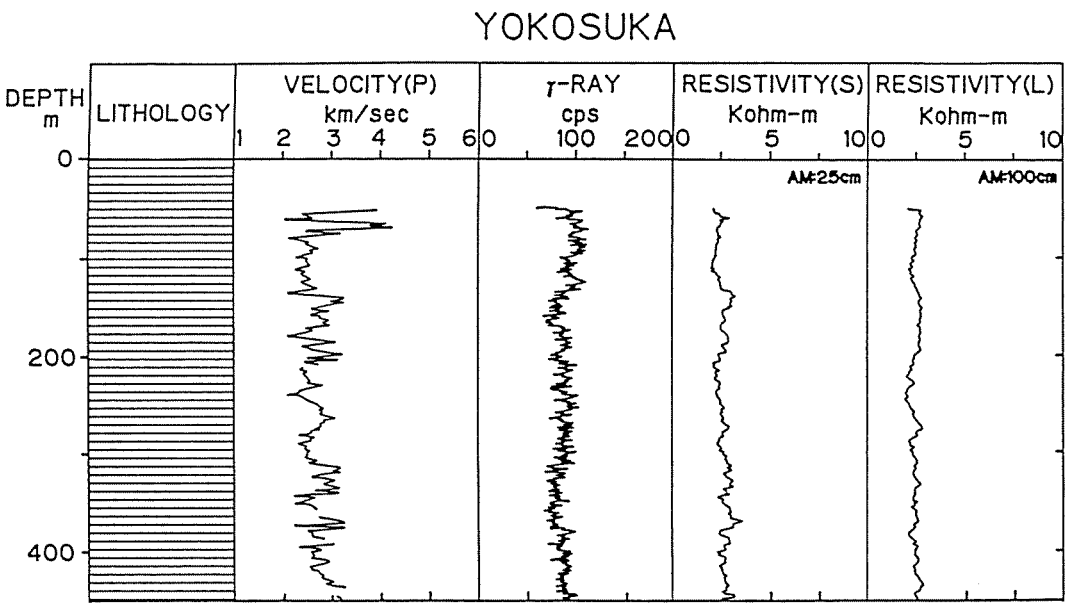

Fig.B5: YOKOSUKA [YK]. From the surface to the bottom, mudstone with many preexisting fractures of Miocene age (the Morito Formation of the Hayama Group) exist (TSUKAHARA et al., 1983a).

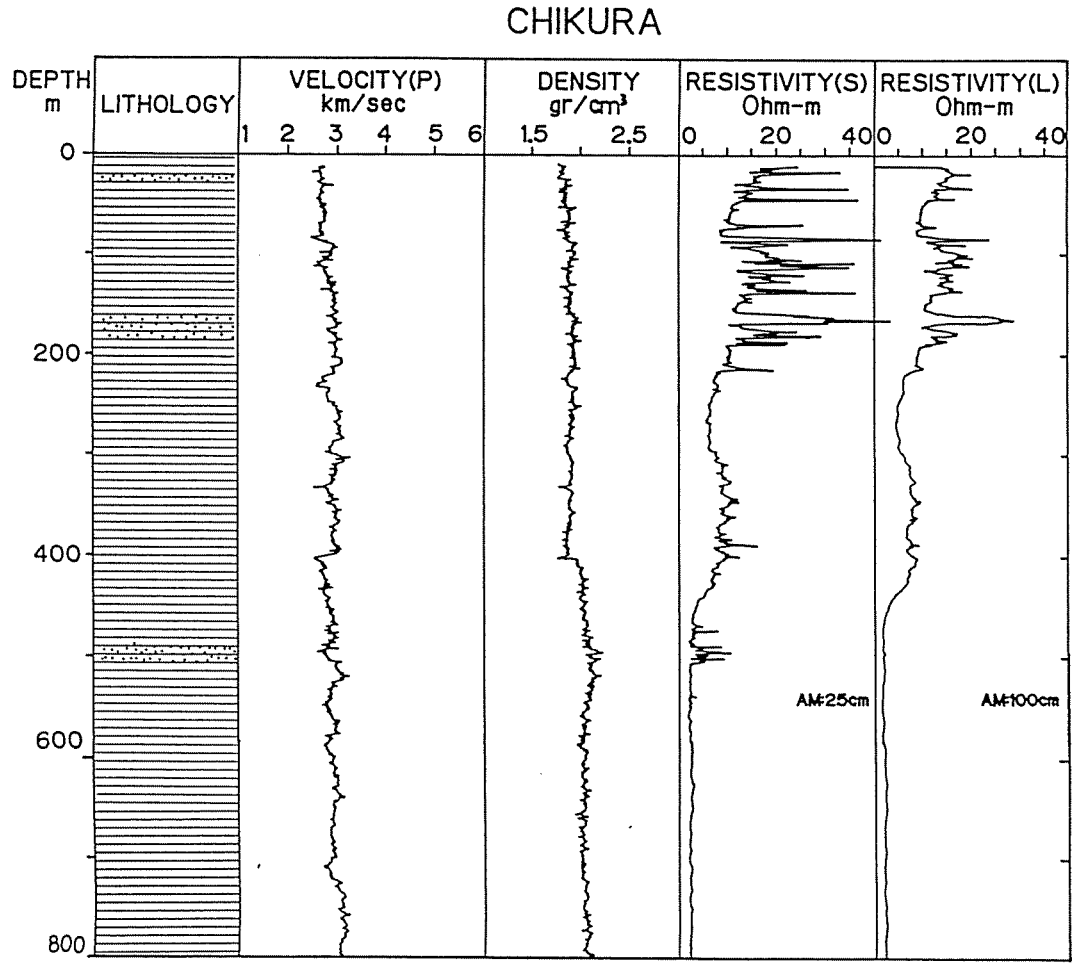

Fig.B6: CHIKURA [CK]. From the surface to the bottom, the formation is composed mainly of mudstone and is interbedded with thin sandstones of Early Pliocene age (the Chikura Formation of the Miura Group) (TUKAHARA and IKEDA, 1985).

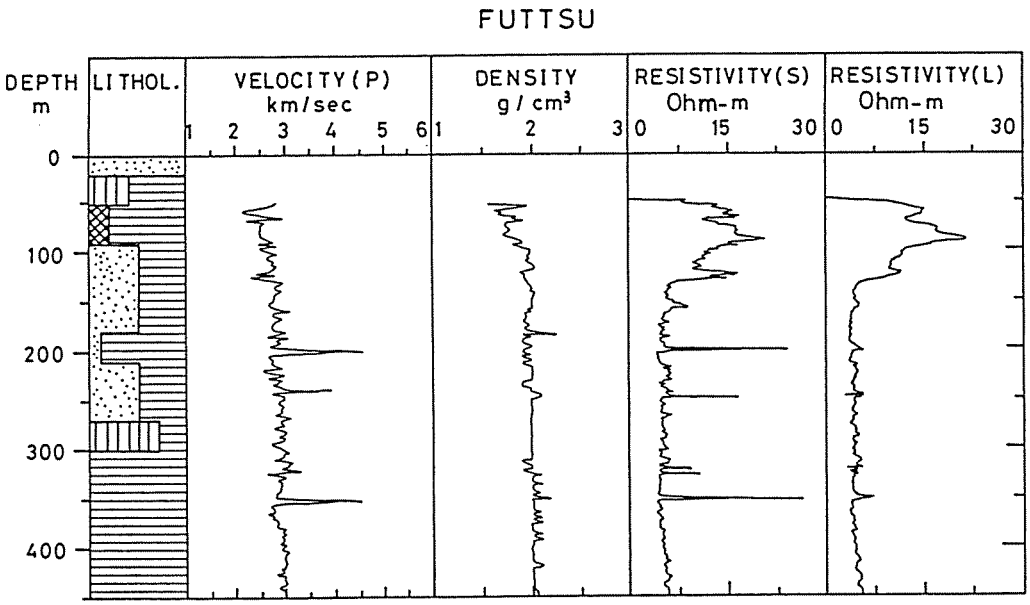

Fig.B7: FUTTSU [FT]. From the surface to bottom, the formation is composed of mudstone and sandstone and is interbedded with thin shale beds of Miocene age (the Amatsu Formation of the Miura Group) (IKEDA and TAKAHASHI, 1981).

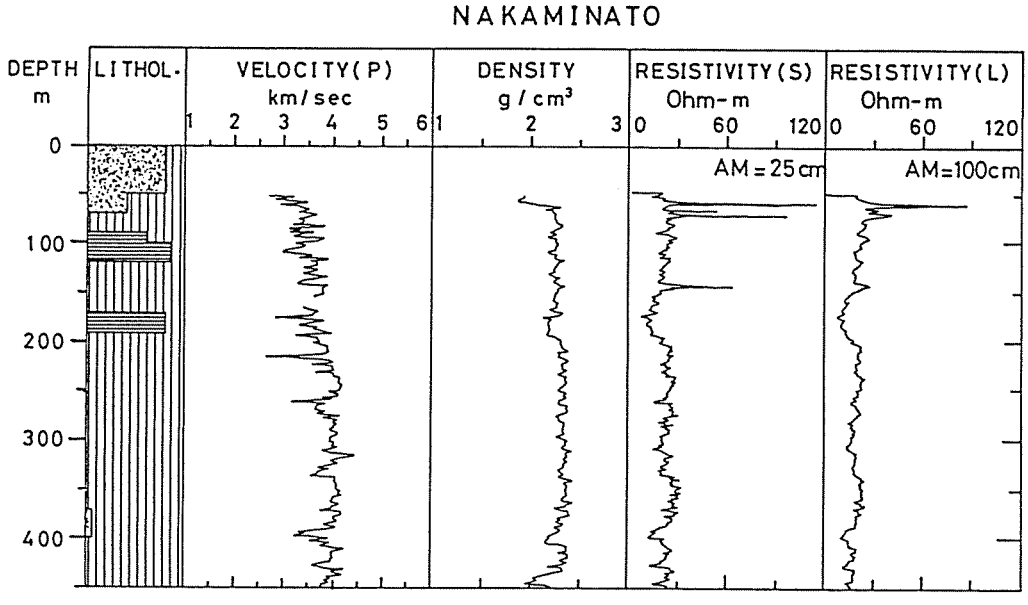

Fig.B8: NAKAMINATO [NA]. Sandy siltstones of Cretaceous age are exposed (the Nakaminato Group) (IKEDA and TAKAHASHI, 1983).

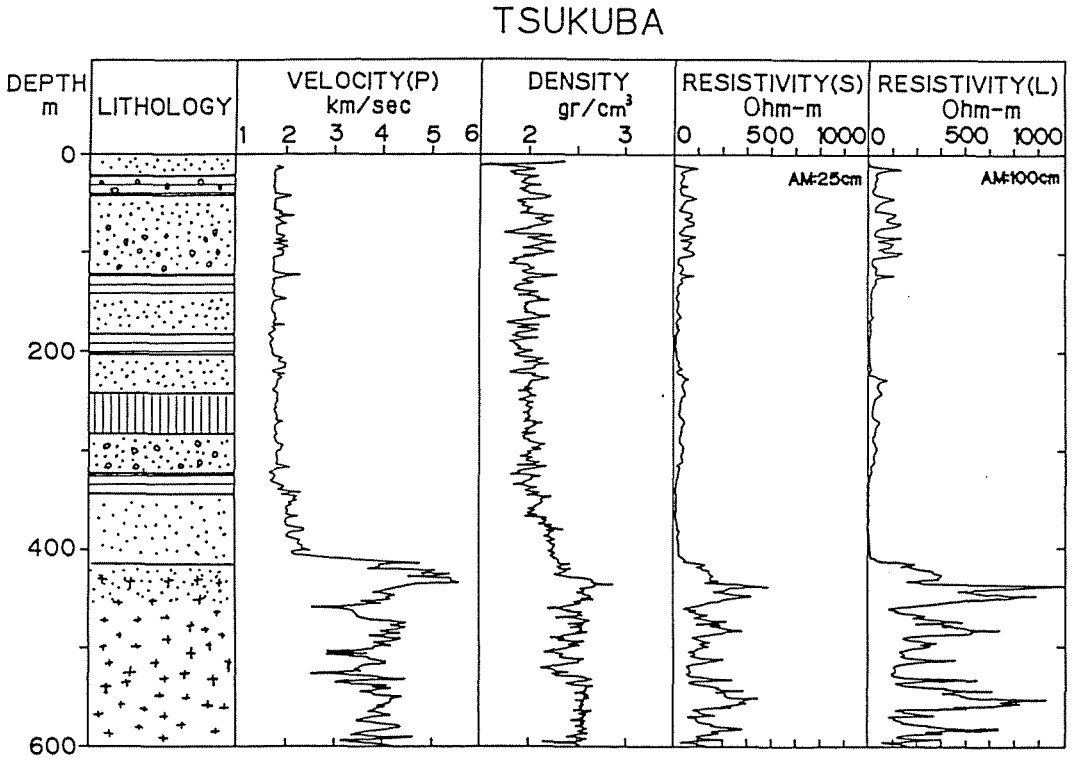

Fig.B9: TSUKUBA [TK]. From the surface to the depth of 410 m, mudstone and sandstone of Quaternary age (the Narita and Kazusa Group) exist. The basement around the area below the depth of 410m to the bottom is metamorphic granitic rocks of Cretaceous age (TSUKAHARA and IKEDA, 1983C).

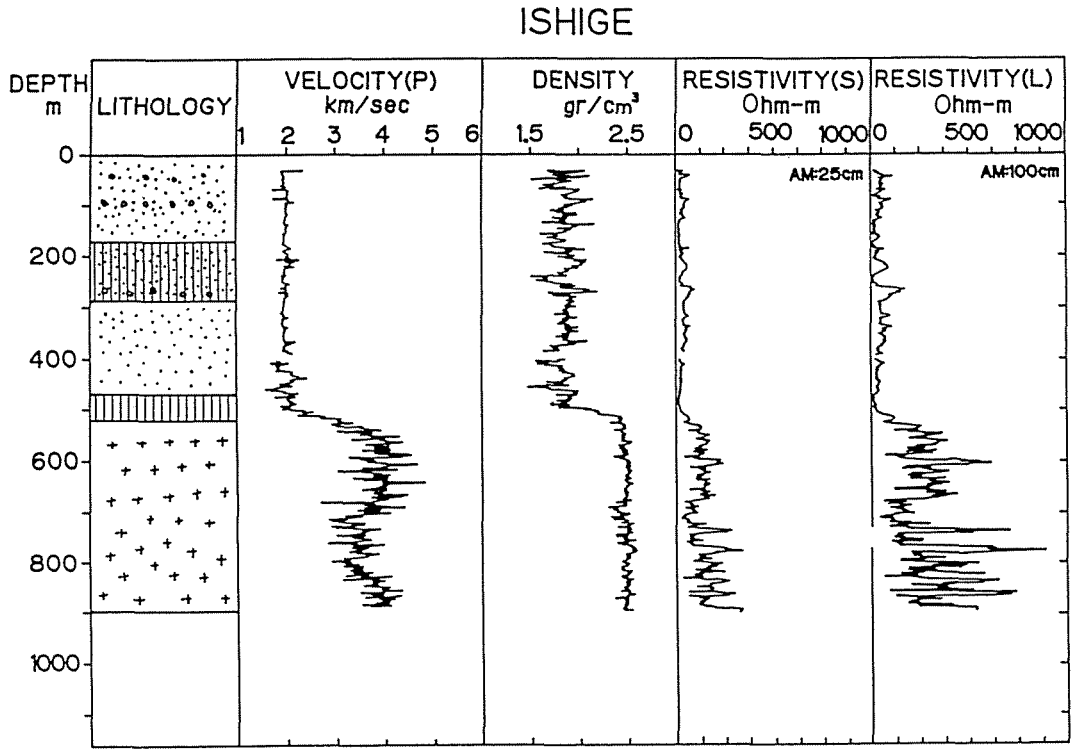

Fig.B10: ISHIGE [IS]. The [IS] well is located about 30 km west of the [TK] well. The formations are very similar to that of the [TK] well. The depth of the granitic rock basement is below 518 m (IKEDA and TSUKAHARA, 1986).

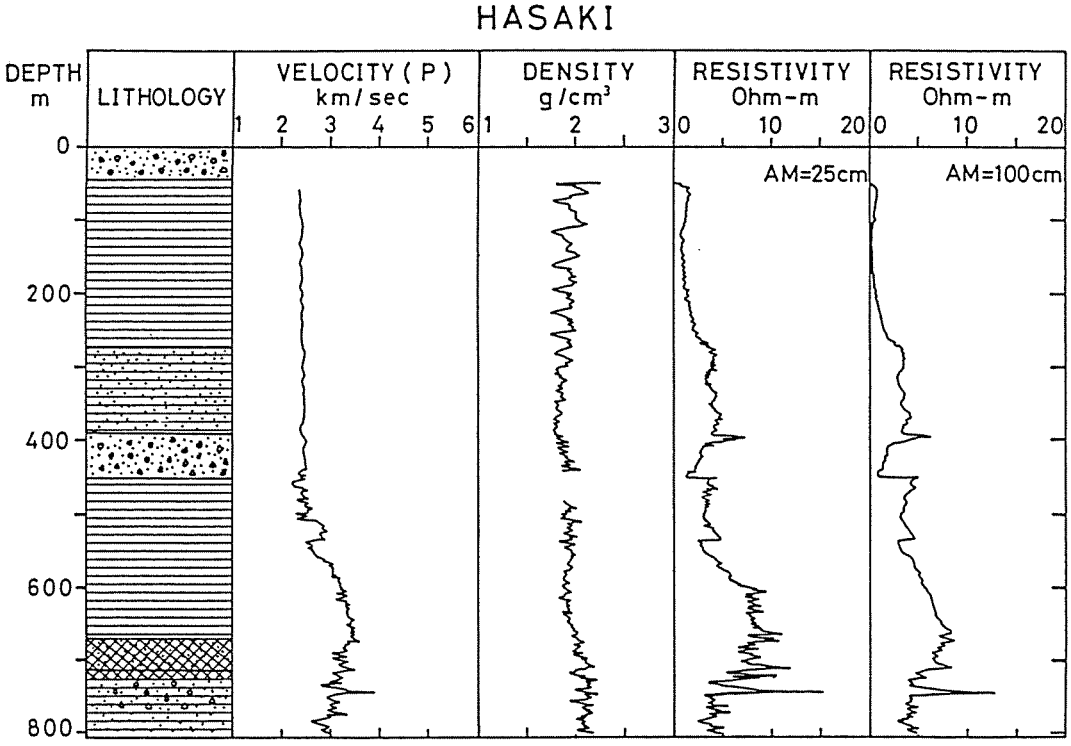

Fig.B11: HASAKI [HS]. From the surface to the depth of 670 m, mudstone and gravel exist. The formation below the depth of 670 m to the bottom is composed of mudstone and gravel and contains tuff. The basement of pre-Paleogene was not discovered till the depth of 800 m (IKEDA and TSUKAHARA, 1984).

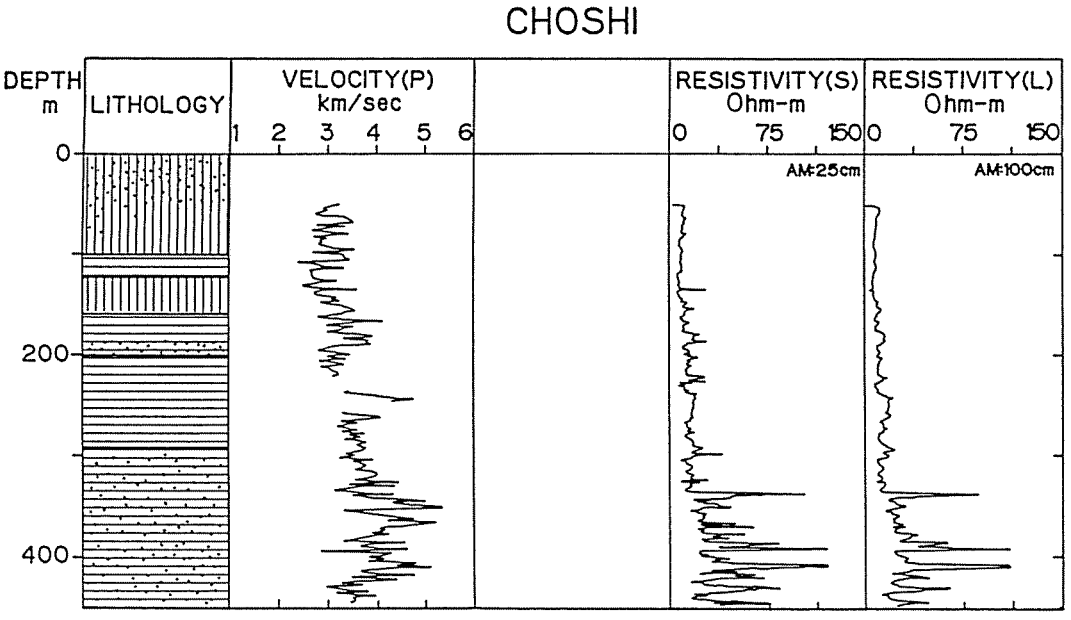

Fig.B12: CHOSHI [CH]. From the surface to bottom, sandy mudstone with many preexisting fractures and clayey beds of Cretaceous age exist. Density was not measured by the log (TSUKAHARA and IKEDA, 1981).

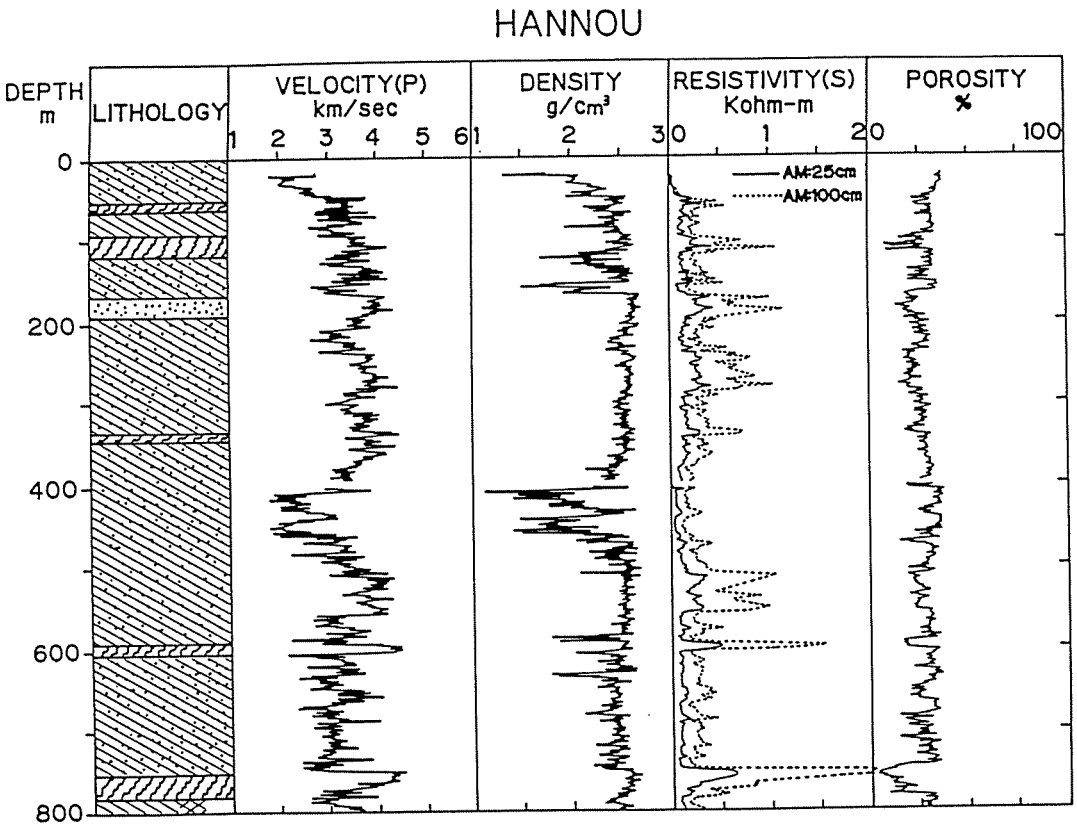

Fig.B13: HANNOU [HN]. The formation is composed of alternating beds of shale and sandstone and is interbedded with thin chert of pre-Neogene age (the Shomaru Formation of the Musashi Group) (IKEDA and TSUKAHARA, 1987c).

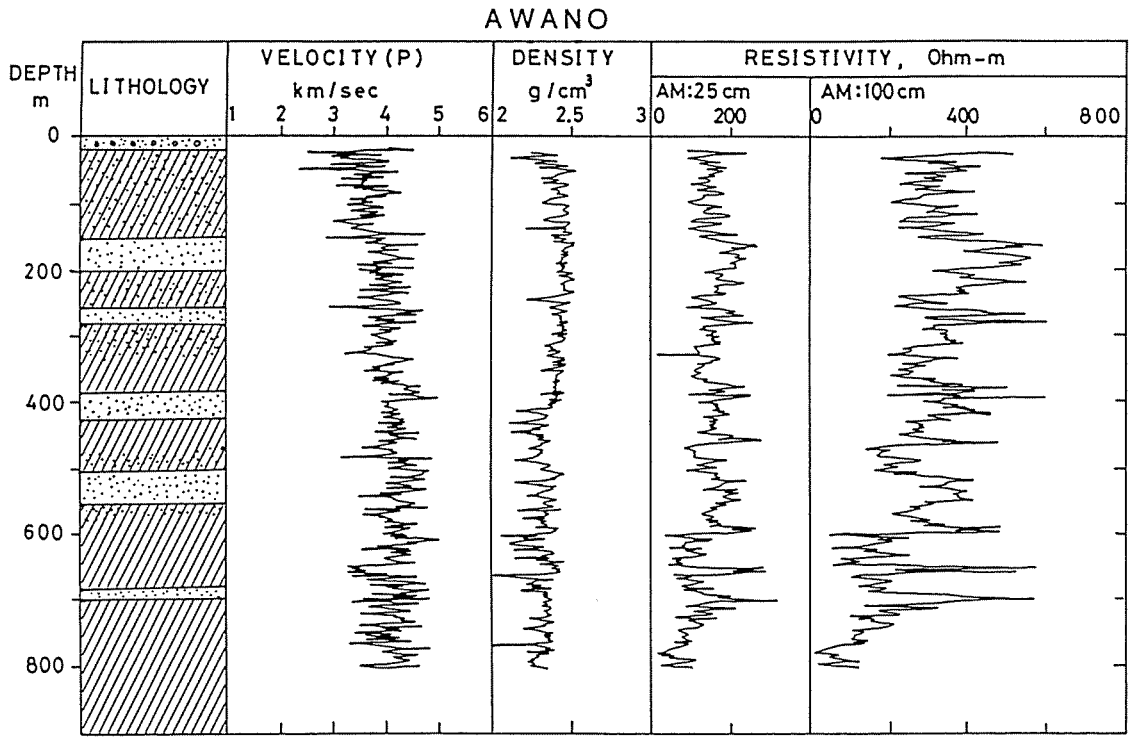

Fig.B14: AWANO [AW]. The formation is composed of alternating beds of sandstone and slate of Paleozoic age (the Aizawa Formation of the Tochigi Group (TSUKAHARA and IKEDA, 1988).

BIBLIOGRAPHY

ANDERSON, T.O. and E.J. STAHL, 1967. A Study of Induced Fracturing Using an Instrumental Approach. Soc. Petroleum. Eng. J., 1967, 261-267.

BASS, J.D., D. SCHMITT and T.J. AHRENS, 1986, Holographic In Situ Stress Measurements, Geophys. J. Res. Astr. Soc., 85, 13-41.

BREDEHOEFT, J.D., R.G. WOLFF, W.S. KEYS, and E. SHUTER, 1976, Hydraulic Fracturing to Determine the Regional In Situ Stress Field, Piceance Basin, Colorado, Geol. Soc. Am. Bull., 87, 250-258.

BYERLEE, J., 1978, Friction of Rocks, Pure and Appl. Geophys., 116, 615-626.

FRIEDMAN, M., 1972, Residual Elastic Strain in Rocks, Tectonophysics, 15, 297-330.

HAIMSON, B.C. and C. FAIRHURST, 1967, Initiation and Extension of Hydraulic Fractures in Rock, Soc. Petroleum Eng. J., 7, 310-318.

HAIMSON, B.C., 1978a, Crustal Stress in the Michigan Basin, J. Geophys. Res., 83, 5857-5863.

HAIMSON, B.C., 1978b, Near-Surface and Deep Hydrofracturing Stress Measurements in the Waterloo Quartzite, Proc. 19th U.S. Symp. on Rock Mechanics, AIME, 1978, 345-361.

HAIMSON, B.C., and M.Y. LEE, 1987, The State of Stress and Natural Fractures in a Jointed Precambrian Rhyolite in South-Central Wisconsin, Proc. 28th U.S. Symp. on Rock Mechanics, Arizona, 1987.

HAIMSON, B.C., J.C. ROEGIERS and M.D. ZOBACK, 1988, Proceedings of the Second International Workshops on Hydraulic Fracturing Stress Measurements, 1003p., Geological Engineering Program, Univ. Wisconsin-Madison, U.S.A.

HAYASHI, K. and I. SAKURAI, 1989, Interpretation of Hydraulic Fracturing Shut-in Curves for Tectonic Stress Measurements, Int. J. Rock Mech. Min. Sci. & Geomech. Abstr., 26, 477-482.

HICKMAN, S.H. and M.D. ZOBACK, 1981, The Interpretation of Hydraulic Fracturing Pressure-Time Data for In-Situ Stress Determination, Hydraulic Fracturing Stress Measurements, National Academy Press, Washington, D.C., 44-54.

HIRAMATSU, Y., Y. OKA, H. ITO, and Y. TANAKA, 1973, The Correlation of the Rock Stress Measured in situ and the Tectonic Stress Inferred from Geological and Geophysical Studies, Proc. 4th Jpn. symp. on Rock Mech., 1973, 157-162 (in Japanese with English Abstr.).

HOSHINO, K., S. YASUDA, and H. KOIDE, 1978, Examples of Residual Stress Measurement in the Kanto-Chubu Area, Abstr. Seismol. Soc. Jpn., 1978(1), 124. (in Japanese).

HUBBERT, M.K. and D.G. WILLIS, 1957, Mechanics of Hydraulic Fracturing, Petroleum Trans. AIME, 210, 153-168.

IKEDA, R., H. TSUKAHARA, H. SATAKE, M. OHTAKE, and H. TAKAHASHI, 1978, Observation of Acoustic Emissions during the Hydrofracturing of the Base Rocks, Zisin (J. Seismol. soc. Jpn.), 31, 435-444 (in Japanese with English Abstr.).

IKEDA, R. and H. TAKAHASHI, 1981, Stress Measurement by Hydrofracturing at Futtsu City, Chiba Prefecture, Zisin (J. Seismol. soc. Jpn.), 34, 565-576, (in Japanese with English Abstr.).

IKEDA, R. and H. TAKAHASHI, 1983, Stress Measurement by Hydrofracturing at Nakaminato City, Ibaraki Prefecture, Zisin (J. Seismol. soc. Jpn.), 36, 213-223 (in Japanese with English Abstr.).

IKEDA, R. and H. TSUKAHARA, 1983, Acoustic Emissions Detected hy Hydrophones During Hydraulic Fracturing Stress Measurement, Hydraulic Fracturing Stress Measurements, National Academy Press, Washington D.C., 210-214.

IKEDA, R. and H. TSUKAHARA, 1984, Crustal Stress Measurement by Hydrofracturing: Hasaki Town, Ibaraki Prefecture, and Hamaoka Town, Shizuoka Prefecture, Abstr. Seismol. Soc. Jpn., 1984(2), 169 (in Japanese).

IKEDA, R. and H. TSUKAHARA, 1986, Crustal Stress Measurement by Hydrofracturing: Ishige Town, Ibaraki Prefecture, and Ashigawa Village, Yamanashi Prefecture, Abstr. Seismol. Soc. Jpn., 1986(2), 231 (in Japanese).

IKEDA, R. and H. TSUKAHARA, 1987a, Crustal Stress Measurement and Pore Pressure Observation in Omaezaki Peninsula, Shizuoka Prefecture, Geophys. Bull. Hokkaido Univ. No. 49, 269-279 (in Japanese with English Abstr.).

IKEDA, R. and H. TAKAHASHI, 1987b, Hydraulic Fracturing Stress Measurements at Ashigawa-Mura and Tsuru City in Yamanashi Prefecture - the Vertical State of Stress and the Regional Stress Field -, Zisin (J. Seismol. soc. Jpn.), 40, 519-531 (in Japanese with English Abstr.).

IKEDA, R. and H. TSUKAHARA, 1987c, Crustal Stress Measurements by Hydrofracturing: Hannou City, Saitama Prefecture, Abstr. Seismol. Soc. Jpn., 1987(2), 296 (in Japanese).

IKEDA, R. and H. TSUKAHARA, 1989, Hydraulic Fracturing Technique: Pore Pressure Effect and Stress Heterogeneity, Int. J. Rock Mech. Min. Sci. & Geomech. Abstr., 26, 471-475.

IKEDA, R. and H. TSUKAHARA, 1990, Hydrofracturing Crustal Stress Measurements in Granitic Rocks, Proc. 8th Jpn. Symp. on Rock Mechanics, 1990, 309-314 (in Japanese with English Abstr.).

IKEDA, R. and H. TSUKAHARA, 1991, Characteristics and the Mechanisms of Crustal-Stress Distribution in Hard Rocks, J. Min. & Materials Processing Inst. Jpn., 107, 441-445 (in Japanese with English Abstr.).

JAEGER, J.C. and M.G.W. COOK, 1976, Fundamentals of Rock Mechanics, 2e, 585p., John Willey & Sons, New York.

KAJIKAWA, S., K. MASUDA, I. YAMADA, and O.IDEHARA, 1990, Characteristics of Microcracks Produced in Granites with Different Grain-Size, Zisin (J. Seismol. soc. Jpn.), 43, 179-188 (in Japanese with English Abstr.).

KANAGAWA, T., M. HAYASHI, and H. NAKASA, 1977, Estimation of Spatial Geostress Components in Rock Samples Using the Kaiser Effect of Acoustic Emission, Proc. Jpn. Soc. Civil Eng., 258, 63-75 (in Japanese).

KANAGAWA, T., Y. KITAHARA, and M. HAYASHI, 1981, Determination of Geostress in Rock Samples Using the Kaiser Effect of Acoustic Emission - Uni-axial Tests and Its Applications -, Central Res.Inst. Electric Power Industry Rep., No. 381004, 37p, (in Japanese with English Abstr.).

KEHLE, R.O., 1964, Determination of Tectonic Stresses through Analysis of Hydraulic Well Fracturing, J. Geophys. Res., 69, 259-273.

KOIDE, H., 1980, Problems of Stress Measurements for Earthquake Prediction, The Earth Monthly, 2, 578-585 (in Japanese).

KOIDE, H., Y. NISHIMATU, S. KOIZUMI, K. HOSHINO, T. KANAGAWA, Y. NAKAYAMA, A. INOUE, K. YAMAMOTO, and S. KIKUCHI, 1986, Comparison among Several Methods for Stress Measurement in the Kanto-Tokai District, Japan, Proc. 19th Symp. Rock Mech., 1986, 261-265 (in Japanese with English Abstr.).

KURIYAGAWA, M., H. KOBAYASHI, I. MATSUNAGA, T. YAMAGUCHI, and K. HIBIYA, 1989, Application of Hydraulic Fracturing to Three-Dimensional In Situ Stress Measurement, Int. J. Rock Mech. Min. Sci. & Geomech. Abstr., 26, 587-593.

LOCKNER, D.A., J.B. WALSH and J.D. BYERLEE, 1977, Changes in Seismic Velocity Attenuation During Deformation of Granite, J. Geophys. Res., 82, 5374-5378.

MASTIN, L., B. MULLER, and M.L. ZOBACK, 1989, World Stress Map, International Workshop on the European Contribution, EOS, November 28.

MOOS, D., and M.D. ZOBACK, 1990, Utilization of Observations of Well Bore Failure to Constrain the Orientation and Magnitude of Crustal Stresses: Application to Continental, Deep Sea Drilling Project and Ocean Drilling Project Boreholes, J. Geophys. Res., 95, 9305-9325.

O'CONNELL, R.J. and B. BUDIANSKY, 1974, Seismic Velocities in Dry and Saturated Cracked Solids, J. Geophys. Res., 79, 5412-5426.

OGINO, S., Y. MIZUTA, O. SANO, R. KITAGAWA, and T. SAITO, 1984, A Study on Three Dimensional Stress Determination in a Basement by Hydraulic Fracturing, Rep. S. 58 Grant-in-Aid for Developmental Sci. Res., Yamaguchi Univ., 49p (in Japanese).

OHKAWARA, T., T. YAMASHITA, and R. IKEDA, 1980, Ability of Borehole Televiewer, Proc. Soc. Explor. Geophys. Jpn., 1980(1), 11 (in Japanese).

PLUB, R.A. and J.W. COX, 1987, Stress Directions in Eastern North America Determined to 4.5 km from Borehole Elongation Measurements, J. Geophys. Res., 92, 4805-4816.

RUMMEL, F., 1988, Hydraulic Fracturing Stress Measurements - Theory and Practice -, KTB-Report, 88(8), 53-65.

SATO, H., T. TSUKAHARA, and R. IKEDA, 1987, Spatial Autocorrelation Function of Fracture Strength of Rock: Boring Core Samples of a Well in Ashigawa-mura, Yamanashi Prefecture, Japan, Zisin (J. Seismol. soc. Jpn.), 40, 513-518 (in Japanese with English abstr.).

SCHEIDEGGER, A.E., 1962, Stress in the Earth's Crust as Determined from Hydraulic Fracturing Data, Geologie und Bauwessen, 27, 45-60.

SUZUKI, H., 1989, Focal Mechanisms of Intracrustal Earthquakes and Stress Field of the Earth Crust in the Kanto-Chubu Area, Japan, Rep. National Res. Center for Disaster Prev., No. 43, 125p (in Japanese with English Abstr.).

TANAKA, Y., 1985, Crustal Stress Measurement and Earthquake Prediction, J. Geodetic Soc. Jpn., 31, 73-85.

TANAKA, Y., 1986, State of Crustal Stress Inferred from In Situ Stress Measurements, J. Phys. Earth, 34, s57-s70.

TANAKA, Y., 1987, Crustal Stress Measurements in Japan - Research Trends and Problems -, Proc. Earthquake Prediction Res. Symp. (1987), 199-212 (in Japanese with English Abstr.).

THE RESEARCH GROUP FOR CRUSTAL STRESS IN WESTERN JAPAN, 1986, Comparative and Repeated Measurements of Crustal Stress by a Stress Relief Method and a Hydrofracturing Method - the Rokko-Suwayama Test Site, Kinki -, Rep. Coordinating Committee for Earthquake Prediction, 36, 365-369 (in Japanese).

TSUKAHARA, H., R. IKEDA, H. SATAKE, M. OHTAKE, and H. TAKAHASHI, 1978, Hydrofracturing Stress Measurements at Okabe Town, Shizuoka Prefecture, Zisin (J. Seismol. soc. Jpn.), 31, 415-433 (in Japanese with English Abstr.).

TSUKAHARA, H., R. IKEDA, H. SATAKE, and H. TAKAHASHI, 1980, Stress Measurements by Hydrofracturing at Nishiizu Town, Shizuoka Prefecture, Zisin (J. Seismol. soc. Jpn.), 33, 317-327 (in Japanese with English Abstr.).

TSUKAHARA, H., R. IKEDA, H. SATAKE, and H. TAKAHASHI, 1981, Stress Measurements by Hydrofracturing at Choshi City, Chiba Prefecture, Zisin (J. Seismol. soc. Jpn.), 34, 13-20 (in Japanese with English Abstr.).

TSUKAHARA, H., R. IKEDA, and H. TAKAHASHI, 1983a, Hydraulic Fracturing Stress Measurements: Results at Okabe Town, Shuzenji Town and Shimoda City in Shizuoka Prefecture and Yokosuka City in Kanagawa Prefecture, Zisin (J. Seismol. soc. Jpn.), 36, 551-569 (in Japanese with English Abstr.).

TSUKAHARA, H., R. IKEDA, 1983b, State of Stress in the Kanto-Tokai Area, Zisin (J. Seismol. soc. Jpn.), 36, 571-586 (in Japanese with English Abstr.).

TSUKAHARA, H., R. IKEDA, 1983c, Crustal Stress Measurements by Hydrofracturing: Tsuru City in Yamanashi Prefecture and Tsukuba in Ibaraki Prefecture, Abstr. Seismol. Soc. Jpn., 1983(2), 107 (in Japanese).

TSUKAHARA, H., R. IKEDA, 1985, Crustal Stress Measurements by Hydrofracturing: Chikura Town in Chiba Prefecture, Abstr. Seismol. Soc. Jpn., 1985(2), 107 (in Japanese).

TSUKAHARA, H., R. IKEDA, 1986, Three Dimensional Stress Field in the Southern Part of Fossa Magna, The Earth Monthly, 8, 602-605 (in Japanese).

TSUKAHARA, H., R. IKEDA, 1987, Hydraulic Fracturing Stress Measurements and In-situ Stress Field in the Kanto-Tokai Area, Japan, Tectonophysics, 135, 329-345.

TSUKAHARA, H., R. IKEDA, 1988, Crustal Stress Measurements by Hydrofracturing: Awano Town in Tochigi Prefecture, Abstr. Seismol. Soc. Jpn., 1988(2), 96 (in Japanese).

TSUKAHARA, H., R. IKEDA, 1989a, Stress in Sedimentary Rocks Estimated from Stress Profiles Measured at Shallow Depths, J. Geol. Soc. Jpn., 95, 571-578 (in Japanese with English Abstr.).

TSUKAHARA, H., R. IKEDA, 1989b, State of Stress in the Kanto Area, J. Jpn. Soc. Eng. Geol., 30, 41-46 (in Japanese).

TSUKAHARA, H., R. IKEDA, 1990, Drilling into Earthquake Foci: Preliminary Results, EOS, 71, 894.

TSUKAHARA, H., R. IKEDA, 1991, Crustal Stress Orientation Pattern in the Central Part of Honshu, Japan - Stress Provinces and Their Origins -, J. Geol. Soc. Jpn., 97, 461-474 (in Japanese with English Abstr.).

WOLTER, K.E. and H. BERCKHEMER, 1989, Time Dependent Strain Recovery of Cores from the KTB - Deep Drill Hole, Rock Mech. and Rock Engin., 22, 273-287.

WOLTER, K.E. and H. BERCKHEMER, 1990, Estimation of In Situ Stresses by Evaluation of Time-Dependent Strain Recovery of KTB Drill Cores, Tectonophysics, 178, 255-257.

YAMAMOTO, K., Y. KUWAHARA, N. KATO and T. HIRASAWA, 1990, Deformation Rate Analysis: A New Method for In Situ Stress Estimation from Inelastic Deformation of Rock Samples under Uni-Axial Compressions, Tohoku Geophys. J. (Sci. Rep. Tohoku Univ., Ser. 5), 33, 127-147.

YOSHIKAWA, S. and K. MOGI, 1981, A New Method for Estimation of the Crustal Stress from Cored Rock Samples: Laboratory Study in the Case of Uniaxial Compression, Tectonophysics, 74, 323-339.

ZEMANEK, J., R.L. CALDWELL, E.E. GLENN, Jr., S.V. HOLCOMB, L.J. NORTON, and A.J.D. STRAUS, 1969, The Borehole Televiewer - A New Logging Concept for Fracture Location and Other Types of Borehole Inspection, J. Petroleum Technology, 21, 762-774.

ZHENG, Z., J. KEMENY, and N.G.W. COOK, 1989, Analysis of Borehole Breakouts, J. Geophys. Res., 94, 7171-7182.

ZOBACK, M.D., J. HEALY, and J. ROLLER, 1977, Preliminary Stress Measurements in Central California Using the Hydraulic Fracturing Technique, Pure Appl. Geophys., 115, 135-152.

ZOBACK, M.D., H. TSUKAHARA and S.H. HICKMAN, 1980, Stress Measurements at Depth in the Vicinity of the San Andreas Fault: Implications for the Magnitude of Shear Stress at Depth, J. Geophys. Res., 85, 6157-6173.

ZOBACK, M.D. and B.C. HAIMSON, 1983, Hydraulic Fracturing Stress Measurements, National Academy Press, Washington, D. C., 270p.

ZOBACK, M.L., M.D. ZOBACK, J. ADAMS, M. ASSUMPCAO, S. BELL, E.A. BERGMAN, P. BLUMLING, N.R. BRERETON, D. DENHAM, J. DING, K. FUCHS, N. GAY, S. GREGERSEN, H.K. GUPTA, A. GVISHIANI, K. JACOB, R. KLEIN, P. KNOLL, M. MAGEE, J.L. MERCIER, B.C. MULLER, C. PAQUIN, K. PAJENDRAN, O. STEPHANSSON, G. SUAREZ, M SUTER, A. UDIAS, S.H. XU, and ZHIZHI., 1989, Global Patterns of Tectonic Stress, Nature, 341, 291-298.